Elastocapillary windlass: from spider silk to smart actuators

Hervé Elettro

▶ To cite this version:

HAL Id: tel-01200518
https://hal.sorbonne-universite.fr/tel-01200518v1

Submitted on 16 Sep 2015 (v1), last revised 4 Dec 2015 (v2)

THÈSE

PRÉSENTÉE À

L'UNIVERSITÉ PIERRE ET MARIE CURIE

École Doctorale de Sciences Mécaniques, Acoustique, Électronique et Robotique de Paris (ED391, SMAER)

Institut D'Alembert, Équipe Mécanique et Ingénierie des Solides et des Structures

Par **Hervé ELETTRO**

POUR OBTENIR LE GRADE DE

DOCTEUR

SPÉCIALITÉ : MÉCANIQUE

Le treuil élasto-capillaire :
De la soie d'araignée aux actionneurs intelligents

Directeurs de thèse : Sébastien NEUKIRCH & Arnaud ANTKOWIAK

Soutenance le : *24 juillet 2015*

devant la commission d'examen formée de :

Arnaud ANTKOWIAK, Maître de conférences UPMC . . . . *Directeur de thèse*

Martine BEN AMAR, Professeur UPMC . . . . *Examinatrice*

François GALLAIRE, Professeur Assistant, EPFL, Lausanne . . . . *Rapporteur*

Sébastien NEUKIRCH, Directeur de Recherche CNRS/UPMC . . . . *Directeur de thèse*

David QUÉRÉ, Directeur de recherche CNRS, ESPCI–Polytechnique . . . . *Examinateur*

Benoît ROMAN, Chargé de recherche CNRS, ESPCI . . . . *Examinateur*

Dominic VELLA, Lecturer, University of Oxford . . . . *Rapporteur*

Fritz VOLLRATH, Professor, University of Oxford . . . . *Invité*

Remerciements

Elasto-capillary windlass:
From spider silk to smart actuators

Abstract

The goal of this PhD thesis was to understand and recreate artificially a self-assembling mechanism involving capillarity and elasticity present in natural spider silk. The primary function of the micronic glue droplets that exist on spider capture silk is to provide the spider web with adhesive properties, crucial in attaining efficiency as a food trap. These droplets play yet another role: the dramatic enhancement of silk mechanical properties, as well as the preservation of the integrity of the web structure. This is due to the localization of the buckling instability within the liquid glue droplets, site of over-compression due to the capillary meniscii. This leads to local coiling of the fibre, and retightening of the overall system. In effect, this is a micronic automatic coiling system that is powered by capillarity, and is thus coined elasto-capillary windlass.

The first part of my thesis aimed to the characterization of natural samples and visualization of the natural windlass. This required adjustements of environmental parameters (especially relative humidity), microscopic observations and sub-micronewton force measurements both in compression and in tension, as well as image analysis and technical problem solving. We have found that the local shape of the fibre is intimately linked to the mechanical properties of the overall sample. The existence of the windlass mechanism implies that under compression this special drop-on-fibre system behaves like a liquid, whereas under tension it has a classical elastic spring regime. Spiders have thus found a way to create liquid-solid mechanical hybrids using shape-induced functionalisation.

We use a fully mechanical model to explain this unique behaviour, as well as an analogy with phase transition formalism. Using a drop-on-deformable-fibre system, we show that if the wetting energy is higher than the bending energy, the system "activates" and in-drop coiling begins. Numerical simulations of 3D elastica under local soft confinement potential reproduce the observed link between local fibre shape and mechanical response. We then fabricate centimeter-long micronic soft fibres, by melt spinning or wet spinning of thermoplastic polymers, and show that the simple addition of a wetting liquid droplet makes for an effective system with mechanical properties quantitatively close to that of spider capture silk. Further experimental characterization of the created drop-on-coilable-fibre systems was found to agree with predictions from numerical simulations and theory, especially for properties such as the threshold for activation, the existence of an hysteresis, the fine details of the stress-strain curve, or the influence of gravity and of the deformability of the droplet interface.

We further showed that the drop-on-coilable-fibre systems can be enriched by the addition of new degrees of freedom, such as using several fibres, temperature changes or evaporation. This led to the design of actuators and sensors, as well as a new technique for 3D microfabrication, showing the potential of increasingly complex cases of drop-on-coilable-fibre systems, both technologically and academically.

Keywords

Le treuil élasto-capillaire : De la soie d'araignée aux actuateurs intelligents

Résumé

Le but de cette thèse était de comprendre et recréer artificiellement un mécanisme d'autoassemblage faisant appel aux notions de capillarité et d'élasticité dans la soie d'araignée. La fonction première des gouttes de glue microniques qui existent sur la soie d'araignée dîte de capture est de fournir à la toile ses propriétés adhésives, cruciales pour atteindre une efficacité digne d'un piège. Ces gouttes jouent pourtant un autre rôle : elles améliorent de façon spectaculaire les propriétés mécaniques de la soie, et permettent par la même occasion de préserver l'intégrité structurelle de la toile. Ceci est dû à la localisation de l'instabilité de flambage au sein des gouttes de glue, qui sont le site d'une surcompression de la part des ménisques capillaires, ce qui provoque un enroulement local de la fibre, et la retension du système entier. Ceci constitue un microsystème d'enroulement automatique qui tire son énergie de la capillarité, qui sera appelé treuil élasto-capillaire.

La première partie de ma thèse fut dédiée à la caractérisation d'échantillons naturels et à la visualisation du treuil naturel, à travers le réglage de paramètres d'environnement, des observations microscopiques, des mesures de forces sub-micronewtons en compression et en tension, mais aussi de l'analyse d'image et la résolution de problèmes techniques. Les mesures indiquent qu'il y a un rapport intime entre la forme locale de la fibre et les propriétés mécaniques de l'ensemble de l'échantillon. L'existence du phénomène de treuil implique que ce système spécial de gouttes sur fibre se comporte sous compression comme un liquide, alors que sous tension il possède un régime de ressort élastique classique. Les araignées ont donc trouvé un moyen de construire des hybrides mécaniques liquide-solide grâce à une technique de functionalisation induite par forme.

Nous avons utilisé un modèle complètement mécanique pour expliquer ce comportement unique, ainsi qu'une analogie avec le formalisme des transitions de phases. Nous modélisons ce système comme une goutte sur une fibre déformable, et montrons que si l'énergie de mouillage est supérieure à l'énergie de courbure, le système "s'active" et l'enroulement en goutte commence. Des simulations numériques du problème de l'elastica 3D sous compression locale dans un potentiel de confinement mou reproduit le lien observé entre la forme locale de la fibre et la réponse mécanique. Nous fabriquons ensuite des fibres flexibles de taille micronique et longues de plusieurs centimètres par extrusion de polymères thermoplastiques, et montrons que le simple dépôt d'une goutte de liquide mouillant permet par la suite la création efficace d'un système ayant des propriétés mécaniques proches de celles de la soie d'araignée de capture. La caractérisation expérimentale des systèmes de goutte sur fibre enroulable est en accord avec les simulations numériques et la théorie, notamment pour des propriétés telles que le seuil d'activation, l'existence d'un hystérésis, les détails subtils de la courbe contrainte-déformation, ou encore l'influence de la gravité et de la déformabilité de la surface de la goutte. Nous montrons ensuite que les systèmes de goutte sur fibre enroulable peuvent être enrichi par de nouveaux degrés de liberté, tels que l'utilisation de plusieurs fibres, les changements de température ou la possibilité d'évaporation. Ceci a mené à la conception d'actionneurs et de capteurs, ainsi qu'à une nouvelle technique de microfabrication 3D, révélant le potentiel de situations de plus en plus complexes, tant technologiquement qu'académiquement.

Notations

r . . . . Fiber radius

R . . . . Drop radius

D . . . . Drop diameter

E . . . . Young's modulus

I . . . . Second moment of the section of a beam

γ . . . . Surface tension

θ_Y . . . . Contact angle

α . . . . Angle between the rotated meniscii and the fibre main axis

φ . . . . Fibre self-angle

ℓ . . . . Arc length

L . . . . Distance

L_w . . . . Wetted fibre length

L_0 . . . . Rest length

L_{ac} . . . . Fibre length at activation

R_{ac} . . . . Drop radius at activation

ρ . . . . Density

g . . . . Gravitational acceleration

T_g . . . . Glass transition temperature

INDEX

TABLE OF CONTENTS

HISTORY AND CONTEXT OF THE STUDY

"The most exciting phrase to hear in science, the one that heralds new discoveries, is not "Eureka" but "That's funny..." " — Isaac Asimov

Contents

THIS chapter explains the context of this PhD work. From its origin deep in the mind of an Oxford zoology professor, to the enlightenment of its potential in a necessarily unique mechanics lab in Paris. It gives the proper necessary knowledge in spider science, called araneology, presents the spiders we used, and introduces the state of the art in extreme mechanics.

Birth of this study

This PhD originated from observations of spider silk of Vollrath and Edmonds (1989). The team of Prof. Vollrath, the Oxford Silk Group, was working at the time on the influence of water on the mechanical properties of a special kind of spider silk called capture silk. This type of spider silk consists of a thread covered with glue droplets, further described in section 1.2.1. They found that at low humidity, capture silk is stiff and presents a large dissipation over a mechanic cycle. On the other hand, at high humidity, capture silk is much softer and more extensible and dissipates less energy over the same cycle. The most impressive figure is about the extensibility though. From 30% extension at break at 0% relative humidity to up to 1000% at 100% humidity (Omenetto and Kaplan, 2010; Denny, 1976). They proposed an explanation for this observation. At high humidity, there could be tiny coils of threads inside each droplets that boosts extensibility tremendously. These coils have been explained as a consequence of capillarity (see section 1.5). A proof on its side, when compressed and laid down on a microscope slide a capture silk actually shows a coil-like structure within the "post-mortem" droplets, see figure 1.1.

However, this theory has seen much opposition from the araneology community. "The appearance of more or less balling or winding was an experimental artifact. There were never tiny windlasses in

the drops responsible for the elastic properties" writes the fiercest opponent (Schneider, 1995). The manipulation of the samples has been called uncautious, and attempts to recreate the original observation failed. The community preferred to involve biochemistry as explanation to the extraordinary extensibility (Becker et al., 2003). After several replies, no definitive conclusion was set and the topic has fallen into oblivion. Until our team dusts it off, and provided a new look to this open problem. This PhD work aims at settling this 25 years old controversy, showing that the existence of the in-drop coils are indeed possible, in theory and in practice. After all, what happens in the microworld often defies intuition (Dirac, 1958).
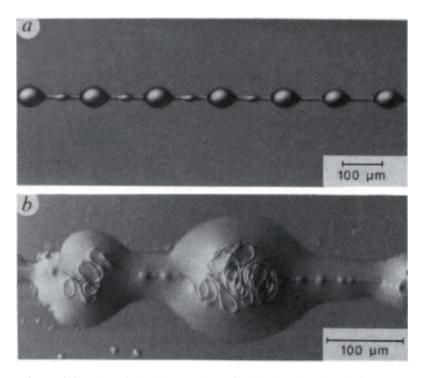
Figure 1.1 – The original observation of Vollrath and Edmonds in 1989.

1.1 Everything you always wanted to know about spiders

... but were afraid to ask.

Spiders, along with snakes, represent what one usually find the creepiest creatures on Earth. Maybe it is their venom. Or their eight legs. Or their numerous eyes (Foelix, 2010). Or their hairy abdomen. Long story short, the ugly is misunderstood and quickly dismissed. Worth to be noted, the social networks are currently spread with the idea that spiders may actually be cute, as in figure 1.2. The following section shows how incredibly diverse and optimized spiders can be, from their behaviour on the herd scale to the fine material design on the nanoscale.

Spider uniqueness Evolution has bestowed an incredible diversity to the spider kingdom, with more than 35000 species, living on every continent except Antartica (Hillyard, 1994). Their body and internal complex architecture is the result of more than 400 million years of evolution (Jacob, 1977; Brunetta and Craig, 2010). Most spiders are known to live and hunt on their own, and thus need an efficient method to capture preys. Spider webs have evolved through natural selection to provide a hunting solution, as very effective insect traps. Their geometry and organisation are optimized for such a purpose, as is discussed in section 1.2. It is worth noting than not all spiders weave a web. Some rely on the frontward discharge

Figure 1.2 – Left: Cute jumping spider. Right: Peacock spider displaying mating ritual. Sources: imgur.com and livescience.com.

of gluey silk, the so-called spitting spiders (Suter and Stratton, 2009). Others tend to use a more classic hunting technique, such as the jumping spider (Jackson and Wilcox, 1998), depicted in figure 1.2.

Spiders cannot feed on solid food. When a prey is captured, the initial bite serves to paralyze it and minimizes the danger of the spider herself being stung or bitten. Enzymes are then injected and liquifies the prey's internal structures. Spiders then simply suck the resulting product (Foelix, 2010). Female spiders are often much larger than their males counterparts (up to six times in Nephilas), a phenomenon called sexual dimorphism (Vollrath and Parker, 1997). Spiders can range in size from 0.37 mm for Patu digua to a staggering 33 cm in body length for the goliath bird-eating tarantula. As it implies, the latter really does eat birds. In order to capture such huge preys, spiders may use webs, but these traps must be very efficient. Their success relies on three properties, elasticity, damping and prey ensnaring (see section 1.2.1). This is done by cleverly tinkering the web structure, encompassing different kinds of silk in a complex structure to make the most of all of its elements (Cranford et al., 2012). Compared to other silk-spinning animals (silkworms (*Bombyx Mori*), crickets (Sutherland et al., 2010) and a recently discovered silk-spinning shrimp (Kronenberger et al., 2012)), spider silk is unique in its very high quality and mechanical properties, allowing a variety of uses. This will be addressed in details in section 1.2. Spiders have a social system based on only one individual. If a spider feels threatened because another spider has come nearby its hunting territory, it may attack the latter, kill it and even feed on it. Spider cannibalism makes breeding difficult, and industrial-scale spider silk factories have been yet an exception because of this low efficiency compared to silkworm silk. For clothing, and any bulk applications, silkworms are highly preferred. Nevertheless, when the application is more demanding and high-quality is required, spider silk is the way to go. It is especially used for its superior mechanical properties (see section 1.2.1) and medical properties (see below).

Medical properties Spider silk enjoys a very complex chemistry, allowing extreme mechanical performance (see section 1.2.1). This also gives spider silk medical properties, employed in many traditional cultures. Peasants in the southern Carpathian Mountains used silk from the Atypus spider to cover their wounds. It was reported to improve healing, and even connected with the skin. This is believed to be due to antiseptic properties of spider silk (Heimer, 1988; Wright, 2011). Silk is also rich in vitamin K, which is effective in clotting blood. The biocompatibility of silk has been a research topic for years (Vepari and Kaplan, 2007). It has been used in the literature to bio-integrate electronics sensors onto brain tissues (Kim et al., 2010), by storing the sensors in a silk-based matrix that can dissolve when in contact with water. It also possesses an incredible potential as a scaffold for culturing neural stem cells (Lewicka et al., 2012).

3

Web automatic hunting   A specific type of spider silk serves for prey capture. These threads rely on a stable aqueous gluey coating (see section 1.3). Due to ion mobility, capture threads are electrically conductive. As the rubbing of the wings on the abdomen rips off some electrons, a flying insect is electrostatically charged. The resulting interaction is an attraction, which make the whole web seem to be attracted by the insect passing by (Ortega and Dudley, 2013; Vollrath and Edmonds, 2013). Although the range of action of this "automatic hunting" technique is limited to a few centimeters, the ability of the web to entrap prey is reinforced.

Influence in human hygiene   Spiders have been shown to have a strong role in the balance of the ecosystem (Nyffeler and Benz, 1987). As insect hunters, and especially insects carrying diseases lethal to human beings, like mosquitoes, spiders are effective protecters. As a matter of fact, when waters flooded nearly a fifth of the land in Pakistan, millions of spiders escaped and climbed up trees where they began spinning webs, as seen on figure 1.3. This turned trees into living mosquito traps. As a consequence, the expected malaria outbreak did not happen, saving many lives.

Figure 1.3 – Trees covered in spider webs after the 2010 great flood in Pakistan. The region avoided a huge outbreak of malaria thanks to the mosquito-eating spiders. Source: globalprosperity.wordpress.com.

Influence in Art   Spider webs were taken as examples for minimal structure, inspirational for architects like Otto Frei, 2015 Pritzker price winner, equivalent to the Nobel prize in architecture (see figure 1.4 (left)). He was one of the few who could be both an engineer and an architect at the same time, blending structural design and architectural finesse. He was noted for his use of lightweight structures, in particular tensile and membrane structures, including the roof of the Olympic Stadium in Munich for the 1972 Summer Olympics. He was much in contrast with the developing architect community that tried to push forward the potential of concrete at that time.

Art has also been influenced by images of spiders. They are often described as dark figures often, symbols of an ancient fear. But they may also be regarded as protective mothers, according to Louise Bourgeois, author of the Maman sculpture, depicted in figure 1.4 (right). "The Spider is an ode to my mother. She was my best friend. Like a spider, my mother was a weaver. My family was in the business of tapestry restoration, and my mother was in charge of the workshop. Like spiders, my mother was very clever. Spiders are friendly presences that eat mosquitoes. We know that mosquitoes spread diseases and are therefore unwanted. So, spiders are helpful and protective, just like my mother." — Louise

Bourgeois.
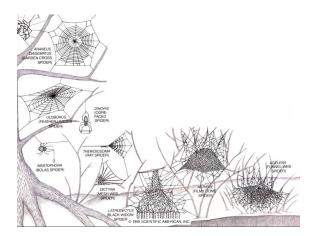
Figure 1.4 – Left: Aviary in the Munich Zoo at Hellabrunn 1979-1980 Munich Germany. Right: "Maman" sculpture in Zurich, Switzerland (temporary location) by Louise Bourgeois. Originals sculptures are at the Tate modern art museum in London, UK and at the Guggenheim museum in Bilbao, Spain. Sources: Atelier Frei Otto Warmbronn (left) and Levan Baski (right).

1.2 Silk factory, up to 7 different silks

There are many types of silks, but even more uses for it. In addition to the common web building, spider silks have many other applications. Among them, silk is used for reproduction. Male spiders may produce sperm webs, and spider eggs are covered in silk cocoons (Foelix, 2010). It is used for dispersal by small spiders too, a technique known as "ballooning" or "kiting" (Humphrey, 1987). When hunting by day, the spider hides under cover nearby. The threads may serve as alarm lines in that case, joining the spider to its web, so that the spider knows when a prey is caught or when a predator is attacking (Foelix, 2010). There are many geometries of webs (Vollrath, 1992), depicted in figure 1.5 (left). They may be regular or not, form a tridimensional structure, be triangular, ladder-like, form a dome or a funnel (Vollrath, 1992). Here we focus on webs of simple geometries, the flat, regular and centered orb webs. The main components of an orb web are the frame threads or structural silk, the radial threads and the capture spiral threads.

The clever composition of the three types of silk is responsible for the most of the toughness of the structure of the spider web (Vollrath, 1992; Cranford et al., 2012). The structural silk is found in the periphery of the web, this is the frame on which holds the rest of the web. The radial threads, as its name implies, run from the center of the web to the outside in a radial fashion. There are typically 30–35 radial threads in a web (Foelix, 2010). The capture threads are found in the spiralling direction of the web, and are deposited last, from the outside towards the center of the web (Vollrath and Mohren, 1985), see figure 1.5. The specific geometry of those webs induces stress localization and overall robustness (Cranford et al., 2012). The capture threads hold their names from their function, as they are gluey and serve for prey entrapment (see section 1.3). The main difference between these different types of threads are their mechanical response and chemical coating (see section 1.2.1). The glands on the abdomen of the spider that make them are different too. The major ampullate gland delivers dragline silk, whereas capture silk is produced in the flagelliform gland, as depicted in figure 1.5 (right). There exist highly different specialised glands in different spiders, ranging from a simple sac with an opening at one end, to the complex, multiple-section Major Ampullate glands of the Nephila golden orb weaving spiders (Dicko et al., 2008). They have been optimized slowly throughout time thanks to evolution.
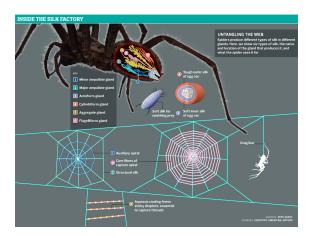
Figure 1.5 – There is a multitude of different spider silks (right) as well as corresponding spider web geometries (left). Source: Vollrath (1992) (left) and Source : Pete Guest (Scientific American, Nature (right)).

1.2.1 Mechanical properties

First described in a 1964 paper by Lucas (1964), the mechanical properties of spider silk are remarkable (Omenetto and Kaplan, 2010; Denny, 1976). The concepts used to quantify mechanical properties are explained in section 1.4.1. Spider silk might not be exceptional regarding its rigidity (5–10 GPa), to be compared with 70 GPa for glass or 300 GPa. Nor for its extensibilty (30% for dragline silk, to be compared with 200% for common rubber band). The combination of both is exceptional. This corresponds to a high toughness (or work to fracture), which is approximately the product of rigidity and extensibility. Spider silk has a toughness of 150 MJ m^{-3}, threefold that of Kevlar$^{®}$. The highest toughness has been observed in the silk of the Giant Riverine Orb Spider at 350 MJ m^{-3} and up to 520 MJ m^{-3}, ten times higher than Kevlar (Agnarsson et al., 2010). These amazing properties come from a very specific nanostructure. Inside a typical fibre there are crystalline regions (highly ordered) separated by amorphous linkages (disordered). Silks, as well as many other biomaterials, have a hierarchical structure, as cellulose or hair do. The primary structure is its amino acid sequence, mainly consisting of highly repetitive glycine and alanine blocks (Simmons et al., 1996). Amino acids are the main constituents of proteins. They are composed of a carboxylic acid functional group $-C\underset{\diagdown O}{\overset{\diagup OH}{}}$ at one end and an amine group $-NH_2$ at the other end, along with a side-chain specific to each amino acid. Glycine is the smallest amino-acid possible encoded by the genetic code, with a single hydrogen as side-chain. Alanine is the second smallest amino-acid, with a simple $-CH_3$ group as side chain. On a secondary structure level, alanine is mainly found in the crystalline domains, while glycine is in the so-called amorphous matrix (Van Beek et al., 2002). Becker et al. (2003) proposed that the glycine-rich flagelliform proteins (the main constituent of capture silk) would act as nanosprings and unfold under strain to provide tension, as seen in figure 1.6 (left). It is the interplay between the hard crystalline segments and the extensible amorphous regions that gives spider silk its unique properties (Liu et al., 2007; Gosline et al., 1984). This complex structure calls for a controlled spinning process. Silks are produced in internal glands, depicted on figure 1.5 (right). After the gland comes the storage sac, where silk is kept available in case of need, in the form of "silk dope" (Vollrath and Knight, 2001). The latter consists of silk proteins dissolved in water, a nanocomposite state of biological matter defined as an "aquamelt" (Holland et al., 2012). It is in a liquid crystal state, highly ordered while able to flow through the duct (Vollrath and Knight, 2001). Each duct is terminated with an external (visible) part called the spinneret,

shown on figure 1.6 (right).
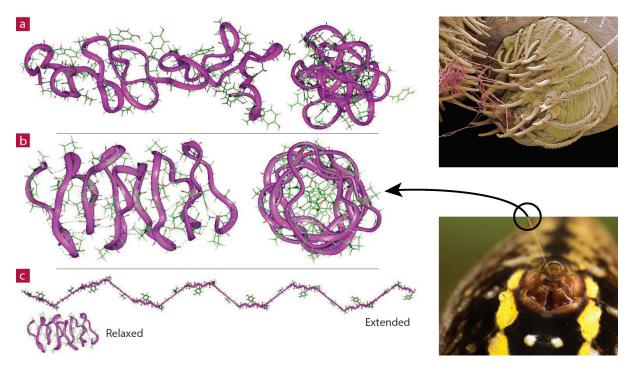
Figure 1.6 – Left: Flagelliform silk proteins are rich in soft and stretchy glycine groups. They are involved in spider capture silk elasticity as nanosprings. Side and end views for possible flagelliform protein conformations of (a) *Araneus gemmoide*,and (b) *Nephila clavipes*. Right: Views of the spinneret of an *Argiope trifeasciata*, during spinning (bottom right) and under post-mortem very high resolution Scanning Electron Microscopy in false colours (upper right). Sources: Becker et al. (2003) (left) Forsyth Photography (upper right) and Steve Gschmeissner (bottom right).

Depending on the complexity of the species, spiders will have two to eight sets of spinnerets, usually coming in pairs. The parity of the spinneret sets are explained by bilateral symmetry, the same biological concept that make us have two arms and two legs. This means that a silk thread is actually composed of two fibres bundled together, so that there is a backup thread in case one breaks. The spinneret is specifically tuned to provide constant shear stress, important to induce controlled crystallization (Holland et al., 2012). The small size of the fibres are of importance. Materials on the micro scale are more rigid than their bulk equivalent, because of low defect concentration (Gordon, 2003). Furthermore, geometrical effects increase orientation of the crystals and thus brings an extra source of toughness (Porter et al., 2012). Additionally, this allows for solidification of the fibres as water is drawn out. Even after silk has been spun, it retains a high influenceability by water. At high relative humidity, water disrupts the hydrogen bonds and change the order of the proteins at the molecular level. This leads to a significant drop in crystallinity, and consequently a thousandfold reduction in rigidity, with an increase in extensibility. This phenomenon is called the glass transition. Figure 1.7 shows comparisons between wet (natural state) and dried capture threads. The latter ressembles strongly radial thread, implying that the two types of threads are closely related (Vollrath and Edmonds, 1989).

Glass transition can be also obtained by changes in temperature. The critical temperature and the critical relative humidity for rigidity loss are related (Plaza et al., 2006), allowing some freedom to tune mechanical properties. Details will be given in section 5.3.1 where this effect is used effectively. In order to fulfill its goal and catch a prey, a web must be able to avoid breaking when impacted by a flying
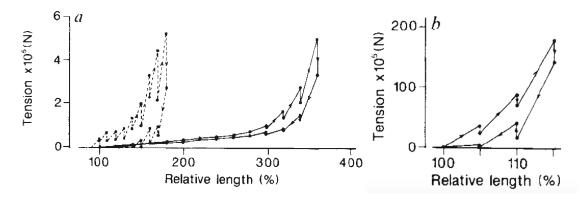
Figure 1.7 – Influence of water on the mechanical properties of capture silk (Vollrath and Edmonds, 1989). (a) Comparison between wet (full line) and dried (broken line) spiral capture threads. (b) Force-strain measurement for a radial thread. Notice the resemblance between the dried capture thread and the radial thread, implying a strong relation between the two types of threads.

insect, but also to stop the prey quickly and not to have it rebound. The prey entrapment process is thus in two stages. First, the insect is slowed down and stopped. To do so, the damping properties of the web have to be excellent. There are several sources of damping, be it aerodynamic or viscous. This will be developped further in section 2.3. Secondly, the insect must be prevented from escaping, until the spider has time to reach it, which is related to the efficiency of the capture threads.

1.3 Virtues of the capture thread

There are two kinds of capture silk. The older (evolutionarily speaking) cribellate silk uses dry adhesion through Van Der Waals interactions of electrostatically charged nanofibres (Vollrath, 2006). The description of this silk is developed in appendix A, and differences between the two types of threads are highlighted experimentally (Elettro et al., 2015). The newer capture thread, ecribellate silk, uses wet adhesion and supports tiny (50 μm) glue droplets (see section 1.3.1). Ecribellate orb spiders rely on the remarkable extensibility (up to almost 1000% at 100% relative humidity) of their capture spiral threads to intercept and entrap preys (Gosline et al., 1986). The glue droplets retain the preys within the trap.

The droplets on ecribellate capture silk contain different chemicals that increase its performance, see section 1.3.1. Acidic salts like potassium dihydrogen phosphate releases protons in aqueous solution, resulting in a pH of about 4, making the silk acidic and thus protecting it from fungi and bacteria that would otherwise digest the protein. The droplets contain a high concentration of the neurotransmitter GABA, which provides them with hygroscopic properties, stabilizing them against evaporation by absorbing air moisture. This is a necessary condition for them to function properly (Vollrath et al., 1990; Edmonds and Vollrath, 1992). This property is extremely important for the glue to be worth spinning, as the lifetime of normal micronic water droplets is on the order of a few seconds (see section 3.3.1). Moreover after each (few) day(s), when the spider eats and recycles its web damaged by natural elements, hygroscopic droplets provide a substantial water intake (Edmonds and Vollrath, 1992). Furthermore drop stickiness changes with relative humidity, helping to trap different kinds of preys by day or by night (Opell et al., 2011).

1.3.1 Optimized glue performance

Glue performance is the criteria that drives evolution of spider capture silk (Opell, 1999), along with web damping properties. The adhesion has several sources. The fluid nature of the glue droplet provides

it with adhesive properties. This arises from the capillary forces due to the thin liquid bridge connecting the silk fibre and the contacted solid (Bico et al., 2004; Gay, 2002), for instance body hairs of insects. A single liquid meniscus may not be very strong, but upscaling the number of meniscii to thousands may build up a significant force, as in the protection method found by the beetle *Hemisphaerota cyanea*, described in figure 1.16. The high lineic concentration of droplets on the threads builds a good contact to any prey that may impact the web.

A second source of adhesion from the liquid nature of the glue is the viscous adhesion. This is typically what keeps the coaster stuck under your cool pint of beer for tens of seconds on a warm and humid summer day. This can be thought of as an extensional flow of a liquid layer, where the force is $F \propto \frac{R^4}{h^3(t)} \frac{dh}{dt} \eta$ with R the radius of the layer, $h(t)$ its instantaneous thickness, η the fluid viscosity. This is called the Stefan apparent adhesion (Stefan, 1874). Notice the strong divergence of the sustainable force and time when the fluid layer thickness enters the micronic world.

The most important source of adhesion of the ecribellate glue droplet is its elastic adhesion. While Newtonian fluids like water are restricted to the two aforementionned adhesion processes, silk droplets enjoy additional adhesion sources by building up elastic stresses. The droplets are charged with glyco-proteins (long biopolymers) that give them a viscoelastic behavior, even at the faintest concentrations (Amarouchene et al., 2001). When glue droplets are flattened against a surface, their proteins condense and polymerize to provide anchoring, behaving like a viscoelastic solid (Opell and Hendricks, 2010; Blackledge et al., 2010). The adhesion properties are consequently improved a hundredfold and the web can thus keep much bigger preys trapped, helpless until the spider comes to deliver its final fate.

1.4 Extreme mechanics

In this section are presented the fundamental tools needed to understand the concept of the windlass mechanism. The intuitive picture of elastic structures deformation would take into account only the curvature energy of the thread coiled within a droplet. But as will be detailed in section 4.2, the windlass mechanism manages to turn a global low curvature diluted over an entire buckled structure, into a localized high curvature concentrated in the liquid droplet. At first sight, it looks energetically not favorable at all. What is next will bring sense to this apparent paradox.

1.4.1 Elasticity, or the mechanical properties of materials in tension

How much a material deforms under a given force has been a topic of interest as soon as Man began building. But it was not before the seventeenth century that a proper scientific approach was undertaken seriously. Early studies were conducted by Galileo, and later formalized by Robert Hooke. He first stated the law in 1660 as a Latin anagram. He published the solution of his anagram in 1678 as: *"ut tensio, sic vis"*, which means "as the extension, so the force". He found that the applied force was proportional to the observed strain of a material. The coefficient of proportionality defines the stiffness k. This stiffness depends on the size of the sample used, but it is possible to rescale it in order to make it size independent. The intensive property of a solid material that defines its intrinsic rigidity is called the Young's modulus and can be expressed in term of the stiffness as $E = \frac{kL_0}{S_0}$, with L_0 the length at rest of the sample and S_0 the area of the cross section of the sample perpendicular to the axis about which the tensile force is applied. This leads to a linear relationship between applied force and observed strain:

$$\frac{F}{S_0} = E \frac{L - L_0}{L_0} \tag{1.1}$$

where F is the force applied to the sample and L is the actual length after application of F. Typical values for the Young's modulus range from very soft biological tissue like cell membrane (1

9

kPa, Hochmuth et al. (1973)) up to very rigid diamond and carbon nanotubes (1 TPa, Treacy et al. (1996)).Common materials like Nylon® have an intermediate value of 3GPa, while rubber bands have a Young's modulus of 10 MPa. Combined with how much the material can deform before fracture, one obtains the theoretical fracture energy, otherwise called toughness, as the area beneath the stress-strain curve, which is the product of stress and strain as a first approximation.

Equation (1.1) allows calculation of the actual length both under positive and negative force, i.e. under tension or compression. However, above a certain threshold of compression, an elastic instability occurs. This is presented below.

1.4.2 Buckling mechanics

Buckling is the bending of an elastic structure out of its main axis as a result of compression. It occurs whenever bending is energetically more favorable than further compression. Early studies on buckling were conducted by Euler in Lausanne in 1744 (Euler, 1744). This followed the groundbreaking work of Galileo on bending mechanics, depicted in figure 1.8.
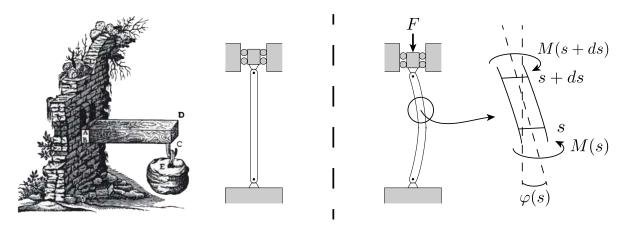
Figure 1.8 – Left: Galileo's explanation of a bending test using a cantilever beam supported by a wall and bent under a rock weight. Right: Sketch of the buckling of a beam under uniaxial compression. s is the curvilinear abscissa, $\varphi(s)$ the local deviation angle, and $M(s)$ the local bending moment. Source: Timoshenko (1983) (left).

The observed deformation of the beam is due to the competition between compression and bending. The resistance to bending of a beam can be quantified with the bending rigidity modulus EI, where E is the Young's modulus and I the second moment of the section of the beam. For a circular cross section of radius r, the second moment is equal to $I = \frac{\pi r^4}{4}$. For a compression test of amplitude F along the main axis of a beam, the local deviation angle of the beam $\varphi(s)$ (with s the curvilinear abscissa) is given by the equilibrium between the moment due to compression and the bending resistance:

$$EI\frac{d^2\,\varphi(s)}{ds^2} = -F\sin\varphi(s) \tag{1.2}$$

This equation is non linear, and must be considered as such to model the behavior of a beam in large deflection in a realistic manner. However, the buckling threshold may be found by linearizing the sine function. With such an approximation, $\varphi(s)$ is given as a linear combination of sine and cosine, with a natural wavelength $\lambda = \sqrt{\dfrac{EI}{F}}$. The boundary conditions yields the buckling threshold. Below the threshold, the beam retains its straight shape, whereas above the threshold, the beam is curved. Equation (1.2) is equivalent to the classical pendulum dynamical equation. The analogy is physically

striking when one replaces the space parameter s by time. The wavelength λ is thus analogous to the classical pendulum period $T \propto \sqrt{\frac{\ell}{g}}$, with ℓ the length of the pendulum and g the gravitational acceleration (Roman et al., 2001).

The force threshold is thus found to be $F_{\text{Buck}} = \alpha \frac{EI}{L^2}$. The coefficient α depends on the anchoring conditions at the beam ends, clamped, pinned (fixed but free to rotate) or totally free. In the case of a beam pinned at both ends like the one depicted on figure 1.8, we have $\alpha = \pi^2$. It is interesting to note that a beam forced in compression against a wall is equivalent to a beam compressed symetrically at both ends, as the boundary conditions are equivalent when one consider the reaction force of the wall (Gordon, 2003). This will help us to quantify the mechanical behavior of the windlass systems and to draw a faithful model of the spider capture silk.

Examples of buckling in biological systems   The mechanics of buckling have been applied in the literature to many biological systems, such as trees, viruses or underwater plants. It is indeed possible to find the maximum height of a tree under consideration of self-buckling. A tree of radius could not be higher than a certain height, as it would buckle under its own weight otherwise. This gives values for the trees height of roughly 100 m, which is quite close to reality (Koch et al., 2004). The buckling instability also dictates the shape of viruses, as the spherical capsids become unstable if too large (Lidmar et al., 2003). Buckling is also used as a tool to induce movements faster than muscles would allow (Skotheim and Mahadevan, 2005). Instances are found for carnivorous plants like the snapping for prey capture of the Venus flytrap (Forterre et al., 2005), shown on figure 1.9 or the ultrafast underwater suction trap of *Utricularia* species (Vincent et al., 2011). Another plant, the fern sporangium, has evolved the remarkable possibility of using buckling as a catapult to spread its spores and colonize its environment (Noblin et al., 2012).

Figure 1.9 – A Venus flytrap snaps under buckling when slightly touched, allowing very fast prey capture. Source: Forterre et al. (2005).

A new vision of buckling   Hystorically, buckling was avoided at all costs by engineers as it leads to failure of a structure. But as shown above, buckling may actually be a powerful method to induce functionalization. Shim et al. (2012) showed that a spherical shell with partial holes would buckle under internal depression, and have a negative Poisson ratio, see figure 1.10. This is a case of metamaterials – materials not found in nature – that expands laterally when stretched, in contrast to common material behavior that contracts laterally under stretching. The underlying idea is actually that the functionalisation is induced by geometry. It has been shown in the literature that an elastic helix in much softer that the material it is made of (Jung et al., 2014) and that egg-shaped shells have a rigidity that depends in their curvature (Lazarus et al., 2012). An interesting application is the use of the buckling phenomenon as

a reserve of apparent extensibility in the fast-growing field of flexible electronics (Rogers et al., 2010), which will be discussed in section 5.1.
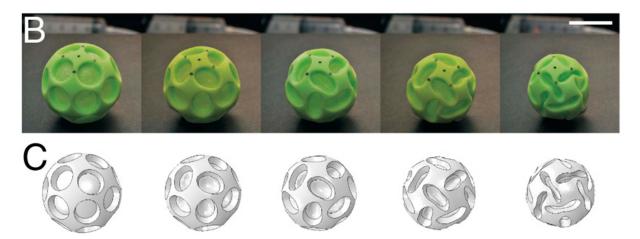
Figure 1.10 – Shape-induced functionalisation of a sphere. It undergoes a structural transformation induced by buckling under pressure loading. Source: Shim et al. (2012).

1.4.3 Surface tension

Surface tension was first observed as the result of capillary action, where a liquid meniscus overcomes gravity when a small tube (a capillary) is dipped in a bath of liquid (Pomeau and Villermaux, 2006). This was made sense of in 1805 by Thomas Young and completed by Pierre-Simon Laplace (Laplace, 1805). Carl Friedrich Gauss unified the work of Young and Laplace in 1830 (Gauss, 1830), deriving an energetical formulation of surface tension effects from Bernoulli's virtual work principles. Surface tension results from the cohesive forces within a liquid. It is represented by the symbol γ and has the dimension of an energy per unit area or equivalently of a force per unit length. It represents an effective force per unit length of liquid meniscus. The molecules at a liquid interface are not energetically equivalent to the ones in the bulk as they experience the proximity of a different medium, and thus a non-symmetric force repartition, see figure 1.11. The liquid molecules tend to stay together, due to the liquid cohesion and chemical affinity.
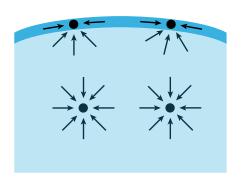
Figure 1.11 – Left: Sketch of the origin of surface tension. The cohesion of the liquid and weaker interaction with the ambient medium explains surface tension as a consequence of the existence of an interface. Right: An everyday experiment to prove the existence of surface tension. A object denser than water may float in certain conditions. Source: Vella and Mahadevan (2005) (right).

A straightforward consequence of the existence of surface tension is the natural likelihood of liquids to minimize the surface that is exposed to the ambient medium. This leads to the pearling phenomenon, where fluid interfaces adapt a spherical shape, typically observed in bubbles. The existence of a surface energy has several daily life consequences, such as the possibility to float objects denser than the supporting liquid (Vella and Mahadevan (2005), see figure 1.12 (right)), the formation of uniquely sized droplets when a tap is opened (De Gennes et al., 2004), or the famous tears of wine, shown on figure 1.12.

Figure 1.12 – Left : The tears of wine result from an equilibrium between gravity, capillarity and evaporation. (Source : "Wine legs shadow" by FlagSteward.) Right : The famous Rayleigh-Plateau instability, or tap instability, an everyday kitchen experience. Source: Flicker.com.

The existence of surface tension shapes all liquid interfaces. When free, all liquid interfaces tend to be spherical, like bubbles in a pint of beer. But not all bubbles are equal, size matters. As surface tension represents an energetical cost to create an unit area, the smaller bubbles have a higher energy, owing to their higher surface to volume ratio. This energy difference is equivalent to a pressure called the Laplace pressure (Laplace, 1805; De Gennes et al., 2004), which reflects the difference between the inside of the bubble (or droplet) and the outside ambient medium. It is proportional to the tridimensionnal curvature of the liquid interface, so that for a sphere, the Laplace pressure is $\Delta P = \frac{2\gamma}{R}$ with R the radius of the spherical droplet, and γ the surface tension of the interface between the liquid and the ambient medium. Typical values for γ are 72 mN m^{-1} for a droplet of water in the air, or 22 mN m^{-1} for a bubble of air in ethanol. The highest values are found for metallic liquids, such as mercury with almost 500 mN m^{-1}. In practice, the Laplace pressure has significant values only for bubbles typically smaller than 10 µm and diverges quickly for nanobubbles, reaching tens of atmospheres easily. The curvature dependence of the Laplace pressure has multiple consequences. For instance, smaller drops disappear in favor of larger ones in an emulsion, a process known as the Ostwald ripening (Ostwald, 1896). They will also be evaporating at a much higher rate in an aerosol, as will be seen in section 3.3.1. When in competition with other forces, surface tension may be the force restoring equilibrium. For instance, when growing a puddle, gravity pulls it down, while surface tension tends to keep a spherical shape. There is a transition between a capillary regime and a gravity-dominated regime when the system reaches the lengthscale $\ell_{\text{gc}} = \sqrt{\frac{\gamma}{\rho g}}$ where ρ represents the density of the liquid. Below ℓ_{gc}, the drop is quasi-spherical, whereas above ℓ_{gc}, the drop is flattened (De Gennes et al., 2004).

When in interaction with another material (solid, liquid or gas), the equilibrium shape of the liquid interface depends upon the balance of the energies in the whole system. There are three interfaces here, each with its specific energy per unit area. We thus define γ_{sl}, γ_{sv}, γ_{lv} the surface energies of the solid-liquid, the solid-vapor and the liquid-vapor interfaces respectively (De Gennes et al., 2004). In the case of a droplet on a rigid substrate, a contact line develops at the intersection of the three interfaces (De Gennes et al., 2004). A force exists along every interface, each with different magnitudes and directions. The horizontal force balance yields the Young-Dupré equation, connecting the forces at stake with the geometry of the interface.

$$\gamma_{lv} \cos \theta_Y = \gamma_{sv} - \gamma_{sl} \qquad (1.3)$$

θ_Y represents the Young-Dupré contact angle, and is the angle between the horizontal plane and the tangent to the drop's shape at the contact line, see figure 1.13.
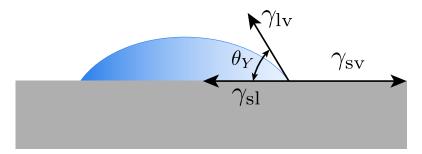
Figure 1.13 – The shape of a drop on a substrate is given by the equilibrium between the energy of interaction between the solid, the liquid and the surrounding gas. A force balance leads to the famous Young-Dupré equation, see equation (1.3).
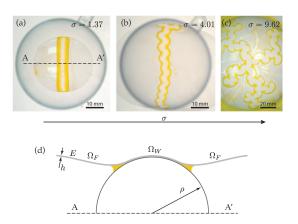
If $\theta_Y > \pi/2$, the liquid does not spread and is said non-wetting. This is the case for high energy liquids on low energy solids, for instance water on Teflon®. The extreme case of $\theta_Y = \pi$ is perfect non wetting and is achieved by lotus leaves for self-cleaning purpose (Gao and McCarthy, 2006; Lafuma and Quéré, 2003). If $\theta_Y < \pi/2$, the liquid spreads and is thus wetting, as silicone oil on glass. In the case of a drop on a fibre, the contact angle influences the shape of the drop from the cylindrical axisymmetry of the fibre (for $\theta_Y \rightarrow 0$) to a spherical shape ($\theta_Y = \pi/2$). The drop may lose its axysimmetry under certain cases. This will be discussed in appendix B.1. The contact angle is also very important in the drop-on-fibre system to determine the nature of the forces acting on the fibre, tensile or compressive. A technique to measure such forces with great precision is explained in appendix B.2.

1.4.4 Elasto-capillary interactions

The so-called elasto-capillary interactions are a sub-domain of the fluid-structure interactions, in which a solid structure and a fluid are coupled and may influence each other. It has long been thought that because of their lightweightness, fluids could not influence the behavior of solid structures. But like a flag in the wind, in 1940 the Tacoma Narrows bridge experienced flutter and eventually collapsed. This was due to aeroelastic flutter, a well known fluid structure instability nowadays. Although regrettable, this accident has lead to the most important theoretical advance in the bridge engineering field of the decade (Moisseiff and Lienhard, 1933; Scott, 2001). Despite its potentially destructive consequences, fluid-structure interactions were tamed successfully. This lead for instance to better control of safety protocols in commercial aircrafts (Flügge-Lotz and Flügge, 1973). In the process, much fundamental discoveries were achieved.

Here we focus on a specific type of fluid-structure interactions, which involve the capillarity of fluid

interfaces in contact with elastic structures. These elasto-capillary interactions explain several everyday phenomenon. Why are dry hairs well spaced, whereas wet hairs form bundles (Bico et al., 2004) ? This is due to capillary bridges between hairs and to their high flexibility over a long distance. Elastic deformations due to capillary adhesion are beautifully visualized when a flat elastic structure (a plastic sheet) is placed onto a wetted sphere, see figure 1.14 (left). This effect allows control of capillary-driven self-assembly of micro-pillars, creating cellular-like carbon nanotubes forests (Chakrapani et al., 2004) or beautiful aggregate patterns of nanofilaments (De Volder and Hart, 2013), shown on figure 1.14. This is also a powerful tool to create tridimensionnal structures from bidimensionnal templates, otherwise very complex to make by conventional techniques (Syms et al., 2003; Roman and Bico, 2010).
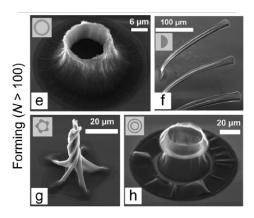
Figure 1.14 – Elasto-capillary buckling of a plastic sheet on a sphere (Hure and Audoly, 2013) (left). The resulting equilibrium depends on the strength of adhesion compared to the stiffness of the film. Beautiful aggregation patterns formed from an array of nano-pillars (De Volder and Hart, 2013) (right).

The addition of an electric field changes the energy balance through the addition of a capacitance energy, which opposes surface tension. This may lead to the overriding of surface tension (Pineirua et al., 2010), see figure 1.15. In the case of a simple droplet, this leads to the Taylor cone instability, which is used in section 5.2. For a thin elastic membrane wrapped around a droplet by wetting interactions (known as capillary origami (Gracias et al., 2002; Py et al., 2007)), the system can thus be folded and unfolded at will using an electrode in contact with the droplet.
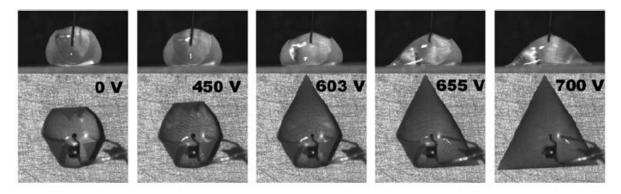
Figure 1.15 – Proof of concept of electro-elasto-capillarity. By use of an electric field, one can override the influence of surface tension. Source: Pineirua et al. (2010).

Elasto-capillary interactions are at their strongest in soft solids and small systems, where capillary forces become stronger than bulk effects. These conditions are found particularly easily in Nature. For

instance, the soft lungs airways of neo-natal babies may collapse because of the biological liquid coating, forbidding first air intake (Heil, 1999). Capillary is also used by the *Hemisphaerota cyanea* beetle to protect from ant attacks. Its fighting technique is to secrete an oil that wets the solid on which it sits, along with the hundred of thousands of small bristles on its feet, depicted in figure 1.16. The numerous meniscii can resist an upward traction, which ants use as a fighting technique, by building tensile elastic stress. Elasto-capillarity provides directionality to the adhesion. As the beetle advances its legs and shears the bristles, they bend and release stress (Eisner and Aneshansley, 2000).
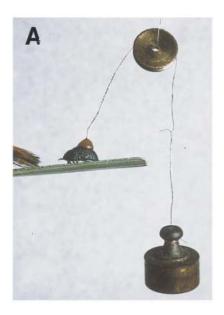
Figure 1.16 – The *Hemisphaerota cyanea* beetle uses capillary adhesion to protect itself against forced roll-over and can resist pull-up forces $60\times$ its own weight. Elasto-capillarity allows directional adhesion, so that the protection is reversible (Eisner and Aneshansley, 2000).

The field of elasto-capillarity is young and fast growing. The field of the drop-on-fibre system is older, and dates back to the 1930s, when textile technology was growing (Adam, 1937). There has been attempts to use elegant geometry-induced softness (see section 1.4.2) to induce elasto-capillary macroscopic deformations in drop-on-fibre systems. Although the physical ingredients are similar, the mechanical properties of the resulting system are very different from the windlass mechanism (Jung et al., 2014).

1.5 Critical radius of coilable fibre

As explained in section 1.4.3, surface tension can be interpreted as a force per unit length of meniscus. The meniscus is the triple interface between the liquid droplet, the solid substrate and the ambient medium. In a drop-on-fibre system, each meniscus as a length $2\pi r$ (with r the radius of the fibre), assuming an axysimmetrical shape. The exact shape of the drop (on fibre) an its consequences will be discussed in appendix B.1. Locally, the contact line is tilted by the contact angle θ_Y with respect to the fibre axis (see section 1.4.3). Integrating each portion of the meniscus orthoradially around the fibre axis yields the meniscus capillary force $2\pi\gamma r \cos\theta_Y$, where γ is the surface tension of the liquid, r the radius of the fibre and θ_Y the contact angle. If $\theta_Y < \pi/2$, the liquid wets the fibre and tends to adopt a cylindrical shape, in contradiction to the minimization of liquid-air interface, that would require a spherical shape. There is thus an equilibrium inward meniscus force, that is compressive. If this com-

pressive force is higher than the buckling threshold discussed in section 1.4.2, then the part of the fibre that resides inside the droplet buckles, as depicted on figure 1.17.
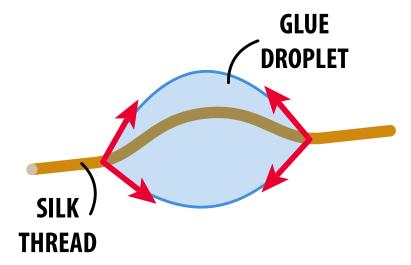
Figure 1.17 – Sketch of the initiation of the coiling process. Through capillary forces, the droplet compresses the fibre inward and induces buckling. The final equilibrium is different than the classical drop-on-fibre system.

The possibility of buckling therefore brings a new degree of freedom to the system and changes its very nature (see section 4.2). As such, after out-of-axis deformation, the fibre offers much less resistance to compression. As a consequence, the fibre may be coiled and "swallowed in" as the liquid meniscii slide on the fibre during compression. This mechanism could explain the initial observation made by Vollrath & al. in 1989, shown on figure 1.1. This will be further discussed in sections 2.2 and 3.1.

The picture of liquid meniscii brings us to assume the meniscii to apply pinned local boundary conditions on the fibre, which means a freedom of rotation for the fibre at the droplet entrance, and no accumulated moment. This assumption gives the numerical factor to predict accurately the threshold of buckling.

Capillary compression > Local buckling threshold

$$2\pi\gamma r \cos\theta_Y > \pi^2 \frac{EI}{(2R)^2} \qquad \Rightarrow R > R_{\text{ac}} = \sqrt{\frac{\pi^2 E r^3}{32\gamma\cos\theta_Y}} \qquad (1.4)$$

where E is the Young's modulus of the fibre, I the second moment of the section of the fibre, and R the actual radius of the droplet. In practice, the latter is measured as half of the drop length, which corresponds to the inter-meniscii spanning distance. R_{ac} denotes the critical drop's radius above which the windlass system is activated. For ease of calculation, we assume that the drop has a quasi-spherical shape. This yields a single parameter to describe the entire drop, its radius R. This view differs slightly from real conditions. This is further discussed in appendix B.1, where we show that this difference is negligible for our experimental conditions.

Under compression, a coilable fibre would begin to coil at a fibre length slightly below the rest length, with a compression strain of $\epsilon \approx \frac{\pi^2}{16}\left(\frac{r}{R}\right)^2$. This is on the order of 0.01% for our typical drop-on-(coilable)-fibre systems. This is thus neglected in the following discussion.

If the drop radius can be increased at will, the onset of buckling will eventually be reached for any fibre made of any material. To put figures in, a steel bar with a 10 cm diameter could be bend by a water droplet... if the latter was 35 km in diametre ! The idea is of course possible in space but not

achievable down here. Nevertheless, the concept has been used to upscale the experiment efficiently in section 5.5. A more realistic version of the windlass mechanism must take into account the fact that a fibre can hold only a finite amount of liquid (Lorenceau et al., 2004). This means that the capillary meniscii must counteract the weight of the drop. This leads to an upper bound for the drop size, given in equation (1.5).

Two meniscii force > Drop's weight

$$2 \times 2\pi\gamma r \cos\theta_Y > \frac{4}{3}\pi R^3 \rho g \qquad \Rightarrow R < R_{\max} = \left(\frac{3\gamma \cos\theta_Y}{\rho g}\right)^{1/3} r^{1/3} \tag{1.5}$$

with ρ is the density of the liquid of the droplet, assuming that it is quasi-spherical, and g is the gravitational acceleration. In the case of an ambient medium of density ρ_0, Archimedes' force counterbalances gravity, thus ρ would be replaced by $\Delta\rho = \rho - \rho_0$. The combination of equations (1.4) and (1.5) yields a criteria to be met for coilability:

$$r < r_{\text{crit}} \quad \text{with} \quad r_{\text{crit}} \approx 2.3 \frac{(\gamma \cos\theta_Y)^{5/7}}{(\rho g)^{2/7} E^{3/7}} \tag{1.6}$$

The exact numerical coefficient is $\dfrac{32^{\frac{3}{7}} 3^{\frac{2}{7}}}{\pi^{\frac{6}{7}}} \approx 2.3$. Typical values for the critical (maximum) fibre radius combined with a silicone oil droplet are 220nm for glass fibres ($E_{\text{Glass}} = 70$ GPa), 850 nm for Nylon® ($E_{\text{Nylon}} = 3$ GPa) and 30 µm for soft rubbery materials ($E_{\text{PDMS}} = 1$ MPa). As expected, the windlass effect belongs to the nano/micro world, where capillary phenomena overtake elastic deformations and weight, and it is indeed the size range of the spider silk threads. This criteria is refined in section 4.6 where we show that the scaling law is conserved.

In the next chapter, we show that the windlass mechanism is indeed possible and is observed it in natural silk samples. We further discuss the biological importance of this mechanism for the spider realm.

"Aerodynamically, the bumble bee shouldn't be able to fly, but the bumble bee doesn't know it so it goes on flying anyway." — *Mary Kay Ash*

Contents

THIS chapter offers a description of the windlass mechanism, observed in natural samples of spider capture silk. Despite the state-of-the-art context, it is shown that micro windlasses do exist in natural spider silk samples, therefore putting an end to a 25 years old controversy.

2.1 Confusion in literature: an unsolved problem

The citation at the beginning of this chapter roots from an urban legend according to which an engineer and a biologist where having a drink and began discussing of their own field. The biologist threw a dare to the engineer, to work out how a bee flew. The engineer, keen to show off his skills, quickly wrote down a few calculations and came to the conclusion that a bee should not be able to fly. To put it simply, it is possible to "prove" that a bumblebee cannot fly if you perform an extremely crude calculation (like forgetting to take into account things like the rate of flapping, the rotation of the wing, or the action of vortices), but a full aerodynamic calculation (to say nothing of getting all empirical and watching a bumblebee fly) will show that the bumblebee's flight works perfectly fine.

The same idea holds for our case. Considering only the fibre as a structure independent of its droplets is an unrealistic assumption and leads to the conclusion that the windlass is counterintuitive. This is the source of the confusion and debate that took place in the 90s in the araneology community (Schneider, 1995; Blackledge et al., 2005).

Difficulty of observation

As explained in chapter 1, the hypothesis according to which silk thread would coil within glue droplets has seen much opposition from the araneology community. The observations presented by Vollrath and Edmonds (Vollrath and Edmonds, 1989) left part of the community unconvinced because they had

been performed in an indirect manner on "post-mortem" samples laid down on a microscope slide (see figure 1.1). Subsequent attempts to produce direct optical observations failed.

In our understanding, this practical difficulty might be due to the specific interactions of silk with water. As explained in section 1.2.1, the silk raw material is stored within the spider organs as a liquid crystal with water as solvent. This has a strong effect on capture silk threads, in particular the fact that it is in a rubbery state at room temperature. It might also induce creeping of water within the thread. As a consequence, the optical boundary between water and the thread is destroyed. Upon deposition on a glass slide, the glue droplet spreads and releases its water content on the surface. This dries the inner thread and restores the optical index contrast, thus allowing observation.

The first silk samples we tried came from local spiders from the Paris gardens and bridges, presented in section 2.2.1. Like previous studies, we could not observe directly the fibre coiling within the droplets, whatever the optical techniques we used. However, other parameters like dynamic retightening and force-displacement curves (see section 2.2.3) were evidences of the presence of the windlass mechanism and a motivation to push forward. After nearly a year of trials, we decided to change the spider species. The longer and wider samples of large exotic spiders made them a good testing ground for further trial. We found that the relatively thicker exotic capture silk samples has slightly different optical interactions with the glue droplet content and that the thread was actually still visible within the droplet. The methods to observe the fibre coiling in practice are explained below.

2.2 Observation of the windlass

2.2.1 Presentation of the spiders we used

Larinioides Sclopetarius and _Araneus Diadematus_ *Larinioides Sclopetarius* is commonly known as the "bridge spider". It is a relatively large orb-weaving spider that is often found on bridges, especially near light and over water. The species tends to live on steel objects and is seldom seen on vegetation. Females reach body length of 10–14 mm, males 8–9 mm. Their orb webs can have diameters of up to 70 cm. They often hide during the day, and wait for prey in the center of their web at night. Males can be found mostly during summer, females are active until november in Central Europe (Foelix, 2010). This species is of convenience because of the proximity of the campus to the river Seine and its many bridges. The "spider hunting" was carried out at dusk, when the spiders began to reach out of their nest for their web, see figure 2.1 (left).

Alternatively, *Araneus Diadematus* was used, also called the "european garden spider". Thus the proximity of the "Jardin des Plantes" made for a convenient sample source as well. The webs are built by the larger females who hang head down in the center of the web or remain hidden in nearby foliage, with one claw hooked to a signal line connected to the main orb web waiting for a disturbance to signal the arrival of a prey. The prey is then quickly bitten and wrapped in silk before being stored for later consumption. Like *Larinioides Sclopetarius*, *Araneus Diadematus* weave large and regular webs compared to other common spiders. Hence, the ease of manupulation and the quality of the samples are optimal. Both spiders are shown in figure 2.1.

Nephilas *Nephila Madagascariensis* mainly inhabits the island of Madagascar but can also be found in certain parts of southern Africa. *Nephila Edulis* (in latin, the edible golden silk spider) is commonly found in the tropical regions of Australia, New Guinea and New Caledonia. Both weave webs up to 2 m in diameter. Female nephilas are much larger than mature males, reaching 10–12 cm in length when fully grown. Males are about one-sixth of this size. The dorsal side of the female abdomen has bright yellow markings surrounded by a light gray border. The rest of the body and legs are black with patches

Figure 2.1 – Left: *Larinioides Sclopetarius*, the bridge spider, on its web during a spider hunting session at dusk. Right: *Araneus Diadematus* waiting for its prey on a beautiful 70 cm web. Observed in my home town (Bons-en-chablais, Haute-Savoie, France).

of brown. Females live for roughly one year, while males tend to live for close to six months. Only females construct webs. Although some species of orb weavers build a new web each day, *Nephila Madagascariensis* maintains its original one, simply making repairs where necessary. Once the web is stable, the spider will not stray far from it. Overall, golden orb spiders are rather docile, seldom exhibiting aggressive behavior. They pose no threat to humans, and their venom is potent enough only to insects. Any bite typically results in a small redness that would vanish within a few days, much like a bee sting. However, the spider does not bite until attacked. When trying to make it climb on one's hand, the spider simply thinks a tree branch have come by, and quickly readapt to its new environment. They are thus easy and safe to handle.

Figure 2.2 – Me, my *Nephila Madagascariensis* and I. The handling of this exotic spider is easy and safe. A bite, although unlikely, would simply result in a temporary redness.

All the presented spiders are orb-weaving spiders, characterized by the simple geometry of their webs. I had the chance to breed spiderlings. They usually come by the hundreds, crawling together out of the cocoon. During several weeks, they share food and shelter, see figure 2.3. But only a few survive. If food does not come in sufficient supply, hunger takes over companionship, turning the spiderlings into cannibales. As only a few were needed, the majority was sent back to the Oxford silk group, which

enjoys a large facility for spider care. Some were also given to the museum of the "Jardin des Plantes". Only a couple were kept in situ.
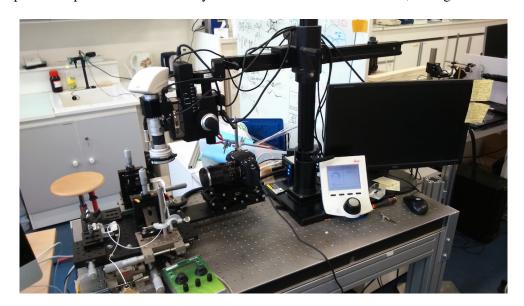
Figure 2.3 – Spiderlings sharing housing (left) and social eating (right). After a few weeks, the spider teenagers will become reclusive and will begin to defend their own living space.

2.2.2   Materials and methods part I

Here we present the materials and methods used to study spider capture silk. The experimental setup consists of a computer for sub-µN force and image acquisition as well as video recording, polarized fibre optics and regular backlighting. The sub-µN force sensor is mounted on a micro-step motor. All the setup is on a optical table for stability and to avoid undesired vibrations, see figure 2.4.
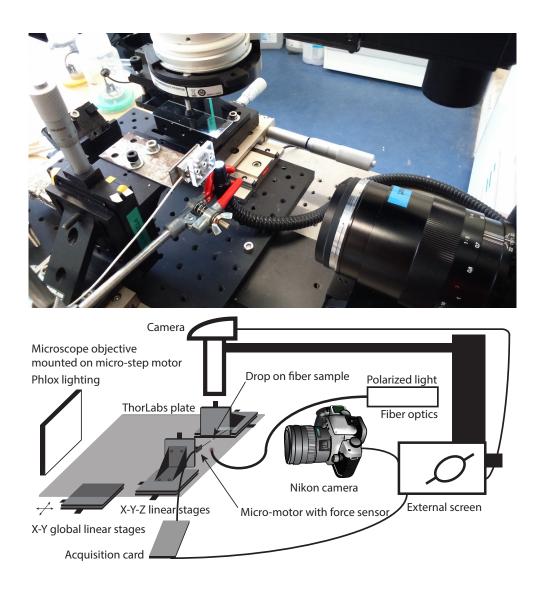
Figure 2.4 – The experimental setup used for all measurement on spider capture silk, mainly force-displacement characterization and image acquisition in different configurations.

Capture silk samples Our *Nephila* spider was kept in a 80×80×30 cm vivarium, consisting of wooden panels, PMMA windows and artificial plants (see figure 2.5). Without the latter, the spider did not feel 'at home' and did not weave any web. It serves for the comfort of the spider and above all for landmarks. The spider was kept at high humidity (above 70%) and comfortable temperature (above 22°C) with a 12/12 hours day/night schedule. The spider was fed crickets and flies two times a week. To avoid laziness and improve sample freshness, the web was partially torn down once a week, so that the spider would build it again. To help visualisation of the fibre running through each droplet, the humidity was set to 100% rH for 15 minutes before observation by use of a mistifier (see section 2.2.2). The humidity was then stepped down to 50% rH (room humidity) for observation.

Manipulation and confinement The capture silk samples were taken gently out of the web by sandwiching the desired piece of web between the bottom and a deep lid of a plastic box, and excised using a soldering iron to avoid sticking. By clicking the two together, a solid frame was obtained and used

Figure 2.5 – Spider housing. It is $80 \times 80 \times 30$ cm and consists of PMMA windows, wooden panels, artificial plants and warming lamps.

for storing fresh web samples. The center of the lid has been cut off beforehand, for easy access. To keep the samples protected, the box was completely covered with a Petri dish. A single capture thread is then transferred to a caliper. This is done by gently touching the choosen sample and cutting the outer edges with an iron solder. Loctite® is then used on both ends for effective clamping. Silk samples are best visualized under high humidity. This is because the glycoprotein content of the droplets (see section 1.3.1) blurs the liquid. We use a megasonic transducer from Beijing Ultrasonics at 1.6 MHz to produce a cloud of micronic droplets, see figure 2.6. It uses the Faraday instability of the liquid-air interface and further atomization. The Faraday instability occurs when a surface is vibrated above a certain threshold, and results in a patterning of the interface. At high intensity, the deformation of the interface becomes non-linear, and pinching occurs, ejecting micronic droplets. We use these droplets to effectively counteract the effects of evaporation (see section 3.3.1).
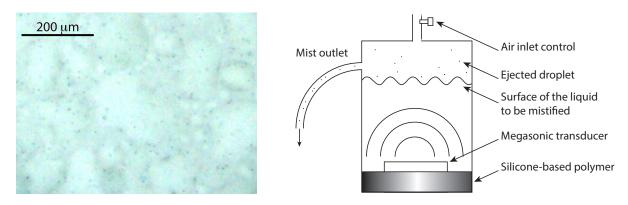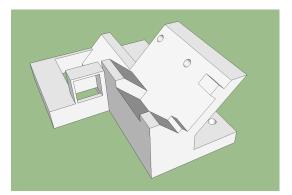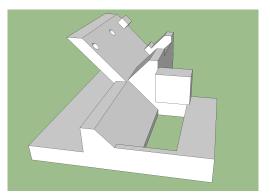
Figure 2.6 – Experimental setup used to produce micronic droplets.

The produced droplets are $3\,\mu m$ to $5\,\mu m$ in diametre and their concentration is 10^4–$10^5 mm^{-3}$. They efficiently attach to and coalesce on the fibre or on already present droplets. In order to control the environment further, a confinement chamber was built. To meet specific requirements (fit to the caliper, small chamber size, mist entry,...), the chamber was designed on the 3D modeling software Google Sketchup® before being 3D printed on a home-made fused filament fabrication 3D printer from MakerBot. The result is shown in figure 2.7.
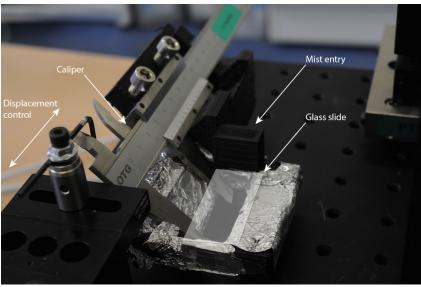
Figure 2.7 – Google Sketchup® model (top) for the 3D-printed confinement chamber (bottom). The chamber is used to create a controlled environment at 100% relative humidity and facilitate observation.

Force measurements The force sensors we used are capacitive deflection force sensors, from the Zurich-based FemtoTools® company. They are based on a unique method for measuring tiny forces (down to tens of nN, see appendix D.5) both in compression and traction. It works thanks to a calibrated series of capacitors, coupled with a tip made of a mono-crystal of silicon. When the tip is stretched, so is the series of capacitors. The capacitance of the full electronic system is a function of the spacing between the plates that make up each capacitor, and varies as the inverse of this distance. Thus, a signal can easily be recorded when stretching or compression occurs. A high number of capacitance with small spacing leads to a high sensitivity, at the scale of a few tens of nN. A data acquisition system is set for direct writing in a text file. The usual sampling frequency is 20 Hz, far below the 100 kHz capability of the sensors. The sensors are mounted on a linear micro-step positioner SmarAct SLC-

1730, with a 25 mm range, controlled by an external station with direction and speed control. The actual length of the sample and position of the drop are measured optically with a large field side camera (see figure 2.4). To decrease noise measurements levels, electronic contacts were insulated from the (metallic) optical table using electrical tape or styrofoam bottom. Gluing samples onto the sensor tip does not actually work, because the liquid glue creeps into the electronic and short-circuits the whole sensor. The samples are then attached to the sensor tip by wrapping a significant length of thread (at least 5 turns are done around the tip). The attachment is then tested during a couple of cycles of medium amplitude to verify its stability. It is verified that the rest length remains the same over cycles, both with force measurements and optically. All the tests were performed in traction at a speed of $12\,\mu\mathrm{m\,s^{-1}}$. Considering the centimeter size in length of the sample, they can be considered quasi-static. Speed has been varied well below and slightly above this value, and no significant difference has been observed. Further details about the force sensing technology and the linear micro-step motor may be found in appendix D.5.

Visualization The optical setup consisted of a Leica macroscope (VZ85RC) mounted on a micro-step motor and a 3 megapixels Leica DFC-295 camera (C-mount lens 400× angular zoom, working distance 54 mm, numerical aperture 0.12) for high resolution snapshots. The theoretical picture resolution is 334 nm/pixel, without taking diffraction into account. This is discussed in details in appendix C.1. For video recording, we used a D800E Nikon camera with three 10 mm C-mount extension rings (937 nm/pixel video resolution and 374 nm/pixel photo resolution). The very high resolution is particularly useful as it is used as an accurate measurement method. The depths of field with the Leica DFC-295 camera is 2.7 mm and 80 µm at 50× and 400× angular zoom respectively. The fields of view are 6.1 mm and 780 µm at both extremes. We used a long life highly uniform $50{\times}50$ mm^2 Phlox backlight at 60 klux or alternatively an optical fibre with LED lamp (50 W Moritex MHF-M1002 at 100 klux) with circular polarizers to avoid reflections. Side views were acquired with a second D800E Nikon camera, with a 70 mm extension tube and a 100 mm macro Zeiss lense (7,27 microns/pixel video resolution). All of it mounted on an optical table for stability.

Because of the high curvature of liquid interfaces and optical index contrast, only part of the droplet's internal structure is lit. The part of the drop that is illuminated is the image of the light source as seen from the droplet's perspective. So in order to increase the viewing angle span, the light source must be taken as wide as possible and positioned close to the object. But larger light sources provide less illumination density, so a compromise was found between light source size and power according to the need. For ease of manipulation, the light sources were set at an average distance of 5 mm. Whenever more room was needed, for instance in the case of fluctuating or sagging samples, a 1 cm distance was set.

2.2.3 Observation of the windlass in spider silk samples

A sample made of a single spider capture thread was first extracted from a home-grown web, as explained in section 2.2.2. The sample was then carefully deposited on the force measurement setup and exposed to high relative humidity during 15 minutes to swell up the droplets, and reach a stable stationary state. A tensile experiment is then carried out, and the force is recorded. To avoid any viscous stress build up, the test is done quasi-statically, at a speed of $12\,\mu\mathrm{m\,s^{-1}}$.. A video camera is mounted on the microscope objective and synchronized with the force measurements, simply by starting the two at the same time. The results are shown in figure 2.8.

This experiment shows a strong link between geometry and force. Region III is linked to droplet
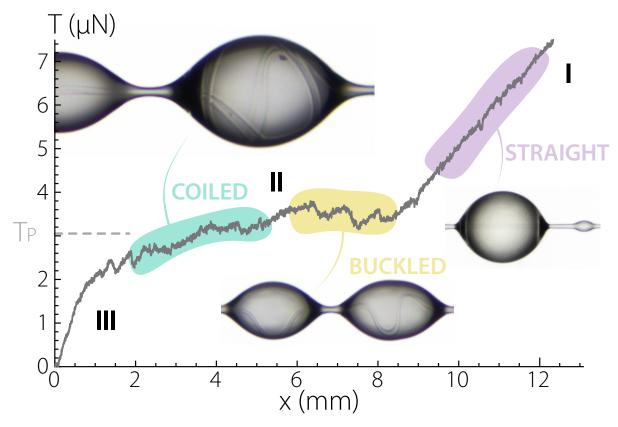
Figure 2.8 – Force measurements on spider capture silk and thread local geometry. This proves a strong correlation between the shape of the in-drop thread and the mechanical response.

stretching, when the external force is lower than the capillary force, and thus the part of the thread located inside the drop is still under effective compression. Then the fibre begins to uncoil, giving up all the accumulated length, and creating an effective force plateau T_P (region II). Finally, region I is linked to the core fibre mechanical response, which acts as a simple elastic spring. The measured Young's modulus of the core fibre is thus found to be 5±4 MPa, in good agreement with values reported in the literature (Omenetto and Kaplan, 2010). While the force plateau resembles the mechanical behavior of a liquid (De Gennes et al., 2004), region III resembles a purely elastic solid regime. The windlassing samples have thus the combined characteristics of liquids and solids, and may be coined liquid-solid mechanical hybrids.

The shape of the force-displacement curve is related to the typical J-shape of biomaterial (Gordon, 2003), but instead of being an exponential, it is composed of three straight lines of very different slopes. We coin the shape of the transition to the solide regime (associated with the end of the uncoiling) a V-shape curve. The close ressemblance, even if accidental, is one of the argument usually taken to involve protein unfolding (Becker et al., 2003). However, if recorded with low accuracy, the shapes resemble sufficiently to be mistaken.

It can be seen quite clearly on the insets of figure 2.8 that the capture thread is actually made of two parallel fibres running together inside the droplet. The reason of the presence of the two fibres lies in the biological concept of bilateral symmetry. Almost all silk glands within the spider abdomen come in pairs, as explained in section 1.2.1. The advantages of coiling multiple fibres will be further discussed in section 5.2. Another important parameter is the speed at which the experiment is carried. Indeed, a high tensile speed might build up viscous stresses, as well as elastic stresses, as the glue droplets are

made of a visco-elastic fluid. Visco-elasticity increases with the concentration of glycoproteins, and thus decreases with relative humidity as the drops are diluted. Performing measurements at very low speed and high humidity is thus required to obtain the proper quasi-static force-displacement characterization of spider capture silk.

2.3 Biological consequences for the mighty spider

2.3.1 Liquid-solid mechanical hybrid

It is our understanding that the windlass mechanism has been evolved to protect the structural integrity of the web. Indeed, during buffering, for instance from the wind, local compression may occur in some capture threads. In the result of compression were sagging or global buckling, these threads would adhere to each other and annihilate the stickiness of the spider web. Thus self-tension is a necessary feature for a dense and effective trap, and largely extends the lifetime of the web.

Furthermore, the existence of the windlass mechanism allows the spider to reach extreme mechanical abilities. The windlass mechanism constitutes a thread reserve in each coil, that can extend a great deal and offer very high extensibility to the whole web, on a global scale as well as on a local scale. This is linked to the auto-hunting electrostatic effect discussed in section 1.1 (Ortega and Dudley, 2013; Vollrath and Edmonds, 2013). The very high contrast of rigidity, from quasi-null to tens of MPa, is unique and highly contributes to the overall performance of the web, by offering a controlled combination of strength and extensibility. A regular network of radial threads (stiff and not extensible) and capture threads (soft and extensible) makes for an effective and resistant trap. The effective mechanical performances are described by the damping and fracture energy of the web, as explained below.

2.3.2 Additional sources of damping and fracture energy

Damping is crucial for many natural systems. For instance, damping enables trees to resist the blows of wind. Damping may be caused by the interaction of fine structures such as leaves with air, contact with other trees, root interaction with soil, and dissipation in the plant material (Spatz et al., 2007). Typically, plants achieve damping ten times more efficiently than man-made structures (De Langre, 2008). In the current literature, there are discussions as to what is the actual main source of damping of a spider web. Lin et al. (1995) proposed that aerodyamics plays a large role in web damping performance, but Aoyanagi and Okumura (2010) model web damping without taking aerodynamics into account. Sensenig et al. (2012) results may be interpreted as having the main mechanical damping in the radial threads, even though they admit to have found instances where the quasi-totality of the energy is damped in capture threads.

Though its relative importance is unclear (but acknowledged as important), the windlass mechanism provides an additional source of damping. As a reserve of length, the windlass creates the need for an increased travel length before breaking. Although the quasi-static force is small compared to forces built up in the elastic regime at high strain, the viscous stress that develops during dynamic traction may be much higher. The viscosity of the drop plays an important role here, along with the visco-elasticity of the fibre itself. The latter is the damping that occurs in the amorphous matrix of the core fibre, as explained in section 1.2.1.

Additionnally, the glycoproteins present in the capture thread droplet generate a visco-elastic behavior to the liquid coating. Visco-elasticity increases drop adhesion (see section 1.3.1), as well as fracture energy. Drop viscoelasticity is an important source of dynamic stress, especially at high impact rates.

However, this might influence the uncoiling dynamics. Our intuition is that the viscoelasticity of the droplets has been optimized to secure high damping in the very first moments of insect impact, followed by uncoiling-induced viscous damping. Optimization of viscoelasticity has already been observed for insect trapping (Dumais and Forterre, 2012; Gaume and Forterre, 2007).

Damping is also linked to dynamics of the windlass and ultimately to its efficiency, as the coiling must be faster than external buffeting. This will be quantified in section 4.7, after a detailed analysis of the windlass mechanism.

UNIVERSALITY OF THE WINDLASS – THEORY, SIMULATIONS AND EXPERIMENTS

"Everything is theoretically impossible, until it is done." — *Robert A. Heinlein*

Contents

T HIS chapter aims at forming a simple model for the windlass mechanism. The first section is dedicated to bringing forward the conceptual background of the mechanics of the windlass system. The second section is dedicated to the corresponding numerical simulations. The third section provides experimental proofs of the feasibility of drop-on-coilable-fibre systems.

3.1 Theory of the windlass mechanism

The first details of the windlass mechanism were introduced in section 1.4. Here we push the theory further, first by showing that the windlass is analogous to a phase transition. Then we describe the nature of this transition, and show signs of subcriticality.

3.1.1 Analogy with phase transition

A phase transition is the transformation of a thermodynamic system from one phase of matter to another, by transfer of energy. The classic example of a phase transition is boiling water, transforming liquid water into gaseous water by means of heating. When the water is either in a completely liquid state or completely gaseous state, the supplied energy is converted into a temperature increase. But during phase transition, the temperature is constant and all the supplied energy is consumed in the transformation from liquid to gaseous water. The windlass mechanism may be seen as a mechanical phase transition between a coiled wet phase and a straight dry phase, with the applied tensile work being analogous to the supplied heat, the recorded force to temperature and the strain to the specific volume, i.e. the inverse of the density. The analogy is shown in figure 3.1.
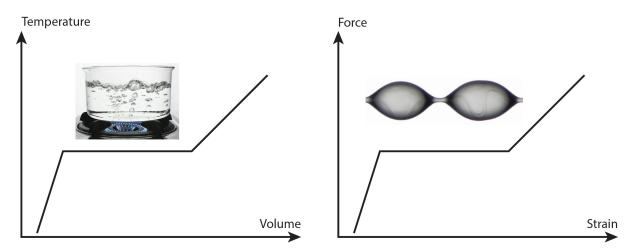
Figure 3.1 – The windlass mechanism can be seen as a mechanical phase transition, analogous to the daily life experience of water boiling.

The analogy of the windlass mechanism to a phase transition is justified by the fact that it is possible to transfer wetting energy into bending energy, as seen in section 1.4.4, analogous to the transfer of heat into latent heat in boiling water.

To elucidate the conditions for the windlass action, we examine this transition further. We start by considering a model capture thread composed of a soft fibre, that can be bent or stretched and subjected to an external tension T, and supporting a wetting liquid drop standing astride (Lorenceau et al., 2006). Though thin, silk fibres are not expected to be significantly excited with thermal fluctuations: the persistence length of such fibres is indeed estimated to be kilometer-sized, to be compared with a few tens of nanometers for DNA (Marko and Cocco, 2003). Disregarding entropic elasticity effects, we describe the windlass activation as a transition between a coiled phase – where the fibre is entirely packed within the liquid drop – and an extended phase – where the fibre runs straight through the drop. The extended phase is modelled as a spring with stiffness $k_e = \pi E r^2 / L$, where L stands for the rest length, E the Young's modulus of the fibre and r its radius. The strain energy of the extended phase is then $\frac{1}{2} k_e (x_e - L)^2$, where x_e is the phase's extension. The coiled phase typically describes the system at low applied tension T. In the limit $T = 0$ the coiled phase extension is $x_c = D$ where $D = 2R$ is the diameter of the, then spherical, liquid drop. As tension starts rising, the liquid drop deforms into an elongated shape. Modelling the deformation as ellipsoidal yields the following spring-like relation: $T = \frac{4}{5} \pi \gamma (x_c - D)$, where γ is the liquid surface tension. The strain energy of the coiled phase is then $\mathscr{E}_c = \frac{1}{2} k_c (x_c - D)^2$ where the spring stiffness of the liquid drop directly arises from surface tension $k_c = \frac{4}{5} \pi \gamma$.

As typical for phase transition problems, there is an energetical cost per unit length associated with the transformation from the coiled phase to the extended phase, which we note ϵ_0. This energy originates from both the uncoiling of the fibre and the energy difference between wet and dry states. The uncoiling process results in an elastic energy gain $-\frac{1}{2} E I \kappa^2$ per unit length, where the curvature $\kappa = 2/D$ and $I = \frac{\pi}{4} r^4$ for a circular fibre of radius r. The latent energy per unit length also embodies the difference in surface energies: in the coiled phase the fibre is surrounded by liquid, hence bears a surface energy $2\pi r \gamma_{sl}$ per unit length whereas in the extended phase the air surrounding the fibre yields an energy $2\pi r \gamma_{sv}$ per unit length. Here γ_{sl} and γ_{sv} denote solid-liquid and solid-air interface energies respectively. Upon using Young-Dupré wetting relation $\gamma_{sv} - \gamma_{sl} = \gamma \cos \theta_Y$, the energetical cost for phase transformation is obtained: $\epsilon_0 = 2\pi r \gamma \cos \theta_Y - \frac{1}{2} \pi E r^4 / D^2$, where θ_Y is the liquid contact angle on the fibre. Noting $\mathscr{E}_e$ the total energy of the extended phase, with $\mathscr{E}_e = \frac{1}{2} k_e (x_e - L)^2 + \epsilon_0 L$, we now write the global energy when part of the fibre is in the coiled phase, and part in the extended phase. Assuming an imposed total
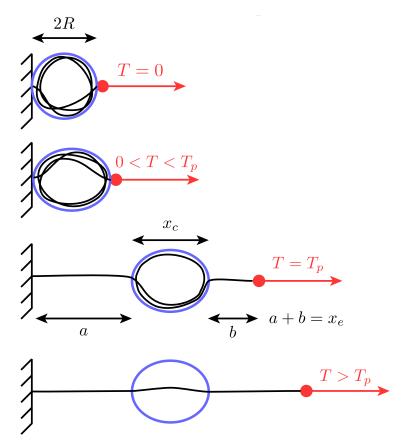
Figure 3.2 – Two phases model. The windlass system comprises two phases. The extended phase consists of the fibre that lies outside the drop(s). The coiled phase consists of the fibre that is coiled inside the drop(s). Each phase has its own extension, and there is a fraction ρ (resp. $1 - \rho$) of the complete fibre in the extended (resp. coiled) phase.

extension x and denoting the extended phase fraction ρ, the global energy $\mathscr{E}$ reads:

$$\mathscr{E}(x_e, x_c, \rho) = (1 - \rho)\mathscr{E}_c(x_c) + \rho\mathscr{E}_e(x_e). \tag{3.1}$$

Minimizing this energy under the constraint $x = (1-\rho)x_c + \rho x_e$ we find that the fibre can be entirely in the coiled phase ($\rho = 0$, fibre fully packed in the drop) with tension $T = k_c(x - D)$, or entirely in the extended phase ($\rho = 1$) with tension $T = k_e(x - L)$. A third interesting possibility consists in a mixture of phases $0 < \rho < 1$. In this latter case, part of the fibre is packed in the drop but the outer part is taut, consistent with our observations. In the limit where $2R \ll L$ and $\epsilon_0 \ll k_e, k_c$, we have $x_c \simeq D + \epsilon_0/k_c$, $x_e \simeq L + \epsilon_0/k_e$ and $T \simeq T_P \simeq \epsilon_0$, so that the plateau tension is given by

$$T_P \simeq 2\pi r\gamma \cos\theta_Y - \frac{1}{2}\pi E\frac{r^4}{D^2} \tag{3.2}$$

Numerical simulations are presented in section 3.2, and experiments in section 3.3.2. Both show very good agreement with the phase transition model. Both also reproduce the fine details of the windlass mechanism, for instance the very nature of the coiling transition, which is discussed below.

3.1.2 A subcritical transition

Many natural and engineering systems exhibit transition from one state to another. Some of the prominent examples of transition are water to vapor, paramagnetic to ferromagnetic, conduction to convection

(e.g., in Rayleigh Bénard convection), laminar to turbulent flow in channels, etc. Some of these transitions are continuous, i.e. the order parameter grows smoothly from zero as the control parameter is increased through the transition, while some others exhibit a discontinuity or a finite jump in the order parameter. The former class of transitions is called supercritical, while the latter is called subcritical (Verma and Yadav, 2013).

Figure 3.3 – Supercritical transition (left) and subcritical transition (right). In the latter, a discontinuity of the measured parameter X exists during continuous increase of the control parameter C. Solid lines represent stable equilibria, whereas dashed lines are unstable.

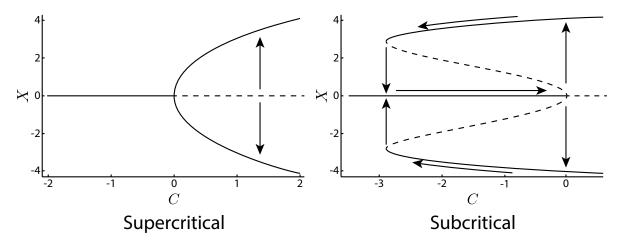The paths depicted on figure 3.3 show that the behavior of a system through a transition depends on the nature of the latter. In contrast to the smooth and reversible supercritical transition, the subcritical transtion is rather violent at the threshold, and exhibits two different barriers. The barrier to deactivate the transition (leftward arrow on figure 3.3) is lower than the barrier to activate it (rightward arrow). That means that for a range of control parameter C, there are two possible solutions. One must specify the previous history of the system in order to distinguish between the two. This history dependency is called hysteresis, and is related to damping properties. An interesting example of subcritical transition is found in the buckling of thin metal shells (Timoshenko, 1983). In careful laboratory tests, researchers had found thin metal shells to be collapsing violently at about one quarter of the classical buckling loads predicted by small-deflection linear theory. Furthermore, the experimental results were very scattered, well above the measurement errors. This was eventually explained by the existence of a very unstable, subcritical post-buckling path in the shell equilibrium diagram. This leads to metastable states of the shell, and a high sensitivity to defects and lateral shocks. The explanation of this discrepancy has been very useful in designing aircraft cabins with proper factors of safety (Thompson, 2014).

The subcritical nature of the windlass mechanism comes from the specific mechanics of the elasto-capillary buckling phenomenon. The transition between the stretching and the capillary coiling regimes occur when the tension is such that the part of the fibre that lies inside the drop experiences compression above the Euler local buckling threshold. The post-buckling regime begins with an out-of-axis deformation of the in-drop fibre and a sliding of the meniscii to accomodate the drop diameter back to equilibrium. This increases the fibre wetted length over which buckling occurs. As the buckling threshold depends upon the arc length ℓ between the boundary points as $\propto \frac{1}{\ell^2}$, this implies a softening of the system and a negative stiffness regime.

As a consequence, the recorded tension is expected to shoot back upwards, as the counteracting resistance to bending suddenly decreases, as sketched in figure 3.5. The tension then stabilizes on a plateau, described by the force required to hold the system in the post-buckled state, which is five times smaller
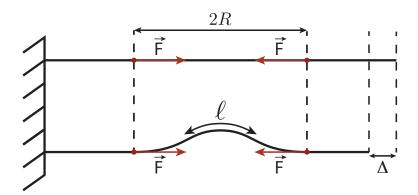
Figure 3.4 – The subcritical nature of the windlass mechanism comes from the specific mechanics of the elasto-capillary buckling phenomenon. The drop retains its size, while swallowing additional fibre length. The length over which buckling occurs increases from $2R$ to $\ell = 2R + \Delta$, which decreases the encountered resistance.

than the buckling threshold force.
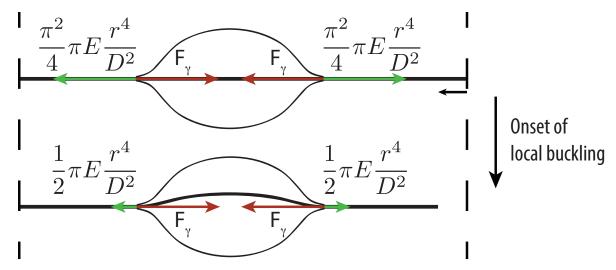
Figure 3.5 – The drop-on-fibre system exhibits a force undershoot at the coiling activation. This is due to the drastic decrease of the fibre resistance to bending after buckling. When the fibre is straight, its resistance is $\frac{\pi^2}{2} \approx 5$ times higher than when the fibre is buckled. The red arrows represent the capillary force (compressive), and the green arrows are the resistance to bending of the fibre.

Consequently, windlass can hold in drops with radii smaller than the activation radius. Windlass will be deactivated if the drop radius becomes smaller than the so-called deactivation radius R_{deac}, which, from equation (1.4), is found to be

$$\text{Deactivation if } R < R_{\text{deac}} = \frac{R_{\text{ac}}}{\sqrt{\pi^2/2}} = \sqrt{\frac{Er^3}{16\gamma \cos \theta_Y}} \tag{3.3}$$

The existence and consequences of this deactivation radius are shown experimentally and discussed in section 4.3. There is a simple picture to understand the subcritical nature of the windlass transition. If $\epsilon_0 < 0$, then we have a normal drop-on-fibre system. If $\epsilon_0 > 0$, the system gains energy when some fibre is coiled in, theoretically "swallowing" suddenly all available fibre. The discontinuity of the transition at $\epsilon_0 = 0$ is another sign of subcriticality. Of course in practice there is a limit to the amount of fibre

that can be coiled in. But in a large majority of tests, this limit could not be reached, see discussion in section 4.4.

3.2 Numerical simulations of the windlass

We performed detailed numerical computations of the equilibrium of a flexible elastic beam under localised large deformations following methods developed in our recent literature (Audoly and Pomeau, 2010; Antkowiak et al., 2011; Elettro et al., 2015). The generalization to 3D is not a difficulty in itself, but for clarity of the explanation, the following discussion is restricted to a 2D model.

The beam, held at both extremities with imposed distance $x = L - \Delta$, is modeled as an elastic beam obeying Kirchhoff equilibrium equations (developed below), and is subjected to attracting meniscus forces F_γ at entrance and exit (points A and B) of a confining disk and under the action of a tensile end-load. The presence of the liquid disk generates these capillary forces due to the contrast of surface energy, the interaction energy of the beam with the liquid being smaller than the interaction energy of the beam with the air. As shown in the publications presented in appendix F, meniscii forces Λ_A and Λ_B are pointing towards the center C of the disk. Their intensity is related to surface tension γ_{lv}, but also to the angle between their direction and the tangent to the beam at the meniscus points. Λ_A and Λ_B represent force jumps at the meniscii, but it is to be noted that the total external force applied on the beam by the disk is zero.
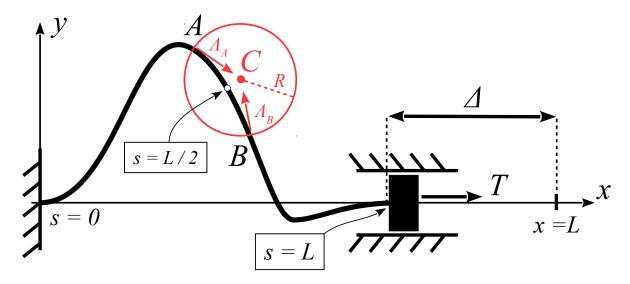
Figure 3.6 – An elastic beam held in tension at its extremities, and buckling under the action of compressive forces in a disk. The beam is clamped at both ends. The deformation of the beam is described by the angle $\theta(S)$ between the tangent to the beam and the x-axis, where $S \in [0, L]$ is the arc-length along the beam.

The beam has a length L and a circular cross-section of radius r. We work under the slender ($L \gg r$) Euler-Bernoulli hypotheses where the beam is considered inextensible and unshearable. Configurations are thus fully described by the position and orientation of the centerline. We use the arc-length $S \in [0, L]$ and note $\theta(S)$ the angle between the tangent of the beam and the horizontal.

Capillary forces are two-fold: (i) meniscus forces as described, but also (ii) barrier forces that prevent the beam from exiting the disk elsewhere than at the meniscus points. A soft-wall barrier potential

(Manning and Bulman, 2005)

$$V(X,Y) = \frac{V_0}{1 + \rho - \frac{1}{R}\sqrt{(X - X_C)^2 + (Y - Y_C)^2}} \tag{3.4}$$

is used to retain the beam inside the disk, centered on (X_C, Y_C) and of radius R. The small dimensionless parameter ρ is introduced to avoid the potential to diverge at the meniscus points, where the beam enters and exits the disk. The intensity V_0 of the potential is chosen to be small, the hard-wall limit being $V_0 \to 0$.

Kinematics, relating the position (X, Y) of the beam and the inclination θ of its tangent $(\cos\theta, \sin\theta)$ with the horizontal, the bending constitutive relation, relating the curvature $\theta'(S)$ (with S the curvilinear abscissa along the beam) to the moment $M(S)$, and finally force $(N_x(S), N_y(S))$ and moment balances are derived from an energy minimization perspective.

We consider the drop to be undeformable and thus remains a disk throughout the experiments. The interface energy between the liquid drop and the air (related to γ_{lv}) is thus a constant. The internal energy of the system comprises the bending energy E_b of the beam, the barrier energy E_w of the circle, and surface energy E_γ:

$$E_\kappa = \frac{1}{2}EI\int_0^{S_A}\kappa_1^2\,dS + \frac{1}{2}EI\int_{S_A}^{S_B}\kappa_2^2\,dS + \frac{1}{2}EI\int_{S_B}^{L}\kappa_3^2\,dS \tag{3.5a}$$

$$E_w = \int_{S_A}^{S_B} V(X(S), Y(S), X_C, Y_C)\,dS \tag{3.5b}$$

$$E_\gamma = P\,\gamma_{\mathrm{sv}}\,S_A + P\,\gamma_{\mathrm{sl}}\,(S_B - S_A) + P\,\gamma_{\mathrm{sv}}\,(L - S_B) \tag{3.5c}$$

where $P = 2\pi r$ is the perimeter of the cross-section of the beam, and V_0 has the dimension of an energy per unit length. The curvatures $\kappa_i(S)$ are defined in each region of the beam. We add the work done by the external load $T\,e_x$ and obtain the potential energy of the system:

$$E_\kappa + E_w + E_\gamma - T\,X(L) \tag{3.6}$$

We minimize this energy under the following constraints

$$\frac{S_A + S_B}{2} = \frac{L}{2} \tag{3.7a}$$

$$[X(S_A) - X_C]^2 + [Y(S_A) - Y_C]^2 = R^2 \tag{3.7b}$$

$$[X(S_B) - X_C]^2 + [Y(S_B) - Y_C]^2 = R^2 \tag{3.7c}$$

Equation (3.7a) restricts the system so that the capturing disk is centered on the mid-point of the beam. We introduce Σ such that $S_A = L/2 - \Sigma$ and $S_B = L/2 + \Sigma$. The beam has then 2Σ of its arc-length spent in the disk. As the variables $X(S)$, $Y(S)$, $\kappa(S)$ and $\theta(S)$ all appear in the formulation, we have to consider the continuous constraints relating them:

$$X'(S) = \cos\theta(S),\ Y'(S) = \sin\theta(S),\ \theta'(S) = \kappa(S) \tag{3.8}$$

where $' = \frac{d}{dS}$. We can consequently write the total Lagrangian of the system. The beam is clamped at both extremities, and yields simple boundary conditions on the position and angle of the beam at the edges $X(0) = 0, Y(0) = 0, \theta(0) = 0, Y(L) = 0, \theta(L) = 0$. We minimize this Lagrangian, that is

we compute its first variation under small perturbations of the variable. Requiring the first variation to vanish, we obtain:

$$X'(S) = \cos\theta \tag{3.9a}$$

$$Y'(S) = \sin\theta \tag{3.9b}$$

$$EI\theta'(S) = M \tag{3.9c}$$

$$M'(S) = N_x \sin\theta - N_y \cos\theta \tag{3.9d}$$

$$N'_x(S) = \chi \frac{\partial V}{\partial X} + \delta(S - S_A)\Lambda_A \frac{X_A - X_C}{R} + \delta(S - S_B)\Lambda_B \frac{X_B - X_C}{R} \tag{3.9e}$$

$$N'_y(S) = \chi \frac{\partial V}{\partial Y} + \delta(S - S_A)\Lambda_A \frac{Y_A - Y_C}{R} + \delta(S - S_B)\Lambda_B \frac{Y_B - Y_C}{R} \tag{3.9f}$$

with $\chi = 1$ for $S \in [S_A; S_B]$ and $\chi = 0$ otherwise, and where $\delta(S - S_\star)$ is the Dirac distribution centered on $S = S_\star$ and $X_{A,B} = X(\frac{L}{2} \pm \Sigma)$ and $Y_{A,B} = Y(\frac{L}{2} \pm \Sigma)$. The beam material has Young's modulus E and the second moment of area of the beam's section is $I = \pi \frac{r^4}{4}$.

This system of equations is highly non-linear. It is possible to linearize it to the first order and find weakly non linear solutions that represent the system close to the buckling threshold. This is used to obtain equation (4.2) which gives an analytical approximation of the subcritical buckling threshold.

However, the far-from-threshold behavior must take into account the full non linearities of the system. Sources of non linearity are the large rotation of the beam, and also the complex force field that the beam encounters. The generalization to 3D differs from the 2D model only by the existence of torsional terms, which add to the complexity of the problem. The concepts remain the same.

The equilibrium of the full system is solved using two-points boundary-value problem techniques. As such, we implement a continuation of equilibria using a shooting method in Mathematica. The shooting method consists in exchanging the boundary conditions in $S = L$ with initial conditions at $S = 0$, which means working with $\theta(0)$ and $\theta'(0)$ instead of $\theta(0)$ and $\theta(L)$. More precisely there is a value of $\theta'(0)$ that generates a solution that fulfills the boundary condition $\theta(L) = 0$. This value is computed using a classical Newton-Raphson scheme. This allows for reduction of the boundary-value problem to the solution of an initial-value problem.

For large $f_\gamma = \frac{F_\gamma}{EI/D^2}$ values, typically $f_\gamma > 15$, numerical difficulties arise and we thankfully switch to the Fortran - AUTO package which uses a collocation method. The collocation method consists in choosing a finite-dimensional space of candidate solutions (usually, polynomials up to a certain degree or sine functions) and a number of points in the domain (called collocation points), and to select the solution which satisfies the given equation at the collocation points. For further details, see the publications in appendix F. This yields the 3D configuration of the beam, as shown in figure 3.7.
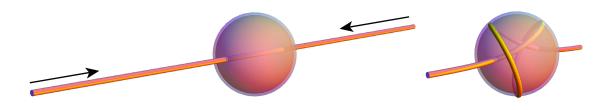
Figure 3.7 – Numerical simulations of the coiling of a beam inside a spherical cavity.

Figure 3.7 reveals the localisation of the curvature within the drop during beam compression, reminiscent of the observations of spider capture silk samples. The knotted structure of the beam is due to the lack of implementation of self-contact. Further numerical characterisation of the drop-on-fibre system includes a force-displacement diagram, combined with snapshots of the coiling geometry calculated. It unravels a buckling transition where the slack beam is suddenly localised within the droplet. Continuation of equilibria, with $F_\gamma D^2/EI = 20$ and $L = 20\,D$, reveals the fine details in the micromechanical response on figure 3.8, resulting in inhomogeneities of the plateau. These fine details are related to sudden increase in the coiling rate, as we show in section 4.3.2. The approximate plateau value $T_{\mathrm{P}} D^2/EI \simeq 18$, given by equation (3.2), is drawn for comparison. Several equilibrium configurations illustrate the coiling of the beam and its strong packing within the droplet.
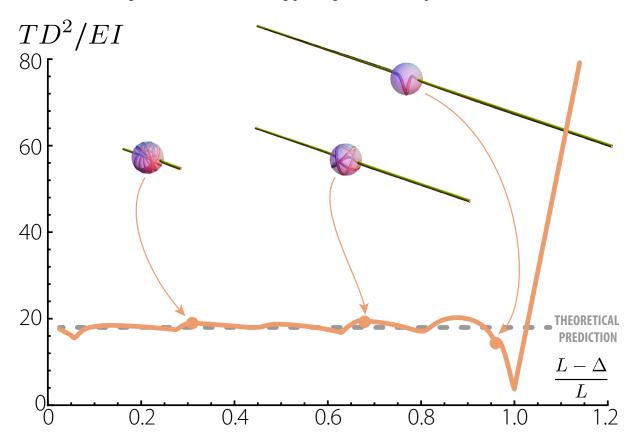
Figure 3.8 – Windlass mechanism can be seen as a structural phase transition.

Figure 3.8 clearly shows the onset of liquid-like behavior under compression, switching from a linear spring regime to a force plateau – equivalent to a vanishing rigidity – at $x = L$. This mechanical response is typical of systems exhibiting first-order phase transitions. This confirms numerically the analytical model involving a coiled wet phase and a stretched dry phase that was developed in section 3.1.1.

The subcritical nature of the coiling transition is visible in figure 3.8 as a retightening of the system at $x = L$, indicated by a sudden force increase. This negative rigidity regime will be observed experimentally and discussed further in section 4.3.2.

Universality of the windlass mechanism   The idea behind the windlass mechanism is that the seemingly simple ingredients of fibre elasticity and drop capillarity can have dramatic consequences on the coupled equilibrium of the system. These ingredients being universal, there is no need for complex

biochemistry to explain spider silk uses, as highlighted in section 2.2. This means that the concept is inherently mechanical, and may thus be expanded theoretically to any material. In the next section, we show experimentally that the windlass mechanism used by spiders is reproducible with virtually any materials.

3.3   Reproducing the natural windlass

In this section we present an experimentaly simple way of producing a completely artifical windlass mechanism. It has been shown in section 3.2 that, in theory, any material may be used as a coiling system. Here we make an experimental proof of this.

3.3.1   Materials and methods part II

Choice of the material

The specific functionalization process of combining the right fibre to the right droplet ("right" being defined by size arguments given in equation (1.6)) is protected by the international patent number FR1453960, as of april, 30th 2014.

As universality was highlighted previously, one may think that any material would be equally suitable for experiments. But it is not. In practice, common materials like wood or glass have such a high Young's modulus (on the order of GPa), that the fibres needed would have a sub-micronic diameter. Such fibres are tricky to produce and require heavy, expensive and constraining equipment to observe and characterise (Atomic Force Microscope, Scanning/Transmission Electron Miscroscope,...). As a matter of ease of manipulation, we focused on finding a soft material, so that the critical fibre diameter is higher (see equation (1.6)), which makes the fibres less difficult to manipulate. There exists extremely soft materials, but they usually require slow and/or partial curing, which makes them difficult to be produced at the required scales, which is still at the order of 100 μm. The challenge was in fact to find a material and an feasible process that matched the necessary conditions, mainly a compromise between softness and ease of production. The problem has been tackled by the polymer industry and the class of material of choice is called thermoplastic polymers, and is particularly adapted to injection molding techniques. Thermoplastics differ from thermosetting polymers (like vulcanized rubber for car tyres), which form irreversible chemical bonds during the curing process. This is due to the nature of the crosslinks, i.e. the joints between the polymer chains (see figure 3.9).

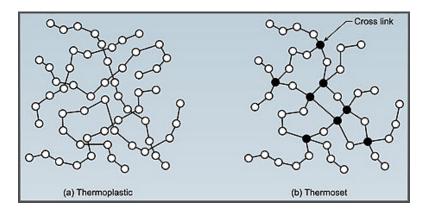
Figure 3.9 – The difference between thermoplastics and thermosets holds in the irreversible cross-linking of the later. Source: RecycledPlastic.com.

We contacted Denis Bouvier from BASF®. He kindly sent us a 1 kg sample of Soft Thermoplastic

PolyUrethan (TPU, product name Elastollan 1185A). The datasheet value of the Young's modulus of the TPU is 20.5 MPa, the softest we could find. This value have been verified in situ after fibre production, to be sure that there are no effect of size or processing speed on the fibre rigidity. Further details may be found in appendix D.1. We will see in the next section how the raw material is processed in order to produce fibres of necessarily micronic sizes. We also used different kind of material to induce windlass, such as glass, electropinned polymeric fibres or glass transition-activated PolyLactic Acid. For further details, see chapter 5.

Fibre drawing

Melt-spinning The Soft Thermoplastic PolyUtherane (TPU) we worked with was most often melt-spinned. This process consists of melting down a material, then pick a small quantity of liquid, apply an extensional flow (stretch it) and quench it into the final form, as shown on figure 3.10.
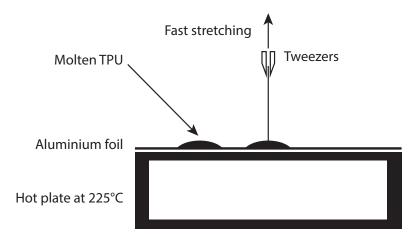
Figure 3.10 – Sketch of the melt spinning technique. TPU granules are melted at 225°C on a hot plate covered with aluminium foil. A small amount of liquid TPU is then pinched with tweezers, and violently stretched while released in open air to quench.

For better melt properties, TPU is stored in dry atmosphere (P_2O_5) to avoid contaminating water content. TPU has a melting point around 160°C. TPU granules were placed on a hot plate covered with an aluminium foil (to avoid stains) at 225°C for proper fluidity of the material. After melting, we used a tweezer to pick up a small amount of liquid TPU which was then stretched quickly while at the same time being released at ambient room temperature. This resulted in the creation of micron-sized, metre-long, soft fibres. The fibre was then transferred to a caliper. Loctite® superglue was used to ensure good clamping conditions at both ends. The processing temperature was chosen in order to avoid mainly two instabilites, the curling instability and frozen Rayleigh-Plateau instability, both depicted in figure 3.11. As the TPU we used is amorphous at room temperature, the quenching speed and processing temperature do not have any effect on the Young's modulus of the final fibre. This was verified with in situ force measurements of the samples using the FemtoTools sensors described in section 2.2.2. We found a Young's modulus of 19±3 MPa, in good agreement with the value given by the manufacturer.

The curling instability creates a natural curvature in the fibre. In our understanding, a processing temperature too low would mean fracturing the spinned sample. Fracture and plastic events generate some excess edge energy leading a fibre with an instrinsic curvature (Shenoy et al., 2010). Although this could be used to enhance the windlass coiling, we restricted to systems with zero intrinsic curvature

Figure 3.11 – Two mechanical instabilities to be avoided when producing micronic fibres by melt-spinning. Left: the curling instability. Right: the frozen Rayleigh-Plateau instability. Note the different scales of the two pictures.

for quantitative comparison with the theory. The Rayleigh-Plateau instability has been introduced in section 1.4.3. It relies o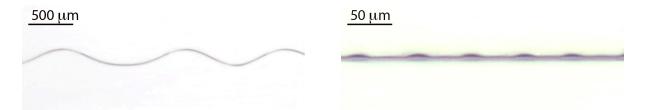n the existence of surface tension, so that a liquid cylinder which aspect ratio is larger than π is unstable (Laplace, 1805) and destabilizes on a viscocapillary timescale of $t_{\text{visc}} = \frac{\eta R_0}{\gamma}$ (De Gennes et al., 2004) for a viscous liquid polymer, with R_0 the initial radius of the liquid cylinder. If the quenching is much faster than the destabilization, then the final fibre will be smooth. The final fibres have a low radius fluctuation, on the order of 10% for 100 radius (see appendix C.2). These fluctuations are hidden within the measurement errors in most cases.

Wet-spinning Another way to produce micronic soft fibres is to use a wet-spinning method (Collier, 1970). This technique consists in dissolving the material of choice in a well chosen solvent. A droplet is then produced from the mixture, and is stretched while driven in an extraction bath. When the liquid filament enters the extraction bath, the solvent is drawn away and the material begins to solidify to its final form. Here we use liquid TetraHydroFurane (THF) to dissolve the material PolyUrethane (TPU), at a concentration of 10 wt% (weight per cent). To do so, a 5 mL bottle is left overnight with a magnetic stirrer. The resulting solution is optically clear, sign of its quality. The mixture is then placed in a syringe with syringe pump to allow control of the droplet volume. We use a needle with a right angle for ease of manipulation. The tip of the needle is placed in a water bath. THF is very soluble in water while TPU is not, so that the initial TPU is restored. The process is summed up in figure 3.12.
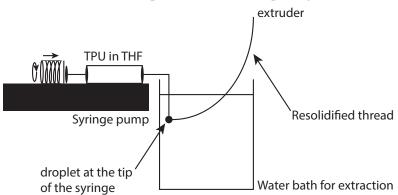
Figure 3.12 – Sketch of a droplet-spinning setup, implemented in collaboration with David Grosso (LCMCP, Collège de France).

The rate of solvent (THF) extraction in the case of wet-spinning is similar to the rate of quenching in melt-spinning process. Here the liquid filament might break into droplets if the THF/water interface surface tension is too high. But in wet-spinning, this can be reduced by use of a surfactant (commercial soap). Additionnally, the size of the nozzle as well as the initial concentration of the TPU solution influence greatly the final size of the fibre. This results in smoother fibres than with melt-spinning. But

as THF is highly dangerous and requires measures of precaution, the melt-spinning method is preferred.

Droplet choice and deposition

Choosing and depositing the proper necessary droplet on a micronic fibre is not an easy task. TPU is a low surface energy solid with $35 \, \mathrm{mJ \, m^{-2}}$ (Vargo et al., 1991), to be compared with that of silicon crystals at $1000 \, \mathrm{mJ \, m^{-2}}$ (Bikerman, 1965). Hence the liquid must have a low surface energy too for good wetting properties. A non-wetting liquid would stretch the fibre inside the drop instead of compressing it, making the windlass mechanism impossible in that case. Furthermore, a substantial volume of liquid needs to be deposited in order to obtain an axisymmetric droplet (Carroll, 1986) (see appendix B) large enough to induce local buckling,. This is taken further in the following paragraphs.

Bath extraction The simplest way to coat a fibre is to soak it into a liquid and draw the fibre out of the bath. This may result in a liquid cylinder coating the fibre, further destabilizing in an array of droplets through the Rayleigh-Plateau instability, see section 1.4.3. The thickness of the initial liquid coating is related to the speed of withdrawing, by the classical Landau-Levitch-Derjaguin relation (Landau and Levich, 1942). The final film thickness scales as $h_0 \propto \left(\frac{\eta V}{\gamma}\right)^{2/3}$, with η the fluid viscosity and V the speed at which the fibre is withdrawn. Below a speed threshold, which depends on the fluid viscosity, there is no liquid drawn with the fibre (Maleki et al., 2007). The more viscous the fluid the easier it is drawn. But the direct coating of the entire fibre may leave too much residual liquid on the edges of the sample, contaminating the experiment with drops interacting with the clamping walls and/or force sensors instead of wetting the fibre only. To circumvent this issue, we used a slightly different approach, using a droplet hanging from a needle instead of a liquid bath.

Fibre brushing with hanging droplet A localised and accurate deposition process is achieved by using a droplet hanging from a commercial chemistry needle (typically 0.7 mm in diameter). The nozzle of the needle is cut flat for better control. The micronic fibre is held in slight tension for better deposition control. Too low a tension would imply large deformation of the fibre and rebound, while too large a tension would mean fast vibration of the fibre and possible ejection of the droplets. An optimum is found at roughly 10% strain for the TPU samples, which means stresses of a few MPas, still small compared to its ultimate tensile strength. The micronic fibre is then simply brushed with the droplet as it hangs, leaving a cylindrical liquid coating on the fibre, which further destabilizes into an array of droplets. The typical size of the droplets is 20–100 μm, the spacing is 50–200 μm and the droplet array is deposited on roughly 5–10 mm. In case of overdeposition, some side droplets were removed with KimTech® wipers, a particularily smooth tissue that does not leave residues after use. The deposition process is depicted in figure 3.13.

This technique yields good results in depositing a large number of droplet of controllable sizes. To allow for reachable control and velocity range, viscous silicone oil (roughly 1000 times more viscous than water) was used. Further details about this material may be found in appendix D.3. A large viscosity lowers the speed threshold for coating. It also decreases the sensibility to inaccuracy in the applied brushing speed. This made for a very convenient way of producing desired droplets simply by hand, attaining the goal size with a 15% accuracy. Although great for viscous fluids, this technique does not work for fluids with viscosity less than 10 times that of water. An alternative technique is mistification or spraying of droplets, explained in the next section.
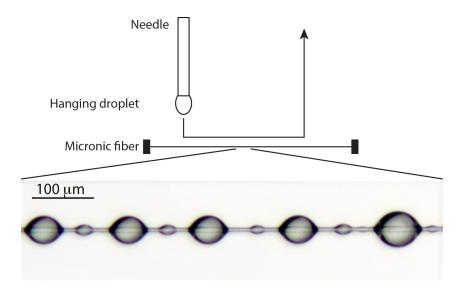
Figure 3.13 – Sketch of the droplet deposition by fibre brushing with an hanging droplet (top) and profile of droplets array (bottom) obtained by brushing a 6.1±0.3 μm diameter TPU fibre at medium speed with viscous silicone oil (1000 times the viscosity of water).

Mistification or spray   The process of "mistification", or megasonic production of mist from a desired liquid, has been explained in section 2.2.2. This works well for low viscosity fluids (below 20 times that of water) and produces droplets in the 3–5 μm range. However, if the liquid to be mistified is viscoelastic at 1.6 MHz (working frequency of the transducers), the atomization does not work (Amarouchene et al., 2001; Li, 2006). Unfortunately, this is the case of silicone oil. So if the fibre brushing technique does not work (for low viscosity silicone oils for instance), we need another solution. In order to complete our panel of droplet deposition techniques, a simple spray was used. It has been built from an empty fragrance bottle, and the resulting spraying nozzle was placed in a syringe whose bottom has been sealed. The sprayed droplets are bigger than the ones in the mist, roughly 20 μm in size. It is still small enough for the micronic fibres to capture them though, even at their incoming velocity.

Now that we are able to deposit almost any droplet of wetting liquid, comes another issue: the drop might simply vanish through evaporation.

Droplet stabilization against evaporation

Evaporation is a type of vaporization that occurs from the surface of a liquid into a gaseous phase. In contrast with boiling, which is characterised by bubbles of saturated vapor forming in the liquid phase, evaporation happens when the gaseous phase is not saturated with the evaporating substance. At non-zero temperature, a fraction of the molecules within the liquid have enough energy to escape into open air. This is compensated by the arrival of molecules from the environment to the liquid. When the relative humidity of the gaseous environment is less than 100%, it means that the net flux of molecules is towards the air. The relative humidity is defined as the ratio between the partial vapor pressure of the molecules and its equilibrium vapor pressure at saturation, called simply vapor pressure. The Clausius-Clapeyron relationship allows one to calculate explicitly the vapor pressure at a given temperature. This will determine the equilibrium of the liquid phase.

For the case of micronic droplets in open air, the amount of liquid is not sufficient to saturate the environment and reach equilibrium. The droplets might thus disappear. The first idea is to confine the drop and saturate its near environment. This is done in practice with the use of a mist of the desired

liquid, that counterbalances the evaporation flux (see section 2.2.2). A second idea would be to use liquids with very low vapor pressure, such as high viscosity silicone oil. This can be done with water charged with salts too. There exists an equilibrium concentration of salt in water, so that if the drop is more concentrated than the equilibrium value, it will become hygroscopic and suck water from the air. This is the technique used by spiders to keep their gluey droplets wet and working.

The value of the vapor pressure also gives the dynamics of the evaporation. This gives the lifetime of a micronic droplet if it is supposed to disappear, and the time to reach equilibrium if any. For a spherical droplet in infinite medium, the radius of the droplet follows the dynamic law $R^2(t) \propto 1 - \frac{t}{t_{\text{ev}}}$ (Kent, 1973). This means that there is an acceleration of the radius decrease with time. The evaporation rate thus increases until the drop finally vanishes. The confinement may have rather drastic effects. In order to show its importance, we have measured the lifetime of ethanol drops when a 6.7 μm diameter TPU fibre is placed in different environment at constant mist flow rate. The evaporation of sessile drops on surfaces with non zero contact angles has similar dynamics than drops in infinite medium (Erbil et al., 2002). To put figures on, in an open environement the maximum obtained ethanol drop is on the order of 10 μm, and the lifetime of an ethanol droplet at this size is roughly 0.5 seconds if the mist stops. In the confinement chamber introduced in section 2.2.2, the droplet can reach 400 μm, and its lifetime in case of opening is on the order of the minute. The adjustement of the mist flow rate is an additional advantage to control the size of the droplet deposited through misting. Evaporation is used in section 4.3 to prove the subcritical nature of the windlass mechanism, theorized in section 3.1.2.

In the following, we use high viscosity silicone oil. Droplets of 300 μm in diameter have been observed to last for one month without any noticeable change in radius. The advantage of using high viscosity liquids or salty water is that it does not need any confinement nor mist in order to work. This enhances the clarity of the field of view and thus the quality of the observation.

3.3.2 Realisation and characterisation of the artificial windlass

Here we present the practical realisation of a fully synthetic windlass mechanism. To do so, we used ThermoPlastic PolyUrethane (TPU) combined with silicone oil droplet. TPU and the associated process to mold it into micronic fibres is described in section 3.3.1. The Young's modulus of these fibres is 19±3 MPa, in good agreement with the value given by the producer. The fibre size required for coilability is given in equation (1.6). The dynamic viscosity of the oil was 1000 mPa s, which allows deposition of a large and stable amount of liquid. The resulting drop-on-coilable-fibre sample is compressed below the slack length of the core fibre to induce coiling. It is indeed observed for droplets large enough (as defined in equation (1.5)) as a slight retightening of the fibre and subsequent drop lift upon coiling activation. The fibre coiling is further observed under microscope, following the techniques given in section 2.2.2.

Because of the curved liquid interfaces, the droplet is able to focus incoming light and act as a lens. As a consequence, the periphery of the drop is hard to illuminate, as explained in section 2.2.2. In contrast to natural samples, micronic fibres of TPU have the capacity to polarize incoming light. This might be due to the small size of the produced fibres with respect to the size of the polyurethane molecules. This can induce alignment of these molecules in the main axis of the fibre and thus anisotropic interaction with light. We harvest the polarizing power of the fibres to change the light intensity of the fibre independently from the background. This is done by using two polarizers, one at the light source and one at the microscope lense. The sample will then receive polarized light. The light that goes through the fibre sees its polarization plane rotated, while the background polarization is unchanged. By crossing the two polarizers at right angle, one may "switch off" the background and reach an excellent contrast, as seen on figure 3.14. One may obtain a similar effect by simply putting the light source perpendicular to the axis of the microscope. The polarizing method has the advantage of reducing glares and enhancing

edge sharpness. It is also useful to illuminate properly the part of the fibre close to the envelope of the droplet, which makes up tmost of the wetted fibre length.
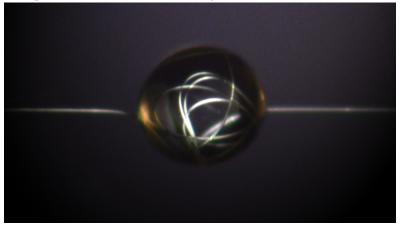
Figure 3.14 – Micrograph of the coiling of a TPU fibre in a silicone oil droplet under polarized light.

This shows qualitatively that the windlass mechanism is a purely mechanical phenomenon and may be realized with any material, as highlighted in section 3.2. We characterised the mechanical properties of the artificial windlass system below.

Correlation between force and shape   The force measurements are performed using the experimental setup described in figure 2.4, in combination with synchronized video recording under microscope with polarized light. The synchronization is simply done by starting both measurements at the same time. Figure 3.15 compares the mechanical properties of the drop-on-coilable-fibre system with the raw fibre.
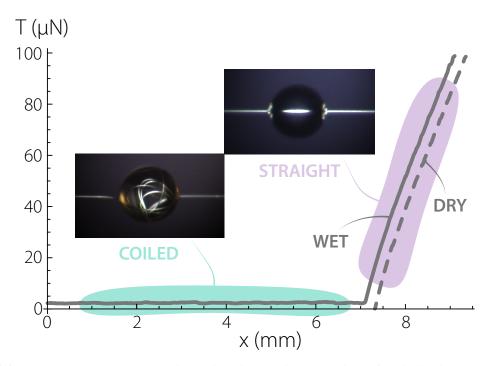
Figure 3.15 – Force measurements combined with microscopic observations of a windlassing system (solid line) compared with the characteristics of the simple fibre (dashed line).

The elastic regimes, occuring when the imposed length is larger than the rest length of 7.2 mm, are quantitatively the same for the drop-on-fibre and for the raw fibre. The slight shift of the two force curves is mainly due to the measurement error on the absolute value of the length of the sample. Nevertheless, the slopes (which represent the stiffness) do match. This means that the solid regime of the windlassing sample is a simple stretching of the core fibre. However, below the rest length, the raw fibre buckles globally whereas the drop-on-fibre sample stays tight and under tension. This produces a plateau in force slightly above zero, which is a signature of the local coiling of the fibre. The value of the force plateau is given by equation (3.2). The ability of the drop to store fibre is a **shape-induced functionalisation**, i.e. the addition of functionality through geometry. This links the local shape of the fibre to its mechanical properties, which usefulness is harvested here. This is correlated with the new vision of the buckling instability in the mechanics community described in section 1.4.2.

In the next chapter, we push the study of the windlass mechanism further, and discuss the influence of parameters at play both theoretically and experimentally.

"Love is a better teacher than a sense of duty." — *Albert Einstein*

Contents

THIS chapter aims at bringing the comprehension of the windlass mechanism further, by giving a view of some of its subtilities. The details of coiling activation are first described, both in terms of size characteristics of the fibre/droplet couple and in the force profile when the coiling starts. The far post-buckling regime is then analyzed, as well as the complex equilibria of this non linear system. Finally, we show that gravity might influence the drop-on-coilable-fibre systems in numerous ways.

4.1 Coiling activation

The first way to quantify the windlass mechanism is to test whether a given fibre/drop couple will coil or not. This was done on various fibre materials and liquids. In each case, the coiling (or absence of it) was tested by placing the drop on the fibre and slowly compressing the sample. If coiling does not occur, the compression is repeated over several cycles. If coiling still does not occur after 5 cycles, the sample is declared not coilable. The diameters of the fibre and of the drop are measured optically, as well as contact angles (see appendix B.1.1). Intrinsic material properties are taken from datasheets. Results are summarized on figure 4.1.

In order to characterise the system further, we use a unique dimensionless number, that compares the magnitude of the compressive capillary force and the local critical buckling force (see equation 1.6):

$$C_{\text{Buck}} = \frac{F_\gamma}{F_{\text{Buck}}} = \frac{2\pi\gamma r \cos\theta_Y}{\pi^2 \frac{EI}{D^2}} \tag{4.1}$$
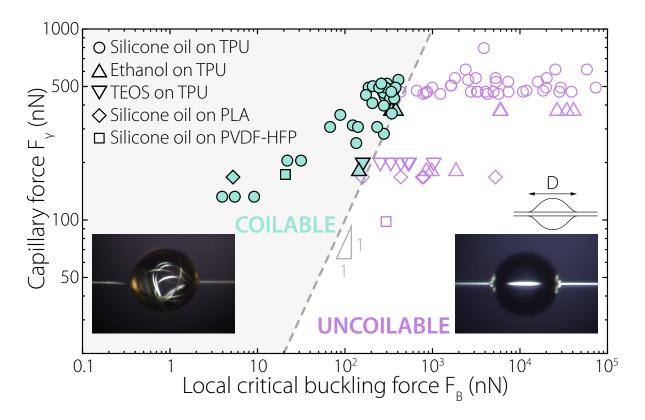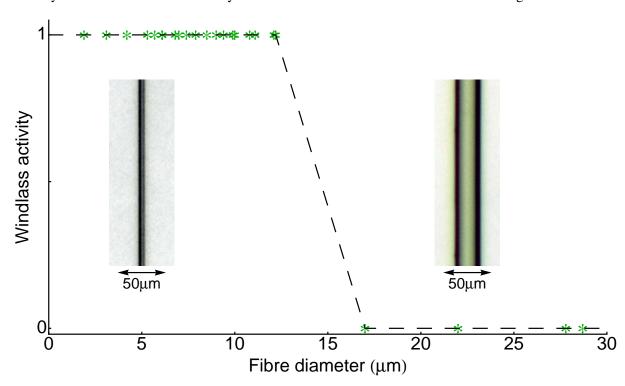
Figure 4.1 – Coiling activation as a function of capillary force for several fibre/drop couples of materials. Coiling is activated if the wetting force is higher than the local critical buckling force (the dashed line represents the frontier). The filled green symbols represent the drop-on-(coiled)-fibres, and the hollow purple symbols represent the drop-on-(straight)-fibres.

with γ the surface tension of the liquid, r the radius of the fibre, θ_Y the contact angle of the liquid on the material the fibre is made of, E the Young's modulus of the fibre, I the inertia moment of the fibre ($I = \frac{\pi r^4}{4}$ in case of a cylindrical fibre of radius r), and $D = 2R$ the diameter of the droplet. Here the droplet is assumed quasi spherical for ease of calculation. Real droplets include a boundary part at the meniscii location, which serves to reconnect the perfect spherical shape to the requirement of the Young-Dupré contact angle. This increases slightly the actual buckling length, from the drop diameter to the drop diameter plus the meniscii length. In the following, the drop diameter cumulated with the meniscii length will be referred to as the drop size. The experimental data take into account this actual drop size for a faithful description of the buckling phenomenon.

If our assumptions are right, the transition from the classical drop-on-(straight)-fibres to drop-on-(coiled)-fibres should appear at $C_{\text{Buck}} = 1$. Reporting the previous experiments in a dimensionless graph shows a transition from drop-on-(rigid)-fibre to coiling at $C_{\text{Buck}} = 0.97 \pm 0.15$, in accordance to what was predicted. Furthermore, equation (1.6) predicts the maximum diametre of the TPU coilable fibre when coupled with silicone oil. Using $\gamma = 21.1$ mN m^{-1}, $\theta_Y = 23 \pm 3°$, $\rho = 960$ kg m^{-3}, $E = 19 \pm 3$ MPa yields a critical diameter of 15.8 ± 1 µm. This represents another way to look at the coiling transition, through the increase of the fibre bending rigidity until it cannot be coiled any more. Dozens of fibres have been produced for this experiment, with radii varying from 1 to 40 µm. As highlighted in section 3.1.2, the subcritical nature of the transition induces a binary structure of the coiled status, i.e. "all or nothing". If the coiling begins, the sample is given the activity value of 1. If there is no coiling (characterised by the sagging of the sample under the drop's weight), the sample is given an

activity of zero. The windlass activity as a function of the fibre diametre is shown in figure 4.2.

Figure 4.2 – Windlass activation transition when the (TPU) fibre radius is changed through the threshold. The small fibre shown in the left inset has a diameter of 6.7±0.7 µm and the large fibre diametre is 28.3±0.7 µm.
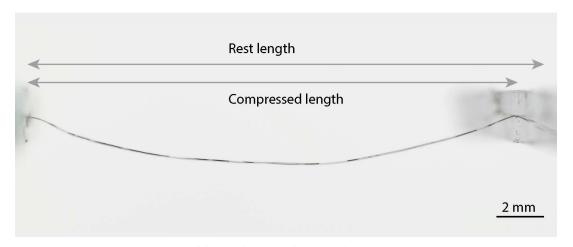
The biggest fibre with which coiling was achieved was 12.2±0.7 µm and the smallest non coilable fibre was 17±0.7 µm, so the critical diametre for "coilability" is 14.6±2.4 µm, in accordance with equation (1.6). The gap in term of diametre between the tested fibres is due to the difficulty to produce regular smooth fibres with our procedure, that paradoxically works much better for fibres below 8 µm.

This shows that the fully mechanical picture of the drop-on-fibre system is quantitatively correct. This highlights as well the nature of the hinges at the liquid meniscii (pinned-pinned, free to rotate). The coiled system and the classical drop on fibre system owe their difference to the existence of meniscii forces, that will be discussed in the next section. Additionnally, the next step of refinement in the model of the coiling mechanism, consisting in the precise quantification of windlass activity, is still an open problem. Nonetheless, a first answer is given in sections 4.4 and 4.6.

4.2 Macroscopic consequences of the existence of the meniscii
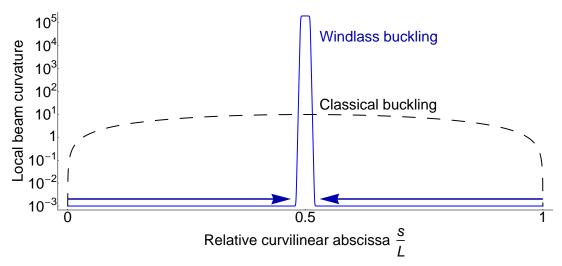
The main difference between a simple fibre and a drop-on-fibre system is the existence of local meniscii forces, that induces a zone of over-compression and a way towards symmetry breaking. This is reminiscent of the wrinkle to fold transition of thin films, where deformation localises (Pocivavsek et al., 2008). Localisation implies that the deformation concentrates from all areas into defined spots. This is what happens during the windlass transition, with the droplet harvesting all the curvature. The sharpness of the curvature localisation may be seen on the periphery of the droplet. There is a zone of transition between very high curvature and quasi-null curvature. The extension of this zone is on the order of a few drop sizes, see figure 4.3.

This curvature localisation has several implications. The global buckling state still exists, but at much smaller sample length, only when the windlass has reached its limits. This is discussed in section 4.4. This has a strong influence on the natural length of the sample (called the rest length) and its apparent extensibility. Rest length is usually defined as the point of zero force, but in the case of thin and long filaments, it is very close to the length under which the sample globally buckles. Thus, the windlassed system has a much smaller rest length than the fibre it is made from. Normal fibres globally buckle to adapt to the imposed length, while windlass fibres have the freedom to locally coil. This made possible the creation of samples of spectacular apparent extensibility, with a maximum recorded at a mindblowing 50,000% extension at break. This will be further discussed in section 4.4. The mechanical response of the windlassed fibres has been measured, discussed and compared with simple fibres in section 3.3.2. The ability of the drop to store fibre is a **shape-induced functionalisation**, i.e. the addition of functionality through geometry. As such, the drop may behave as perfectly soft, or with a finite modulus. Thus, the drop-on-coilable-fibres may be described as **liquid-solid mechanical hybrids**, that combines the possibilities of both. The easiest way to witness the difference is through the behavior in compression, see figure 4.3. This will be further discussed in term of forces in section 4.3.2.

(a) Classical buckling experiment.

(b) Windlass buckling. The green halo is due to diffraction.

(c) Theoretical dimensionless curvature profiles of classical and windlass buckling.

Figure 4.3 – (a) Classical buckling and (b) windlass buckling experiments show typical curvature profiles of the corresponding samples. While the raw core fibre has a global curvature, the drop-on-coilable-fibre presents a curvature localised mostly inside the drop, linked through a boundary region to the dominant straight fibre. (c) Theoretical local curvature as a function of the dimensionless curvilinear abscissa s. Here the fibre rest length is L=1 cm and the drop size is D = 100 μm.

4.3 Experimental subcriticality

It has been explained in section 3.1.2 that the windlass transition is of subcritical nature. In this section we show two consequences of this subcritical nature: the hysteresis of coiling threshold and a negative stiffness regime slightly after the coiling has started.

4.3.1 Highlights of an hysteresis

As seen in section 3.1.2, the force needed to preserve the coiling when it exists is roughly fivefold smaller than the force to induce coiling on a straight fibre. In practice, this means that the post-buckled fibre accepts a higher curvature than the pre-buckled fibre. In term of droplet sizes, the deactivation radius is $\sqrt{\frac{\pi^2}{2}} \approx 2.2$ times smaller than the activation radius, as given in equation (3.3). This theoretical results is verified experimentally by evaporation of a windlassing droplet.

To test the difference between activation of the coil and deactivation when it already exists, a mist charged with ethanol microdrops is sent onto a TPU fibre in a confinement chamber (see section 2.2.2). In those conditions, a drop can reach 400 μm with a well closed chamber. But observation is enhanced if the chamber is opened. As these large drops have a lifetime on the order of the minute (see section 3.3.1), quasi-static observations are still possible.

Ethanol droplets large enough to coil are deposited on a TPU fibre. The resulting system is compressed and the biggest droplet starts coiling some fibre in. Then the ethanol mist flow rate is slowly decreased, so that evaporation operates droplet size reduction in a quasi-static manner. Quasi-static is defined with the timescale for coiling rearrangement, which will be discussed in section 4.7. The drop size is recorded throughout evaporation, and curvatures above the activation maximum curvature are measured. This is in accordance to the theory of subcritical transitions, and leads to the apparition of a coiling hysteresis and a dependence on previous history, as shown in figure 4.4.

During evaporation, the drop gives away some fibre, but the coiling remains. When the drop reaches
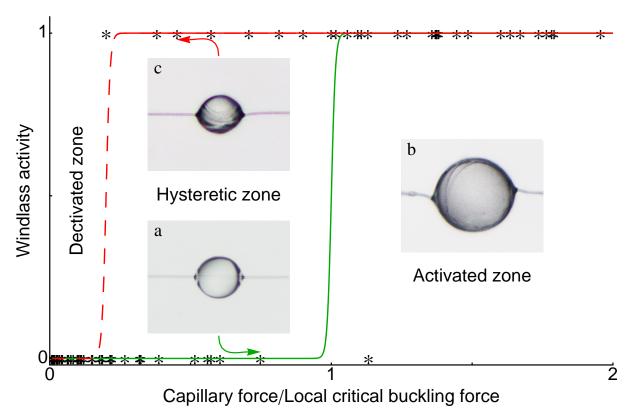
Figure 4.4 – Windlass hysteresis owes its existence to the fact that it is easier to keep curvature when it exists, that to create some when there is none. The fibre is made of TPU and measures 5.4±0.7 μm in diameter. The scale is the same on all pictures. Insets (b) and (c) show a windlassing droplet during its evaporation. The large drop in (b) is 165 μm in diameter, whereas the small evaporated drop in (c) is 103 μm. The in-drop fibre bending energy throughout evaporation increases a eightfold.

the deactivation radius, the fibre is expected to completely uncoil and recover the classical drop-on-fibre shape. Instead, a structural instability occurs, leading to complex tridimensionnal regular patterns that could be useful in micro-fabrication, as explained in section 5.6. Below we quantify experimentally the subcritical nature of the windlass transition.

4.3.2   Force undershoot at coiling activation

In practice, the subcritical nature of the windlass activation results in a negative stiffness regime when coiling starts. The force then stabilizes onto a plateau, in accordance to the phase transition formalism explained in section 3.1.1. There is thus an undershoot force at the coiling onset, which is of help in the accurate quantification of the windlass subcritical nature. Owing to the low intensity of the forces at stake (typically μN), we use highly sensitive capacity deflection force sensors, as explained in section 2.2.2. However, those sensors have the drawback of drifting slowly with time. While it only adds slightly to the measurements errors in the rapidly performed tests (less than five minutes), this can lead to substantial offset in longer tests. Appendix B.2 presents a method to measure the force of a drop on the straight fibre in situ. Equation (3.2) is then used to compensate the plateau to its supposed value. This allows for direct comparison between numerical simulations and experimental data, as shown on figure 4.5.

The numerical simulations only use measured physical parameters (e.g. drop diameter, fibre radius, liquid surface tension,...), i.e. there is no fitting parameter. This is strong evidence that the coiling mechanism works as we explained it so far. In addition, one may notice that, on top of the essentially
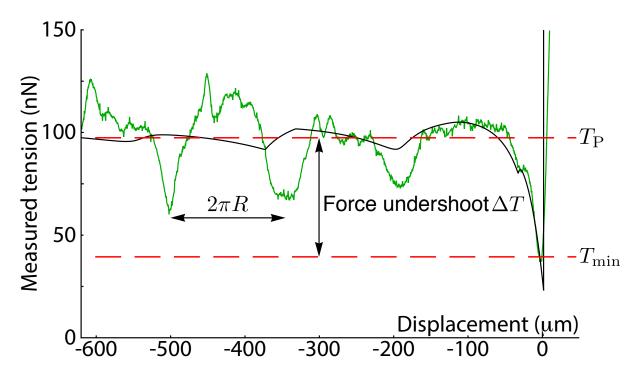
Figure 4.5 – Force measurements at the coiling transition. Comparison between numerical simulation (black line) and experimental data (green line) on a TPU/silicone oil system (droplet diameter 62 μm and TPU sample (see section 3.3.1). The single coil period and the initial negative stiffness regime (and subsequent undershoot) are well reproduced.

flat shape of the plateau, it exists a structure with well defined period. The cycles correspond to one coil. The oscillations are thought to come from in-drop rearrangement, thus leading to a local force minimum when the internal fibre wetted length is a integer times the perimeter of the drop. The amplitude of the oscillations decreases when the system is further from the threshold, and becomes essentially flat (below sensor resolution) at $C_{\text{Buck}} > 30$.

Furthermore, upon using the dimensionless capillary force $f_\gamma = \frac{2\pi\gamma r \cos\theta_Y}{EI/D^2}$ and the dimensionless tension $t = \frac{T}{EI/D^2}$, with T is the dimensionalized tension and $D = 2R$ the drop size, it is found that the minimum tension at activation $t_{\min}$ is analytically given by equation (4.2). It is to be noted that $C_{\text{Buck}} = \frac{f_\gamma}{\pi^2}$. For further details, see publications in appendix F.

$$\sqrt{f_\gamma - t_{\min}} + \sqrt{t_{\min}} \tan\left(\frac{\sqrt{f_\gamma - t_{\min}}}{2}\right) = 0 \qquad (4.2)$$

The combination with the formula for the plateau force, given in equation (3.2), yields analytical values for the force undershoot $\Delta T = T_{\text{P}} - T_{\min}$. It is measured experimentally by use of the difference between the minimum force and the average value of the plateau force, taken over at least three cycles. This definition of the quantitative undershoot force avoids the problem of sensor drifting exposed above. For each sample, the undershoots are measured three times, and the average value is kept, so that noise measurement are reduced. System parameters have been varied and the corresponding force-displacement curves were recorded, from which undershoot forces were extracted. As explained in appendix D.5, the intended measurements are at the limit of the sensor resolution, which is at the nanonewton scale. As a consequence, we can only measure time changes in force in the present conditions, not an absolute value. An compensating offset is thus applied to each force-displacement curve so that the force plateau corresponds to equation (3.2). However the main measured quantity, the force

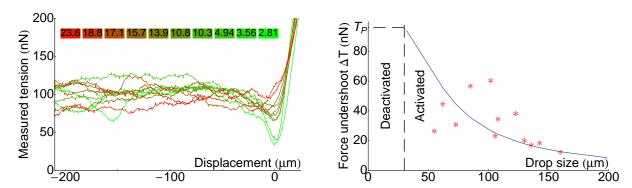undershoot, is not changed in the process. Results are given in figure 4.6.

Figure 4.6 – Left: Force-displacement tensile curves for different droplet sizes. The given numbers are the corresponding C_{Buck} numbers, from the smallest (green) to the largest (red). Right: Undershoot force as a fonction of drop size. The theoretical results (equations (3.2) and (4.2), solid line) match the experimental data reasonably well, considering the absence of use of any fitting parameter. As the critical diameter corresponds to $t_{\min} = 0$, the undershoot equals the plateau force T_{P} given in equation (3.2).

There is a good agreement between the analytical and the experimental values, considering the absence of use of any fitting parameter. Unexpectingly, there is a difference between traction and compression undershoot values. On average, compression undershoots are two times higher than traction undershoots. The results shown above are for traction undershoots. As this difference is not reproduced by numerical simulations, further theoretical work is needed.

The subcritical behavior of the windlass transition may also be seen in the strong discontinuity of the coiled length, which will be discussed in combination with the limits of the coiling in section 4.4.

4.4   What are the limits of the windlass ?

Packing of elastic structures have been studied in literature from the point of view of statistical physics (Deboeuf et al., 2009; Katzav et al., 2006). The initial intuitive image of the windlass limits is the droplet being "full" of fibre. However, to fit a more realistic picture, the coiling is modeled as filling the droplet until the radius of curvature of the next coil is too high to be sustained by wetting energy gain. This limit is characterised by the deactivation drop radius given in equation (3.3). The droplet is filled with packed coils of fibre from its equator up to a threshold latitude. At the poles the curvature would be too high. That defines the highest point on the sphere occupied by fibre coils, as shown on figure 4.7. It is characterised by an angle in spherical coordinates φ_j with $\sin \varphi_j = R_j/R_{\text{deac}}$, with R_{deac} the deactivation radius. When a sphere is completed the fibre is sorted on the next spherical layer, spiralling towards the center. There is a forbidden central sphere of radius R_{deac}, see figure 4.7.

Here bending is the dominant energy cost, and leads to an equilibrium wetted fibre length. The same analysis has been used by Stoop et al. (2011). The fibre arrangement is assumed tightly packed. As a consequence, the surface S_j of the j$^{\text{th}}$ spherical layer of radius R_j is fully occupied (except on the poles as described). The lenght of fibre on this layer is thus $\ell_j = \frac{S_j}{2r}$. The radius of jth spherical layer is $R_j = R - 2rj$, with R the drop radius and r the fibre radius. The number of spherical layers $N_{\max}$ is approximated to $\frac{R - R_{\text{deac}}}{2r}$. We use this approximation as there is always a large number of spherical layers that are occupied. This is justified by the subcritical nature of the transition. The maximum coilable in-drop length L_{max} is finally given in equation (4.3c). The validity of the assumptions required for this calculation will be discussed and refined in section 4.5. Nevertheless, orders of magnitude are well
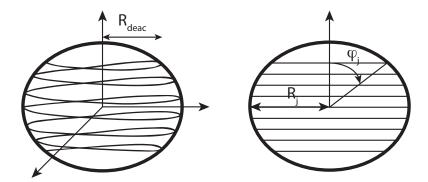
Figure 4.7 – Idealised packing of the fibre inside the drop. The fibre runs tightly in the drop until its local curvature is too high to be sustained by wetting energy. For clarity of visualization, the fibre is represented with a low coil density. Close contact is observed in reality.

represented by the reasoning below.

$$\ell_j = \frac{S_j}{2r} = \frac{1}{2r} \int_{\varphi_j}^{\pi/2} 4\pi R_j^2 \sin \varphi d\varphi = 2\pi \frac{R_j^2}{r} \cos \varphi_j \tag{4.3a}$$

$$L_{\max} = \sum_{j=1}^{N_{\max}} \ell_j \approx \int_0^{N_{\max}} \ell_j \, dj = \frac{\pi^2}{r^2} \int_{R_{\mathrm{deac}}}^{R} R_j^2 \cos \varphi_j \, dR_j \tag{4.3b}$$

$$L_{\max} = \frac{\pi^2}{r^2} \int_{R_{\mathrm{deac}}}^{R} R_j \sqrt{R_j^2 - R_{\mathrm{deac}}^2} \, dR_j = \frac{\pi}{3r^2} \left(R^2 - R_{\mathrm{deac}}^2 \right)^{3/2} \tag{4.3c}$$

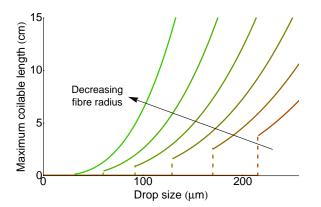With r the fibre radius, R the drop radius, R_{deac} the deactivation radius given in equation (3.3).

For our typical cases, we find that a 100 µm radius droplet could accomodate 12 cm of 4 µm diameter fibre, which is equivalent to more than 180 coils in the drop. To bring it to the reader scale, it would be like having an automatic coiling system the size of a tennis ball able to store 50 meters of 1mm rope. Considering the present assumptions, the bigger the droplet the higher the coil. The maximum coilable length of a given fibre is thus reached for the largest sustainable drop (see equation (1.5)). Equation (4.3c) for $R = R_{\max}$ yields

$$\mathrm{L}_{\max}^{\max} = \frac{\pi}{r} \frac{\gamma \cos \theta_Y}{\rho g} \left(1 - \frac{2}{\pi^2} \left(\frac{r}{r_{\mathrm{crit}}} \right)^{7/3} \right)^{3/2} \tag{4.4}$$

with r_{crit} the critical radius of coilable fibre given in equation (1.6). Notice that for small fibres, the maximum coilability diverges with the fibre radius $L_{\max}^{\max} \propto \frac{1}{r}$. Considering a TPU fibre/silicone oil droplet system, a comprehensive view of the parameters influencing the maximum coilable fibre length is given in figure 4.8.

Notice that there is a discontinuity of the maximum coilable fibre length, intimately linked to the subcritical nature of the windlass mechanism. For thin fibres (in comparison to the critical coilable fibre radius given in equation (1.6)) it goes almost unnoticed but for thicker fibres it can be on the scale of tens of centimeters. Considering the largest sustained droplet on its corresponding fibre, the maximum coilable fibre length also quickly reaches meters. Notice that for the critical fibre radius (given in equation (1.6)), the maximum coilable fibre length goes suddenly to zero.

In practice, the apparent maximum extensibility of a drop-on-fibre system is dramatically increased thanks to the windlass mechanism. A fibre of rest length L_0 can be entirely coiled in the drop if its
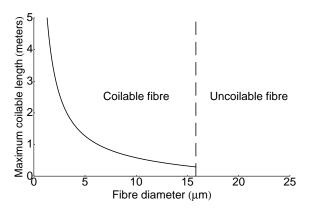
Figure 4.8 – Left: Maximum coilable fibre length L_{max} as a function of drop size (see equation (4.3c)) for several fibre diameters (2, 3, 4, 5, 6, 7 μm). Materials properties used are those from TPU fibres and silicone oil droplets. Note the sharp discontinuity (dashed line) when the windlass is activated, quickling reaching centimeters for micronic droplets. Right: Maximum coilable fibre length in the largest sustained droplet $L_{\text{max}}^{\text{max}}$ under equation (4.4). This quantifies the "coilability" of a fibre through the windlass system.

length is smaller than the maximum coilable length, i.e. $L_0 < L_{\text{max}}$. In this case, the new rest length of the system is the drop size $2R$. If the fibre is too long, i.e. $L_0 > L_{\text{max}}$, the sample can be compressed only by $L_{\text{max}} - 2R$ until it globally buckles. Thus the new rest length is $L_0 - (L_{\text{max}} - 2R)$. Noting ϵ_0^{max} the maximum extensibility (strain at break) of the material the fibre is made of, the apparent maximum extensibility of the system is given by

$$
\epsilon^{\text{max}} = \begin{cases} \dfrac{L_0 \left(1 + \epsilon_0^{\text{max}}\right) - 2R}{2R} = \dfrac{L_0}{2R}\left(1 + \epsilon_0^{\text{max}} - \dfrac{2R}{L_0}\right) & \text{if } L_0 < L_{\text{max}} \\[3mm] \dfrac{L_0 \left(1 + \epsilon_0^{\text{max}}\right) - (L_0 - (L_{\text{max}} - 2R))}{L_0 - (L_{\text{max}} - 2R)} = \dfrac{\epsilon_0^{\text{max}} + 1}{1 - \frac{L_{\text{max}} - 2R}{L_0}} - 1 & \text{if } L_0 > L_{\text{max}} \end{cases}
\tag{4.5}
$$

The apparent extensibility thus depends on the rest length of the core fibre. While this could not happen in one-component systems, this shows once again the possibilities granted by the windlass mechanism. The apparent maximum extensibility is plotted as a function of the fibre rest length in figure 4.9.

The apparent extensibility has intuitive natural limits, $\lim_{L_0 \to 2R} \epsilon^{\text{max}} = \epsilon_0^{\text{max}}$ and $\lim_{L_0 \to \infty} \epsilon^{\text{max}} = \epsilon_0^{\text{max}}$. The windlass mechanism has an influence only in between those limits. To put figures, the lower limit $2R$ is on the order of 100 μm and the upper limit can be defined as $10L_{\text{max}}$, which is at the meter scale. There is thus a wide range of influence for the windlass.

The apparent extensibility has a maximum for $L_0 = L_{\text{max}}$. Considering typical values for the physical parameters, the apparent extensibility of the drop-on-fibre system is found to be increased a thousandfold in our experiments. Given the independance of the fibre length upon the drop and the fibre radii, dramatically large extensibility improval are theoretically reachable. It is also worth noting that materials with intrinsically low maximum extensibility can be given a very large apparent maximum extensibility through the windlass mechanism.

Although the picture of tightly packed fibres is quite realistic, in practice self-contact builds up residual stress. This forbids the coiling from restructurating when more wetted fibre length is added. This also blocks fibres, especially when they are close to the critical coilable fibre radius. This will be exploited to create microtangles in section 5.6. However, this effect is not dominant in most cases, and samples with apparent extensibilities of up to 50,000% have been successfully prepared.
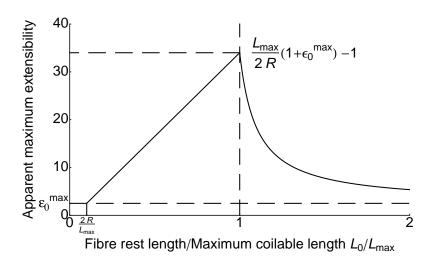
58
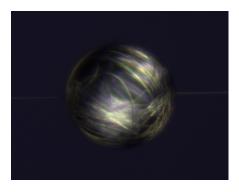
Figure 4.9 – Apparent maximum extensibility of the drop-on-coilable-fibre system as a function of the core fibre rest length, from equation (4.5). The initial shift is due to the fact that the drop size is a lower physical bound for the fibre rest length to be used. The maximum extensibility of the core fibre is $\epsilon_0^{max} = 2.5$ in the case of TPU. The important parameter $\frac{L_{max}}{2R}$ was taken to be 10 for clarity of the graphic, but in typical case it is on the order of thousands, enhancing the contrast of extensibility between the simple fibre and the drop-on-coilable-fibre system.

In addition to self-contact, other parameters can change the limits of the windlass. Gravity may influence the arrangement of the coiling, as will be shown in section 4.6. The envelope of the droplet can adjust to specific pressure fields. The deformation of the droplet is thus strongly connected to the coiling morphology, as is explained in the next section.

4.5 Coiling morphology and related droplet deformation

4.5.1 Different morphologies

In the last section the coiling was considered ordered and tightly packed, for ease of calculation. However, the actual coils inside a droplet may be arranged in several ways. The typical coil morphology is in between the completely ordered state and the completely disordered state, both shown on figure 4.10.

Figure 4.10 – Polarized light reveals the different morphologies of coiling in the TPU fibre/silicone oil droplet system: disordered (left) or ordered (right). The dark background is due to the polarizing technique.

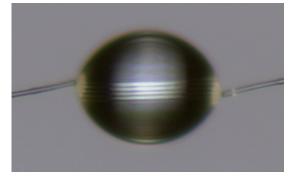One may think that a given drop-on-fibre system would have a given coiling morphology. But it is not so simple. The coiling morphology depends on the amount of fibre inside the drop. The morphologies of thin wires packed into spherical cavities have been studied both experimentally and numerically by other groups (Stoop et al., 2008, 2011). They found that the system is dominated by bending energy, as would be expected. Furthermore, the morphology of the coiling can be changed by applying torsion. If torsion is relaxed (by axial rotation for instance), the coiling is ordered, whereas in the case of axial blockage, the resulting coiling is disordered. This is because an ordered coiling builds up twist which destabilises it. The disordered coiling also has a destabilizing energy component, which corresponds to the additional curvature required for the coiling to leave its main axis and occupy the whole sphere. The comparison between both modes decides which coiling morphology is energetically favorable. Figure 4.11 shows morphologies of wires packed into spherical cavities (reproduced from Stoop et al. (2011)).
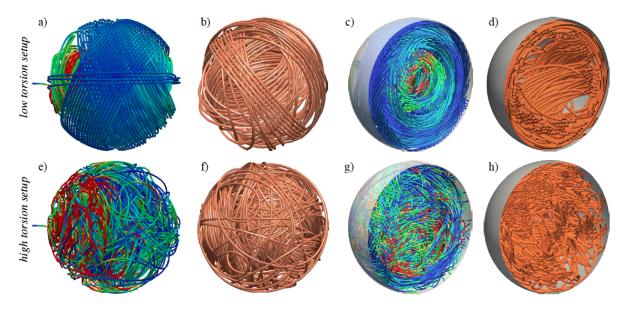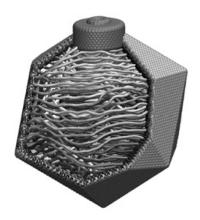
Figure 4.11 – Morphology of a fibre coiled in a rigid container, from Stoop et al. (2011). Color represents the bending energy from blue (low) to red (high).

The top row provides low torsion setup and results in an ordered morphology, characterised by ring-like coiling (a). A cut through the packing (c) reveals the shell-like inner structure. X-ray tomography scans from experimental realizations are shown in (b, d). The use of X-rays allows a look through any sample as well as a useful 3D reconstruction. The bottom row shows that the high torsion setup produces disordered structures see (e, g), with corresponding experiments in (f,h).

These results have implications for viral capsids, as the amount of DNA packed in a capsid limits the genetic information the virus can spread (Purohit et al., 2003). The use of multivalent cations allows the disruption of DNA self-interactions, leading to the freedom of changing the morphology of DNA packing, as shown in figure 4.12. This has found interest in the understanding of condensed states of DNA for many communities (Leforestier and Livolant, 2009).

However, the deformability of the droplet envelope brings another degree of freedom that complexifies the phase diagram for morphological transitions. We have observed that a droplet may take different shapes, depending on the in-drop fibre coiling. The relation between drop deformation and coiling morphology is quantified in section 4.5.2.
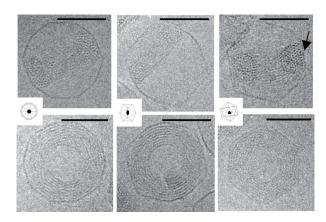
Figure 4.12 – DNA coiling in viral capsids. Left: Cutaway view of a single coaxially coiled conformation for a model virus. Right: Cryoelectron microscopy of T5 bacteriophages viral capsids, revealing the internal DNA structure. Sources: Petrov and Harvey (2008) (left) and Leforestier and Livolant (2009) (right).

Droplet-axisymmetry breaking   As coiling occurs, the droplet experiences a new pressure field from the in-drop fibre. The fibre pushes on the drop enveloppe outwards with a force F of magnitude $F \propto \frac{\partial}{\partial R}\left(\frac{1}{2}\frac{EI}{R^2}\right) = \frac{EI}{R^3}$ per unit length of fibre. Depending on the morphology of the coiling, this pressure field may be inhomogeneous, thus inducing symmetry breaking in the droplet shape, see figure 4.13. When the fibre is straight, the droplet takes an undoloidal shape, reminiscent of a rugby ball (see appendix B.1), that is axisymmetric along the fibre axis. If the coiling is ordered, it has its own main axis (usually perpendicular to the fibre main axis) and may impose it upon the droplet shape. And it will eventually become ordered when more fibre is added, as deformation of the droplet would mean a smaller curvature for the in-drop fibre. This is quantified explicitly in section 4.5.2.
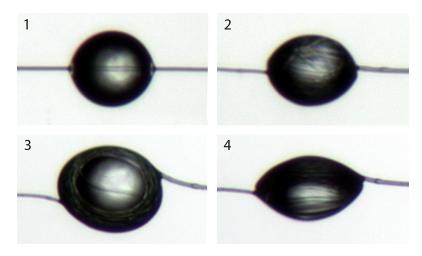
Figure 4.13 – As the in-drop fibre length increases (from 1 to 4), the initial axisymmetry of the droplet may be broken, resulting in an ellipsoidal shape. 3 and 4 are rotated views of the same droplet, showing the breaking of symmetry.

Figure 4.13 shows the breaking of symmetry of the droplet. In (1), the fibre is straight. In (2), the drop contains 18 coils, and mainly retains its original shape. In (3), the drop has coiled approximately 24 coils. The axisymmetry of the droplet vanishes as the internal fibre coiling establishes its order. (4) has slightly more in-drop fibre length, and has undergone rotation with respect to the fibre, revealing the main axis of the drop, corresponding to the coil axis.

4.5.2 Quantification of drop deformation

It has been observed in the last section that the in-drop fibre coiling may deform substantially the droplet. This deformation comes from different sources. The droplet is deformed by the simple entry of fibre as the envelope of the droplet extends to accomodate the cumulated volume of both drop and fibre. The related deformation is then

$$\frac{R - R_0}{R_0} = \frac{1}{3} \frac{V - V_0}{V_0} = \frac{1}{3} \frac{\pi r^2 \ell}{\frac{4}{3}\pi R_0^3} = \frac{\pi}{2} n \left(\frac{r}{R_0} \right)^2 \tag{4.6}$$

with R_0 the radius of the initially spherical droplet, r the fibre radius, ℓ the total wetted fibre length and $n = \frac{\ell}{2\pi R_0}$ the apparent coil number. Furthermore, the coiling itself may impose a non-axisymmetric pressure field and stretch the droplet to minimize the fibre curvature. The deformed droplet shape is modeled as two spherical cap of major axis R, depicted on figure 4.14.
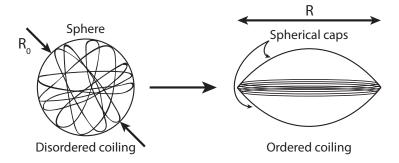
Figure 4.14 – Spherical cap model of the droplet deformed by ordered in-drop fibre coiling.

The resulting drop-on-(coiled)-fibre shape is an equilibrium between the bending energy of the fibre and the surface energy of the deformed droplet. Minimizing the energy of the system under a constraint of constant drop volume and for small surface perturbation, the deformation of the drop is given by:

$$\frac{R - R_0}{R_0} \simeq \frac{\ell}{8\pi \frac{\gamma R_0^4}{EI} + 3\ell} = \frac{n}{\frac{\pi}{2} \frac{R_0}{r} \frac{C_{\text{Buck}}}{\cos \theta_Y} + 3n} \tag{4.7}$$

With R the major axis of the ellipsoid, E the Young's modulus of the solid fibre, γ the surface tension of the liquid droplet and θ_Y the contact angle of the drop on the fibre. At low in-drop fibre length $n \ll \frac{\gamma R_0^3}{EI}$ and for $S = 1$, we recover a formula reminiscent that found by Roman and Bico (2010) for a similar drop-on-coilable fibre system. However, the conditions they used differ slightly for the boundary conditions, as they consider a fibre free at one end.

We have now a theoretical way to calculate the drop deformation in both ordered and disordered coiling mode. But the reality may be in between. To quantify it, we refer to the field of liquid crystals (De Gennes and Prost, 1993) and define an orientational order parameter thanks to the second Legendre polynomial, given in equation (4.8). S measures the order of an assembly of vectors. For $S = 0$ the system is completely disordered. For $S = 1$, the system is perfectly ordered.

$$S = \langle P_2(\cos \psi) \rangle = \left\langle \frac{3 \cos^2(\psi - \langle \psi \rangle) - 1}{2} \right\rangle \tag{4.8}$$

where ψ is the angle between the fibre axis at each coil and the initial fibre axis, and $\langle \rangle$ denotes the spatial average. An universal formula is found using equations (4.6) to (4.8) for any coiling morphology

from disordered to ordered:

$$\delta R = \frac{R - R_0}{R_0} = \frac{nS}{\frac{\pi}{2}\frac{R_0}{r}\frac{1}{\cos\theta_Y}C_{\text{Buck}} + 3n} + n\frac{\pi}{2}\left(\frac{r}{R_0}\right)^2 \tag{4.9}$$

Equation (4.9) is tested experimentally by measuring both the order parameter and related deformation δR for a large number of drop-on-fibre systems. The deformation of the droplet is measured optically as a change of its length along the main fibre axis. The cumulated in-drop fibre length is easily measured as the compression distance from the rest length, given by the caliper or the microstep motor. The order parameter might be tricky to measure experimentally for our case, as the fibre is in a 3D sphere and is observed in a 2D plane. To minimize that effect, we choose in situ a point from which the near morphology looks representative. We then find the closest fibre point and measure the local fibre axis angle. Repeating the same measurement several times, we found a measurement error of $\pm\,0.2$ in order parameter, especially high for the states neither ordered nor completely disordered. This measurement error is increased by the fact that the order parameter is normally considered in large-size samples, though in our case coil number as low as $n = 5$ have been studied. In this case the measurement has less meaning. Typical results are given in figure 4.15.
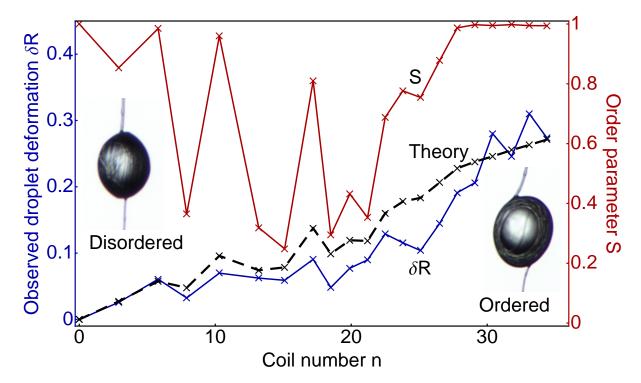
Figure 4.15 – Typical drop deformation and fibre coiling morphology of drop-on-coilable-fibre systems. Comparison between the measured deformation (bottom blue curve) and the theoretical prediction (middle dashed black curve) from equation (4.9), linked through the observed order parameter S (top red curve). The droplet may be deformed by two different mechanisms: the simple entry of fibre adding volume, and the non axisymmetric pressure field of the in-drop coiled fibre. The theoretical formula (4.9) modeling the deformed droplet as two spherical caps is well verified within the measurement errors. Fluctuations of the droplet deformation are not measurement errors but actually related to fluctuating coiling morphology.

The simple model developed above has been verified on many drop-on-fibre systems by varying the size of both fibres and drops. This has been done with the TPU fibre and silicone oil droplet system.

Drop deformation is well predicted within the measurement error bars. The average difference between theoretical prediction and observed deformation is 15%. The large measurement error comes mainly from the difficulty of quantifying the order parameter with a simple optical setup. This can be improved by use of X-ray computed tomography. This technique uses a X-ray beam to look through the sample and reconstruct a very high resolution 3D structure (Stoop et al., 2011). In our model the order parameter S comes as an exterior measured parameter. The prediction of the coiling morphology is the next step. It seems that detailed numerical simulations are required to do so, given the complexity of the problem. However we would like to build a idealized analytical model that mimic the behavior of the system at first order. This could be done by taking into account torsion and is currently under work. A Zurich based team has recently shown that a ordered-to-disordered transition may occur for a flexible filament in an elastic confinement by changing the confinement flexibility and/or the self-friction coefficient of the filament (Vetter et al., 2013, 2015). A close evaluation of the ressemblances and differences of the two problems might shed light on the very details of this complex non-linear problem.

Another sign of this complexity resides in the large fluctuations of coiling morphology at low inserted fibre length, as seen in figure 4.15. This is a signature of occasional re-ordering in spherical mode. These rearrangements are also observed in numerical simulations. They are due to the complexity of the energy landscape of the 2D and 3D modes. From times to times the two modes energies may cross and the coiling reorders temporarily. The droplet shape acts also as a feedback loop on the coiling morphology. This makes the whole system dependent on previous sample history. A detailed description is required in order to make sense of those observations.

Care has been taken to avoid the influence of gravity in the results presented up to this point. In the next section we present the effects gravity has on the system.

4.6   Effects of gravity

In the different previous sections, we analyzed the details of the windlass mechanisms without taking into account the weight of the droplet. But gravity may play an import role in the selection of the equilibrium of the system. We define a dimensionless number that compares the weight of the droplet and the capillary force to quantify this importance:

$$C_{\text{Grav}} = \frac{Mg}{2F_\gamma} = Bo \frac{1}{3\cos\theta_Y}\frac{R}{r} \tag{4.10}$$

with M the mass of the drop, g the gravitational acceleration, F_γ the capillary force, θ_Y the contact angle, R the drop radius and r the fibre radius. C_{Grav} is proportional to the Bond number $Bo = \frac{\rho g R^2}{\gamma}$ used in literature. The difference between these two coefficients is that Bo only uses one length scale and we need two, the drop radius and the fibre radius. Furthermore the factor 2 in the capillary force comes from the two meniscii that support the drop.

The influence of the gravitational coefficient C_{Grav} on our system can be understood in term of drop shape. When C_{Grav} is close to zero, the drop shape is not influenced by the gravitational field and the drop is undoloidal. It resembles a rugby ball, as shown in appendix B.1. The limit $C_{\text{Grav}} = 1$ represents the maximum droplet that could possibly be supported by the corresponding fibre. It is to be related to what was previously seen in section 1.5. Upon using the maximum droplet size $R_{\max} = \left(\frac{3\gamma\cos\theta_Y}{\rho g}\right)^{1/3} r^{1/3}$ (see equation (1.5)), we rewrite the gravitational coefficient C_{Grav} as:

$$C_{\text{Grav}} = \left(\frac{R}{R_{\max}}\right)^3 \tag{4.11}$$

If C_{Grav} has intermediate values, the shape of the drop might be changed to accomodate its own weight. This is done by rotating the meniscii, from quasi-horizontal to an angle α that is easily found to be $\sin\alpha = C_{\text{Grav}}$ by use of a force balance (Lorenceau et al., 2004). This may induce a loss of inter-meniscus span as seen in figure 4.16.
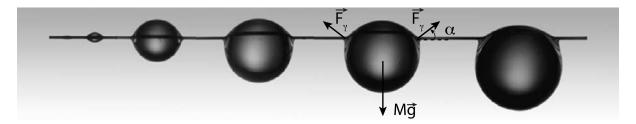

Figure 4.16 – Silicone oil droplets on fibre. The arrows represent the forces applied on the drop. Note the influence of the size of the droplet on its shape. Source: Lorenceau et al. (2004).

The new intermeniscus span would be the intersection of the (quasi)-spherical shape of the drop and the horizontal fibre, yielding equation (4.12). This equation as well as the condition of rotated meniscii are used in the next section to define the critical radius of coilable fibre in presence of gravity.

$$L_{\text{wet}} \approx 2R\cos\alpha = 2R\sqrt{1 - C_{\text{Grav}}^2} = 2R\sqrt{1 - \left(\frac{\rho g R^3}{3\gamma r \cos\theta_Y}\right)^2} \tag{4.12}$$

4.6.1 Rethinking the critical radius calculations

The meniscii may rotate to accomodate the weight of the drop. Hence for small drops the capillary force is fully compressive on the fibre, whereas for pendant drops the main part of the capillary force is to sustain the drop's weight. So instead of using equations (1.4) and (1.5), we will use the projection of the meniscii force on the fibre axis and the actual wet length to calculate the threshold value.

Rotated meniscii compression $>$ Local buckling threshold

$$2\pi\gamma r \cos\theta_Y \cos\alpha > \pi^2 \frac{EI}{L_{\text{wet}}^2} = \pi^2 \frac{EI}{(2R\cos\alpha)^2} \tag{4.13}$$

Upon using the maximum droplet size $R_{\max}$ and the activation drop radius $R_{\text{ac}} = \sqrt{\frac{\pi^2 E r^3}{32\gamma \cos\theta_Y}}$ (see equation (1.4)), the activation condition yields

$$f(R) = \left(\frac{R}{R_{\text{ac}}}\right)^2 \left(1 - \left(\frac{R}{R_{\max}}\right)^6\right)^{3/2} - 1 > 0 \tag{4.14}$$

Without gravity, $R_{\max} \to \infty$. So equation (4.14) is equivalent to equation (1.4) i.e. $R > R_{\text{ac}}$ with R_{ac} the drop activation radius. The difference between the activation conditions with and without gravity is the apparent tension that comes from the drop's weight. $f(R)$ summarizes the behaviour of the system, taking into account the capillary compression, the gravitational tension and the local buckling force threshold. We interpret $f(R)$ as the actual distance from threshold in term of force. For $f(R) < 0$ the drop does not pull enough on the fibre to induce local buckling. For high $f(R)$ the drop coils the fibre very easily. The behavior of $f(R)$ for large drop radii discussed in section 4.6.4.

$f(R)$ has a maximum for a drop of radius $R = \left(\frac{2}{11}\right)^{1/6} R_{\max} \approx 0.75 R_{\max}$. This corresponds to the most active drop on a given fibre. It minimizes the curvature imposed on the coiled fibre and the tension from its own weight. Interestingly, the most active drop has always the same $C_{\text{grav}} = \sqrt{\frac{2}{11}} \approx 0.43$.

The maximum of $f(R)$ in term of drop radius is a function $g(r)$ that depends on the fibre radius. At the critical radius of coilable fibre $g(r_{\text{crit}}) = 0$. This gives the critical radius in presence of gravity as

$$r_{\text{crit}} = \frac{2^{16/7} 3^{11/7}}{\pi^{6/7} 11^{11/14}} \frac{(\gamma \cos \theta_Y)^{5/7}}{(\rho g)^{2/7} E^{3/7}} \approx 1.56 \frac{(\gamma \cos \theta_Y)^{5/7}}{(\rho g)^{2/7} E^{3/7}} \tag{4.15}$$

Interestingly, the scaling law for r_{crit} holds with the rotated meniscii. Only the numerical factor changes. The latter is to be compared with the one in equation (1.6) where gravitational tension is not taken into account, equal to 2.27. This is a 30% reduction in fibre radius. It means that gravity tends to decrease the threshold radius value, making it more difficult to coil fibres. This is equivalent to a gravitational tension on the fibre as discussed above. The critical value for fibre diameter for TPU/silicone oil is now 10.9 μm, to be compared to 15.8 μm without gravitational tension. This is slightly smaller than the experimental threshold, found to be in the range 12.2–17 μm.

As equation (4.12) models the drop as a sphere, this differs from the actual picture by the meniscus length so that the distance over which buckling occurs is actually slightly larger. This is discussed in details in appendix B.1. In addition, the rotation of the meniscii might increase their perimeter. Both those effects make bendable fibres bigger than expected.

Gravity may have yet another effect. Pulling downward mainly at the location of the droplet, the whole system may leave its overall straight configuration and take a triangular shape. This effect and its consequences are discussed in the next section.

4.6.2   A perfectly extensible frame effect with an inextensible fibre

The frame effect is a daily life phenomenon, happening when a frame is suspended on a wall. If the typical string and nail method is used to support the frame, the string is shaped as two straight lines, and is tilted by an angle φ with respect to the horizontal reference. φ is connected to the length of the string and the weight of the frame.
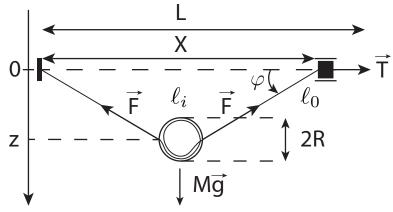
Figure 4.17 – Sketch of the frame effect with a coilable fibre. L represents the rest length of the core fibre, whereas X the compressed length, ℓ_0 the length of fibre in the air, and ℓ_i is the length of the fibre in the drop.

The fibre self-angle is defined as $\pi - 2\varphi$. This represents the angle between the two straight parts of the fibre outside the drop. When the fibre is straight (under tension), the fibre self-angle is π. When the fibre is completely folded, the fibre self-angle is 0. The recorded tension T is linked to the fibre tension F by the relation $T = F \cos \varphi$.

We assume here that the fibre outisde the drop is inextensible and has no bending rigidity. This is neglected especially with respect to the clamping points, and is a good approximation when $\sqrt{\frac{EI}{Mg}} \ll L$. We also assume that the curvature of the fibre inside the drop is constant. The drop is positioned at the middle point of the fibre. The initial symmetry is reasonably assumed to be conserved throughout the compression process. Here the loss of wet length induced by gravity seen in section 4.6 is not taken into account for ease of calculation. The results will be shown to be very close to what is observed in reality. The total energy of the system is thus given below.

$$\mathscr{E}(\varphi, \ell_i) = \frac{1}{2}\frac{EI}{R^2}\ell_i + 2\pi r \gamma_{SV}\ell_0 + 2\pi r \gamma_{SL}\ell_i - T\ell_0\cos\varphi - \frac{\ell_0}{2}Mg\sin\varphi$$

$$\mathscr{E}(\varphi, \ell_i) = \left(\frac{1}{2}\frac{EI}{R^2} - F_\gamma + T\cos\varphi + \frac{Mg}{2}\sin\varphi\right)\ell_i + \text{constant, considering } \ell_i + \ell_0 = L$$

Upon minimizing the energy with respect to the variables at play, one obtains the following equations.

$$\frac{\partial\mathscr{E}}{\partial\varphi} = 0 = -T\sin\varphi + \frac{Mg}{2}\cos\varphi \Rightarrow 2T = \frac{Mg\cos\varphi}{\sin\varphi}$$

$$\frac{\partial\mathscr{E}}{\partial\ell_i} = 0 \Rightarrow T = \frac{F_\gamma - \frac{1}{2}\frac{EI}{R^2} - \frac{Mg}{2}\sin\varphi}{\cos\varphi}$$

The recorded tension and fibre self-angle are finally given in equation (4.16).

$$\begin{cases} T &= \left(F_\gamma - \frac{1}{2}\frac{EI}{R^2}\right)\cos\varphi \\ \sin\varphi &= \frac{1}{2}\frac{Mg}{F_\gamma - \frac{1}{2}\frac{EI}{R^2}} = \frac{C_{\text{Grav}}}{1 - \frac{2}{\pi^2 C_{\text{Buck}}}} \end{cases} \tag{4.16}$$

The frame effect with an inextensible fibre is thus very different from the frame effect in a drop-on-coilable-fibre system. In our system, the fibre self-angle depends only on the weight of the drop and the local coiling of the fibre.

In order to verify equation (4.16), experiments were performed with a 1.9±0.7 µm diameter TPU fibre and silicone oil droplets. The gravitational coefficient ranges $0.01 < C_{\text{Grav}} < 0.46$. Below 4% the deviation to the straight configuration is negligible. Care was taken to position the drop as close to the center of the fibre as possible. The symmetric tilt of the straight parts of the fibre is a measurable sign of this. Experiments were performed at a speed of 12 µm s^{-1}. No dynamic effect was observed at this speed, as confirmed by the lack of variation when this speed parameter is varied. The position of the drop is followed by the ImageJ particle tracking plugin based on video post-processing at the rate of one image every second. The drop can easily be found by the software through a edge recognition routine and a criteria based on circularity and size. Results are given in figure 4.18.

It should be noticed that the fibre self-angle does not depend on the distance between the clamps. This is to be compared to a normal frame effect with an inextensible fibre. In that case the fibre self-angle is given by $\cos\varphi = \frac{X}{L}$ with X the distance between clamps and L the rest length of the fibre. The fibre thus first follows this equation and falls as if it was inextensible. Indeed at this stage the coiling did not start yet. The system then switches from frame effect with inextensible fibre to frame effect with perfectly extensible fibre. This is reminiscent of the liquid-solid mechanical hybrid nature of the system, as explained in section 3.3.2. This first inextensible-like behavior is different from the windlass mechanism without gravity where the coiling begins directly at the core fibre rest length. Gravity thus induces a delay on windlass activation.
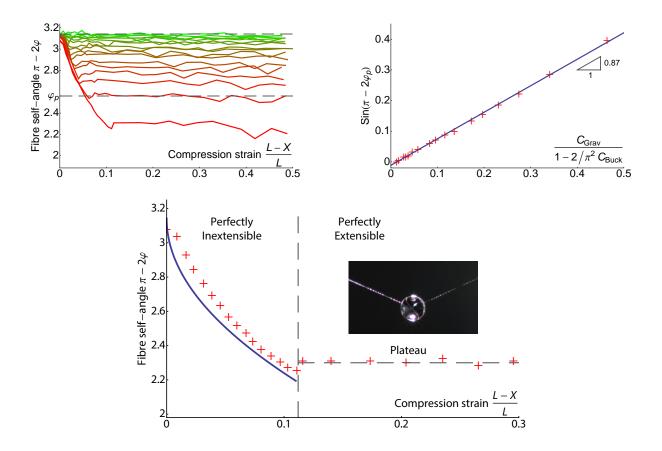
Figure 4.18 – Up left: Fibre self angle $\pi - 2\varphi$ as a function of compression strain for increasing drop size, from green (small) to red (large). Bottom: Inextensible frame effect fall followed by the perfectly extensible frame effect at constant self angle for a large drop ($C_{\text{Grav}} = 0.46$). The solid line corresponds to the theory for inextensible frame effect, followed by a plateau. Up right: The value of the plateau depends only on the weight of the drop and the local coiling of the fibre. This is consistent with a frame effect with a perfectly extensible fibre, as opposed to the classical inextensible fibre.

For ease of calculation, we assume that the coiling begins when the inextensible and extensible self-angles are equal. This is equivalent to neglecting the subcritical retension at first order. According to the experimental results shown in figure 4.18, this is a good approximation. The distance between clamps at coiling activation is then given by equation (4.16) and $\cos\varphi = \frac{L_{\text{ac}}}{L_0}$, which yields

$$L_{\text{ac}} = L_0 \sqrt{1 - \left(\frac{C_{\text{Grav}}}{1 - \frac{2}{\pi^2 C_{\text{Buck}}}} \right)^2} \tag{4.17}$$

with L_0 the rest length of the fibre. As $C_{\text{Buck}} > 1$, we have $0.8 < 1 - \frac{2}{\pi^2 C_{\text{Buck}}} < 1$, which yields a good approximation of the distance between clamps at coiling activation for small gravitational coefficients as $L_{\text{ac}} \approx L_0 \left(1 - \frac{C_{\text{Grav}}^2}{2} \right)$.

Equation (4.16) also gives the sine of the fibre self-angle with a slope of 1. The experimental results yield a value of 0.87 ± 0.03. The discrepancy could be explained by different factors. Some upward convection may exist in the room where the experiments were performed. This was minimized by the use of cold light sources below the sample, but still exists. The fibre bending rigidity outside the drop might not be so negligible at the first order. The weight of the fibre itself may play a role as well.

However, the main factor is thought to be the non-spherical shape of the drop, as the buckling length differs from the drop radius by the meniscii length. This calls for some deeper investigation of the process, which is currently performed.

Nevertheless, the simple connection between geometry and force may still be used as a metrology tool. The experimental results given in figure 4.18 may serve as calibration data so that the fibre self-angle is a measure of the actual absolute force. The measurement of the drop radius and the angle gives a measure of the force through figure 4.18. In the case of small drops, this technique does not allow fine measurement. For a large ($R = 100 \pm 1$ µm radius) drop and a corresponding deviation angle $\varphi = 23° \pm 0.5$, we have a measurement of the force of $F = 100 \pm 3$ nN. This measurement error is excellent and comparable to the performance of the FemtoTools® sensors. However this technique is restricted to heavy droplets only, defined as $C_{\text{Grav}} > 0.05$.

A measure of the plateau fibre self-angle as a function of droplet size can also give access to the fibre bending rigidity EI. The classical technique for such measurement is the study of fibre free vibrations (Landau and Lifchitz, 1967). Imaging micro or even nano fibres at high speed can be extremely challenging. The advantage of our technique is that it is completely static. Additionnally it requires only the measurement of the drop radius, which can be a hundredfold larger than the fibre itself, and thus much easier. And finally the fibre free vibrations frequency is proportional to $\sqrt{EI}$, while the in-drop coiling technique directly measures EI. All these effects add up to make for very fine measurements, better than the classical technique in the case of very thin fibres. It is possible to increase significantly the range of applicability of this technique in term of fibre size, as will be discussed in section 5.5.

Furthermore, at coiling activation the fibre retightens slightly and the fibre self-angle increases. This retension is linked with the subcritical nature of the windlass activation. It is a direct observation of the force undershoot described in section 4.3.2. Multiple retensions also occur on the coiling plateau. In the case where gravity is negligible, they occur with a period corresponding to exactly one additional coil within the drop. In constrat, here they occur quite irregularily. This is discussed in the next section 4.6.3.

4.6.3 Gravity-induced hysteresis

Multiple retensions are observed during fibre coiling when the drop is heavy. However, these fluctuations are erratically spaced, in contrast with the periodic oscillations of the force plateau described in section 4.3.2. The fibre self-angle fluctuations (retensions) thus cannot be explained by a simple force argument. Coiling happens suddenly whenever a retension event occurs. No fibre is additionnally windlassed in between these events, leading to a succession of perfectly inextensible and perfectly extensible frame effects. The coiling of super heavy drops thus happens in a quantified manner. The drops observed with this behavior were characterised by a high gravitational coefficient $C_{\text{Grav}} > 0.5$. They are observed in numerical simulations too, as shown on figure 4.19.

Gravity-induced hysteresis is observed both in experiments and in numerical simulations, with a good qualitative agreement. The experimental data (dotted green line) represent the fibre self angle as a function of the compression strain for a 497 µm silicone oil drop on a 8.3 µm TPU fibre, with a corresponding gravitational coefficient $C_{\text{Grav}} = 0.61$. The compression strain is defined as $\frac{L_0-L}{L_0}$ (see figure 4.17). The numerical simulations were done with corresponding gravitational coefficient $C_{\text{Grav}} = 0.58$ (red) and $C_{\text{Grav}} = 0.50$ (blue). The horizontal dashed line corresponds to a straight fibre ($\varphi = \pi$) and the downward dashed curve corresponds to the inextensible frame effect. This hysteretic behavior corresponds to a barrier followed by a sudden relaxation. The windlass mechanism may be shadowed by this gravity-induced barrier, and may even be deactivated. This will be discussed in the next section.
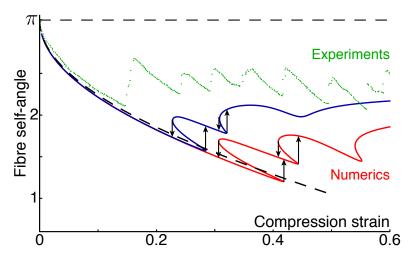
Figure 4.19 – Existence of gravity-induced discontinuous coiling and hysteresis.

4.6.4 Gravity-induced deactivation of the windlass

Equation (4.14) quantifies the distance from coiling threshold in term of forces. $f(R)$ may be viewed as a measurement of the "activity" of the coiling mechanism. In section 4.6.1, setting $f(R) = 0$, we have found the activation threshold and the critical radius of coilable fibre. In the gravitation-free case, $f(R)$ is an increasing function of the drop radius R, but as the weight is considered $f(R)$ is no longer monotonic. The bigger the drop, the easier the coil. In contrast, heavy drops may build up some gravitational tension. This counteracts the windlass mechanism, inherently compressive and leads to a maximum in activity. This most active drop is characterised by a constant gravitational coefficient $C_{\text{grav}} = \sqrt{\frac{2}{11}} \approx 0.43$, as seen in figure 4.21. For drops larger than the most active drop, activity decreases with drop size. It may even reach zero again. This means that gravitational tension is too high for the capillary force to be able to sustain it and coil the fibre at the same time. In practice, this is a gravity-induced deactivation of the windlass, see figure 4.20.
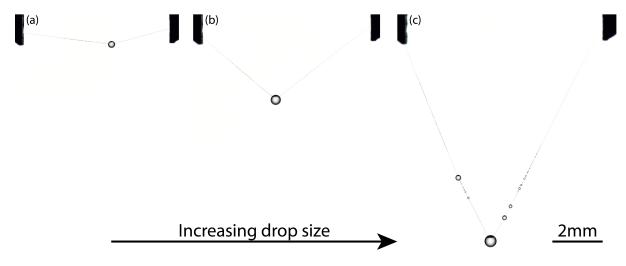

Figure 4.20 – The weight of the drop may produce tension, counteracting the windlass mechanism, inherently compressive. The fibre here is 4.9 μm in diameter and the drops are (a) 275 μm, (b) 394 μm and (c) 481 μm in diameter. The presence of secondary droplets in (c) indicates the absence of coiling of the largest drop.

In the limit $C_{grav} \to 1$, the activity always reaches zero. The windlass is thus always deactivated by gravity when the drop is too big. But this may happen for drops very close in size to the largest sustainable drop. The ultimate difference lies in the size of the fibre used. For small fibres, the deactivation is very close to $C_{grav} = 1$ which makes the influence of gravity almost not noticeable. In the case of large fibres (close to the critical size), gravity changes both the activation threshold and the maximum coiling drop size. Quantitative results using equation (4.14) are given in figure 4.21.
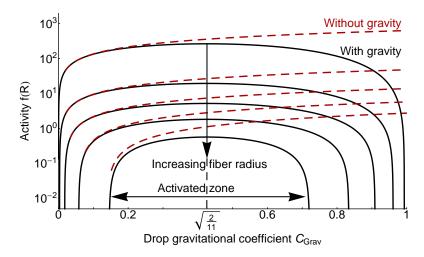

Figure 4.21 – Theoretical activity of droplets as function of droplet size, with and without gravity and for various fibre sizes. The values used for the fibre diameters were 1, 3, 5 ,7 and 9 µm. All other parameters were taken to match the TPU and silicone oil system. Note that the gravity may deactivate the windlass mechanism. This leads to the existence of a most active droplet, as opposed to the non gravitational case where the bigger the droplet, the easier the coil. The gravitational coefficient $C_{grav} = \sqrt{\frac{2}{11}}$ corresponds to the most active drop.

Figure 4.21 shows the strong influence of gravity on the system. Instead of a simple activation threshold without gravity, an upper bound may exist with gravity and lead to the apparition of an activated zone. The activity of the windlass mechanism is also decreased by gravity. For small droplets ($C_{grav} < 30\%$), the difference goes unnoticed though. The smallest drop of figure 4.20, which gravitational coefficient is $C_{grav} = 0.17$, has an activity of 3.8±0.2 in the gravity-free case and 3.6±0.2 with gravity. However, for larger drops, the behavior of the system can be completely changed by the influence of gravity. This explains the deactivation observed in figure 4.20, where the largest drop, $C_{grav} = 0.92$, would have a gravity-free activity of 13.6±3 (strong coiling), whereas with gravity its activity becomes - 0.1±0.2, which means that the coiling is deactivated. One may think of placing the system is a dense immiscible liquid environment to let Archimede's force override gravity and reactivate the windlass. This will be further discussed in section 5.5.

Spider windlass strategy may be reanalysed in the light of this result. An array of multiple droplets has several advantages. Glue droplets distribution increases the actual contact area during insect entrapment. On the other hand, localised large drop may increase windlass ability, but increases also gravitational tension. Multiple droplets decrease the influence of gravity by spreading weight distribution as well as increasing the number of capillary meniscii. It thus minimizes the fibre self-angle as seen in section 4.6.2, which is key to sustaining web integrity.

Another advantage of weight spreading lies in the dynamics of the system. The smaller the drop, the faster the response time. This is discussed in the next section.

4.7 Insight into the dynamical behavior

The drop needs a certain time to coil the fibre in when compression occurs. This can be seen as the response time of the drop-on-coilable-fibre system. When the sample is compressed (resp. stretched) faster than its response time, coiling (resp. uncoiling) is prevented. The sample will thus behave as an inextensible fibre system. There shows an equivalence between a drop-on-coilable-fibre under fast compression (resp. stretching) and the effects of gravity. Indeed when an initially straight fibre is quickly compressed below its rest length, a inextensible frame effect is observed, even for the smallest droplets. If the tensile test is stopped however, the sample relaxes and finally reaches its static equilibrium frame effect angle.

Using this analogy, equation (4.16) can be further exploited to derive the dynamics of the system in this configuration. An instantaneous compression or extension is equivalent to imposing an initial fibre self-angle different from its equivalent value. The resulting vertical force in that case is

$$F_z = 2\left(F_\gamma - \frac{1}{2}\frac{EI}{R^2}\right)\sin\varphi - Mg = 2\left(F_\gamma - \frac{1}{2}\frac{EI}{R^2}\right)(\sin\varphi - \sin\varphi_{eq})$$

With φ_{eq} the equilibrium value of φ, given in equation (4.16). The vertical position z of the drop is given by $z = -\frac{L}{2}\tan\varphi$ with L the total length in between the clamps. Upon using Newton's second law, the fibre self angle dynamics is given by

$$-M\frac{L}{2}\frac{d^2\tan\varphi}{dt^2} = 2\left(F_\gamma - \frac{1}{2}\frac{EI}{R^2}\right)(\sin\varphi - \sin\varphi_{eq})$$

This general equation does not have a simple solution. However it is possible to find one for vibrations in the vicinity of the equilibrium value φ_{eq}. Indeed for $\Delta\varphi = \varphi - \varphi_{eq} \ll 1$, we have $\tan\varphi \approx \tan\varphi_{eq} + \frac{\Delta\varphi}{\cos^2\varphi_{eq}}$ and $\sin\varphi \approx \sin\varphi_{eq} + \Delta\varphi\cos\varphi_{eq}$, which leads to

$$\frac{d^2\Delta\varphi}{dt^2} = -4\frac{F_\gamma - \frac{1}{2}\frac{EI}{R^2}}{ML}\cos^3\varphi_{eq}\,\Delta\varphi$$

$$\Delta\varphi(t) = \Delta\varphi(t=0)\cos\left(\frac{t}{\tau}\right) \tag{4.18}$$

$$\text{With } \tau = \sqrt{\frac{ML}{4\left(F_\gamma - \frac{1}{2}\frac{EI}{R^2}\right)\cos^3\varphi_{eq}}} \text{ and } \sin\varphi_{eq} = \frac{Mg}{2\left(F_\gamma - \frac{1}{2}\frac{EI}{R^2}\right)}$$

The perturbed drop-on-coilable-fibre system thus behaves like an oscillator with a typical response time τ given in equation (4.18). Without gravity ($\cos\varphi_{eq} = 1$), this response time $\tau_{g=0}$ (given in equation (4.19)) represents an inertial time. This is the time the droplet needs for dragging itself back to its original position through capillary force along the fibre. In the case of inextensible fibre, the system would be in free fall, with a typical time $\tau_f = \sqrt{\frac{L}{g}}$. It is possible to rewrite the response time τ as a function of these two times as

$$\tau = \frac{\tau_{g=0}}{\left(1 - 4\left(\frac{\tau_{g=0}}{\tau_f}\right)^4\right)^{3/4}} \text{ with } \tau_{g=0} = \sqrt{\frac{ML}{4\left(F_\gamma - 2\frac{EI}{R^2}\right)}} \text{ and } \tau_f = \sqrt{\frac{L}{g}} \tag{4.19}$$

In the case where the influence of gravity is neglectible ($C_{\text{Grav}} \ll 1$), the system buckles at high speed (it does not have time to coil) and then would retightens with an inertial time $\tau_{g=0}$.

Unfortunately, this is not well verified in practice. Self-angle relaxations after 10% compression at $1\,\mathrm{cm\,s^{-1}}$ have been measured with a video camera at 30 frames per second. For a 1.9 microns diameter fibre, the response time of a 241 μm droplet is 150 ± 20 ms instead of 19 ms and the response time of a 96 μm droplet is 40 ± 20 ms instead of 4.5 ms. The relaxations of the largest droplet are shown on figure 4.22.
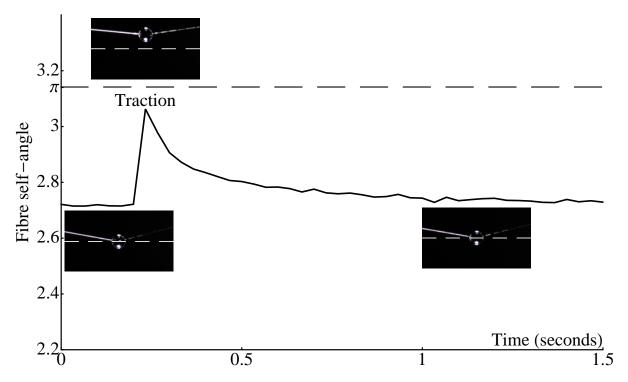

Figure 4.22 – Response of a drop-on-coilable-fibre system to instantaneous compression or traction. The TPU fibre here has a diameter of 1.9μm and the silicone oil drop has a diameter of 241 μm. An instantaneous view of the system is given in the insets. On each inset, the dashed line represents the initial position of the droplet and serves as a guide for the eye. The main dashed line is at $\varphi = \pi$ and represents a straight fibre.

Several parameters may explain the discrepancy. Local rearrangement time may be different from global rearrangement time (which corresponds to the response time) and affect the overall dynamics. In addition, no oscillation have been observed, only deceleration. This means that damping plays an important role. It may come from the viscosity of the fluid and of the inner matrix of the solid fibre. As viscous silicone oil is used here (1000 times more viscous than water), we propose than it may be the main source of discrepancy in our case. This would explain the exponential behavior of the relaxation as well. This calls for further investigation of the subtilities of the windlass mechanism.

In the next chapter, we show that the elasto-capillary windlass mechanism can be extended in numerous ways to produce innovative and unconventional technological perspectives.

CHAPTER 5

EXTENSION OF THE STUDY AND CONCLUSION

"The true artist is quite rational as well as imaginative and knows what he is doing; if he does not, his art suffers. The true scientist is quite imaginative as well as rational, and sometimes leaps to solutions where reason can follow only slowly; if he does not, his science suffers." — Isaac Asimov, The Roving Mind

Contents

THIS chapter presents ideas to open future academic and technological potential of the windlass mechanism. The use of new parameters such as the number of fibres, temperature, the external fluid density,... brings some extra freedom to explore the possibilities of this phenomenon. Although much work is needed to clarify subtilities in the even more complex cases presented, it shows proofs of concept for interesting ideas. It was also the occasion to build some interesting collaborations with other labs in the surroundings of University Pierre and Marie Curie.

5.1 Technological implications

Buckling has been used in literature to induce an apparent extensibility to materials that are not originally stretchable. This comes from a geometrical perspective, as explained in section 1.4.2. Effective extensibility is built up by leaving some "loose length" through buckling (see figure 5.1), so that when the sample is put under tension, the buckled structure first retightens then stretches. The buckling technique is particularly used in the field of stretchable electronics, reaching extensibilities of tens of %. With the windlass mechanism, extensibilities several orders of magnitude higher are on the brink of being achieved.
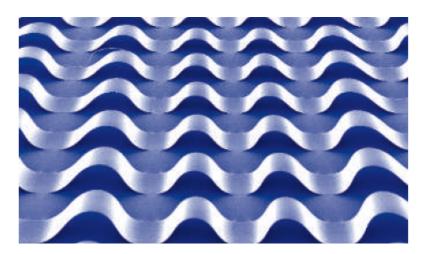
Figure 5.1 – Buckling is useful to induce an apparent extensibility from a geometrical perspective to materials that are not naturally stretchable. This lead to the birth of the field of stretchable electronics. Source: Rogers et al. (2010).

Although windlass-enhanced electronics is a reasonable application, practical solutions for such realisation do not come easy. In the next section, we present ways of upscaling the drop-on-coilable-fibre systems, as well as achieving the fundamental brick for multidimensionnal windlassing structures. We also aim to build actuators and come up with unconventional microfabrication techniques. This shows the windlass mechanism as an innovative and counter-intuitive system.

5.2 Multi-fibres windlass

5.2.1 Bundle of fibres in a single droplet

In the previous chapters, only one fibre has been coiled within liquid droplets. Using multiple fibres is useful in many ways. Multiple fibres means multiple capillary meniscii, thus a higher capillary force. This can be used for instance to build up a powerful capillary motor or to upscale the windlass mechanism.

Indeed, consider a bundle of radius r_0 made of N equivalent fibres. Reasoning on equivalent section, each fibre has a radius $r = \frac{r_0}{\sqrt{N}}$. Thus the bending rigidity of the bundle is $EI_N = NE\frac{\pi}{4}\left(\frac{r_0}{\sqrt{N}}\right)^4 = \frac{EI_0}{N}$. The index N refers to the N fibres case, while the index 0 refers the single fibre case. It means that the bending rigidity of a bundle made of N fibres is N times smaller than a fibre of similar section. The capillary force for a bundle of N fibres is higher than for a single fibre of similar section. Indeed $F_{\gamma,N} = N2\pi\gamma r\cos\theta_Y = \sqrt{N}F_{\gamma,0}$ with $r = \frac{r_0}{\sqrt{N}}$. This is with the assumption that fibres are well separated in the bundle. The bundle can then be assimilated to a porous fibre where the liquid may creep and create a liquid interface N times larger than for a fibre of similar section.

Balance with the weight of the drop sustained by the bundle yields the maximum drop radius as $R_{\mathrm{max},N} = N^{1/6}R_{\mathrm{max},0}$, with $R_{\mathrm{max},0}$ the radius of the largest sustainable drop on a single fibre of similar cross section. Additionnally, in case of heavy drops, the angle between the rotated meniscii and the straight fibre (defined in section 4.6) is $\sin\alpha_N = \frac{\sin\alpha_0}{\sqrt{N}}$. Adding up those differents effects yields to new critical radius of coilable bundle:

$$r_{\mathrm{crit},N} = r_{\mathrm{crit},0}\, N^{11/14} \tag{5.1}$$

This shows the upscaling possibility of a bundle of coilable fibres. We applied this ideas to two

different types of materials, a special silk filament made of hundreds of nano-fibres (ecribellate capture silk, described in appendix A) and electrospinned fibres. A different approach to provide a way towards the upscaling of the system is presented in section 5.5.

Electrospinning   Electrospinning is a very useful technique to create nano-fibres (Greiner and Wendorff, 2007). The desired material is dissolved in a volatile solvent and a droplet of the mixture is created at the tip of a nozzle connected to a syringe pump. A high electric voltage (10 to 30 kV) is applied to the droplet to charge it up. It has been explained that electric charges act against surface tension in section 1.4.3. When the minimization of the liquid interface cannot resist Coulombic repulsion between the electrical charges any more, the drop adopts a sharp shape with a tip, called a Taylor cone (Taylor, 1969). This cone further destabilizes and produces a very thin jet.

The jet is directed towards a earthed deposition metallic target (the collector) acting as a counter-electrode. During the travel, the jet evaporates very quickly due to high surface to volume ratio linked to its thinness (see section 3.3.1). This leaves even thinner solid fibres of the desired material, down to the nanoscale. Furthermore, the instability sends the jet at several meters per second. That is an efficient way of creating a large amount of nano fibres.
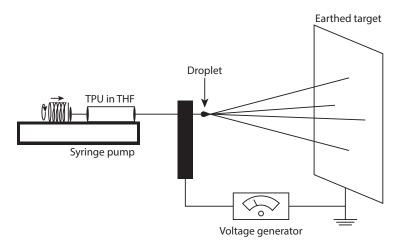

Figure 5.2 – Sketch of the process of electrospinning. This produces nanofibres at a speed of meters per second.

In collaboration with Natacha Krins (LCMP, Collège de France and CNRS), electrospinned fibres have been prepared. We used the block copolymer PVDF-HFP, which consists of a mixture of PolyVinyli-Dene Fluoride and PolyHexaFluoroPropylene. This material is soft and can be dissolved in THF, which has good evaporating properties as a solvent. The tip to collector distance is taken large enough so that all evaporation occurs in the air, thus producing thinner fibres. In practice, this distance is set to 30 cm. Unfortunately, due to whipping instability during flight and details in the evaporation process (Greiner and Wendorff, 2007), the fibres are deposited in random directions and have an wide size distribution. However, the directionality of the fibre networks can be tuned by taking a bundle of fibres and slightly stretch it before clamping. The wide size distribution is not such a problem as long as the biggest fibres can be coiled. After silicone oil deposition, the bundle is collapsed and coiling of the entire bundle is observed (see figure 5.3).

Further characterization is needed to understand quantitatively the drop-on-coilable-bundle system. Another interesting problem that shows the richness of multiple fibres systems is the case of crossed
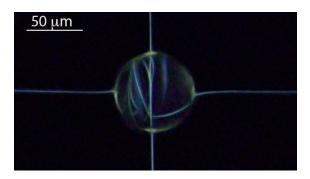
Figure 5.3 – A bundle made from electrospinned block copolymer PVDF-HFP fibres (left) can be coiled within a silicone oil droplet (right). The nature and heterogeneity of the fibre bundle makes observation difficult.

fibres.

5.2.2 Crossed fibres, towards a bidimensionnal windlass

Here we study the configurations of two perpendicular fibres coiled within the same droplet. There is freedom to coil only one at a time, or both simultaneously. In the case where one fibre is kept straight, its presence influences the coiling of the other fibre: the coiled fibre coils in a half sphere, as the path towards the other half sphere is blocked, see figure 5.4.
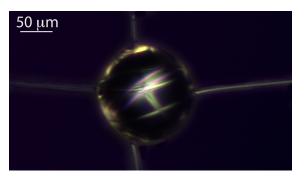

Figure 5.4 – Two perpendicular Thermosplastic PolyUrethane fibres are held perpendicular. A silicone oil droplet is deposited at the contact point of the fibres. Left: Single coiling (one fibre is kept straight) happens in an half sphere, here the left part, the other half sphere being forbidden sterically by the presence of the perpendicular straight fibre. Right: Simultaneous coiling is also possible, and leads to complex crossed bi-coiling.

The straight fibre may be used to prevent the sample from sagging, allowing easier study of the coiling in the case of heavy drops for instance. The proper study of the coiling mechanism of two crossed fibres is a beautiful problem that requires further extensive work.

However, this is the first step towards the generalization of the windlass mechanism to bidimension-nal and tridimensionnal structures. While a sheet can be wrapped around a droplet in an origami fashion (as described in section 1.4.4), it lacks the freedom of coiling several times around the droplet. If many fibres were laid around a central cross point, the droplet could coil the apparent 2D sheet much further.

Furthermore, a 2D array of perpendicular fibres with drops at the joints is an efficient way to design a foldable bidimensionnal device. However, under very high compression strain, droplets may coalesce and leave some joints free of liquid interface thereafter. Current work focuses on finding ways of pre-serving the integrity of such a structure. This could be done by adding some surfactant to the droplets,

rigidifying the interface and increasing the contact time needed for coalescence (Hodgson and Lee, 1969). The effect is so intense that it can be seen in our everyday life. While a drop of water quickly merges with a water bath, coffee droplets may stay for seconds on the surface of a coffee cup, as they are charged with tasty surfactants. This has also the effect of protecting effectively the system against external shocks, thus increasing the lifetime of the device.

Another interesting property of surfactants is the possibility of influencing them by use of temperature or light. On-demand activation is even possible for well chosen configurations. This is further discussed in the next section.
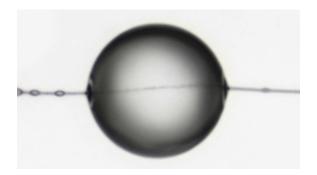
5.3 On-demand activation

In this section, we show that it is possible to activate the windlass mechanism on-demand, by changing the properties of the fibre and/or of the droplet through the activation threshold. This allows the user to switch from a normal drop-on-(straight)-fibre system to a drop-on-(coiled)-fibre system at will, thus tuning finely the desired mechanical properties. This could be done by use of intense light flux, electric fields (in connection to figure 1.15), temperature or change of environment. Here we focus on the last two parameters for proof of concepts.

5.3.1 Glass transition

Temperature may influence solid materials in different ways. While the main visible influence is the melting of the material, many other effects are also powerful. While higher temperature soften common solids slightly, some materials may experience sudden drop in rigidity of a typical thousandfold at a specific temperature. This is due to the glass-rubber transition (Van Krevelen and Te Nijenhuis, 2009).

The glass transition is a reversible transition in amorphous materials from a hard and relatively brittle state into a molten or rubber-like state. An amorphous solid that exhibits a glass transition is called a glass. Glass is actually a kinetically locked state that resembles a supercooled liquid, but with a viscosity as high as 10^{12} Pa.s (Zarzycki, 1991). For reference, this is one trillion times more viscous than honey. In practice, this gives the glassy state mechanical properties similar to the crystalline phase. Above the so-called glass transition temperature, the glassy state is unstable and the sample becomes soft and rubbery. Here we used PolyLactic Acid, as it is a thermoplastic (hence easy to mold into thin fibres) that has a glass transition temperature of 60°C. Its Young's modulus is 2 GPa at room temperature, while it decreases down to 4 MPa at 80°C. The thousandfold decrease in rigidity means that the windlass activation threshold can easily be gone through by use of temperature.
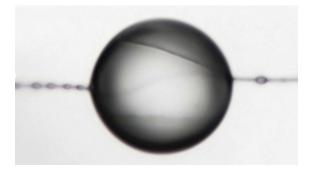

Figure 5.5 – On-demand activation of the windlass mechanism through glass transition. Proof of concept experiment with a 211 μm silicone oil droplet on a 3.9 μm PolyLactic Acid fibre. At room temperature, the fibre is rigid and stays straight (left), whereas at 80°C it becomes soft enough to get coiled (right).

This can be used as an actuator or a temperature sensor, as well as an effective way of tuning the mechanical properties of the system. Another way to do so is to change the wetting properties of the droplet through the threshold.

5.3.2 Chemical environnement change

Appendix B.1 shows that while glycerol does not wet TPU nor PLA, adding a slight amount of ethanol to glycerol influences its wetting properties. The surface tension of glycerol/ethanol is lower than glycerol alone, as $\gamma_{\text{glycerol}} = 62$ mN m^{-1} and $\gamma_{\text{ethanol}} = 22.1$ mN m^{-1} (Good and Elbing, 1970), and the surface tension of the mixture is somewhere in between these values. Albeit this effect might be strong, this also influences the contact angle between the drop and the fibre. In this regard, ethanol wets TPU quite well with a recorded contact angle of $20 \pm 3°$. The method for proper measurement of the contact angle is given in appendix B.1.

In our specific case of glycerol on TPU, both effects add up to make the final capillary force $\gamma \cos \theta_Y$ actually higher with a pinch of ethanol than without. This means that the windlass activation threshold might be crossed by adding some traces of ethanol in the system. Figure 5.6 shows that it is possible to activate the windlass mechanism by simply placing the glycerol-on-TPU system in an ethanol rich atmosphere.
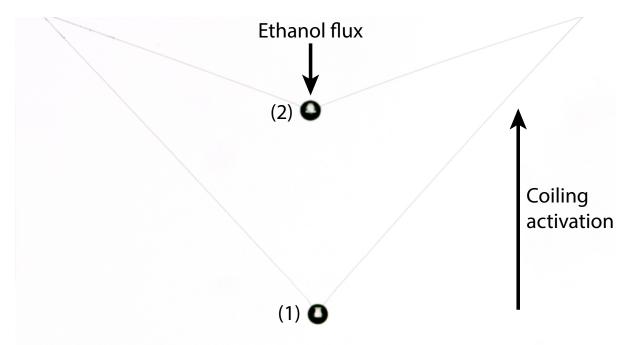
Figure 5.6 – Glycerol does not coil TPU due to poor wetting properties. Hence a glycerol droplet on a TPU fibre hangs low under compression, see configuration (1). However, adding a small amount of ethanol changes the effective wetting properties and activates the coiling mechanism (configuration (2)), even against the incoming flow of ethanol and gravity. Source: Paul Grandgeorge.

Experiments shown on figure 5.6 have been performed by Paul Grandgeorge, the PhD student who will take the windlass mechanism project further for the next three years. This shows the possibility of using the drop-on-coilable-fibre system as a chemical sensor, and will be further developed as such in future work.

5.4 Coiling new materials

5.4.1 Metallized TPU

Here we present a method to build conductive micro-coils. We use a core fibre of Thermoplastic PolyUrethane and deposit a 20 nm layer of gold by sputtering. Sputter deposition is a physical vapor deposition (PVD) method of thin film deposition. This involves ejecting material from a "target" that is a source onto a "substrate" such as a silicon wafer. The ejection is done by sending charged Argon molecules (the sputtering gas) onto a target made of the material to be deposited (gold here). It generates a plasma that will further impact the substrate and create a thin layer of gold.

This was done in collaboration with Diego Baresch at the Institut des NanoSciences de Paris. The resistance of the prepared fibres was tested using a regular multimetre, and found to be on the order of a few hundreds of kΩ. This is higher than expected from the intrinsic conductivity of gold and might mean that the layer cracked during manipulation of the stretchable TPU core fibre. It nevertheless conducts electricity, and can be coiled within a liquid droplet. In order to be able to conduct electricity through the fibre without damage, the liquid must be chosen non-ionic to avoid short-circuits. Here we used a silicon-based polymer that resembles the silicone oil tested in the previous experiments and allows coiling. After 90 minutes, it cures in open air, solidifies and blocks the coiling in place for ease of manipulation and to avoid undesired electrowetting (see figure 1.15). The resulting permanent microcoil is shown on figure 5.7.
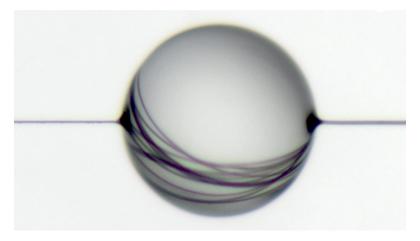

Figure 5.7 – A 20 nm gold layer is deposited on a TPU fibre with a diameter of 5.0μm. The coated fibre then coils within a 318 μm drop of silicon-based polymer, that further solidifies by curing. This produces a stable micro-coil that conducts electricity.

The produced magnetic field were tested using a Hall effect transducer from Vernier[®]. This magnetic field sensor has a good sensitivity of 4 μT. But due to the high resistivity and the small size of the gold layer, no significant measurements were achieved. Furthermore, the difficulty to probe the direction of the axis of the coil (and thus of the magnetic field) is an important issue we wish to address in future work. Another method to produce micro-coils is presented in section 5.6 and is based on evaporation.

5.4.2 Glass nanofibres

In collaboration with Baptiste Gouraud from Laboratoire Kastler Brossel, we present here the elastocapillary coiling of glass nanofibres. Laboratoire Kastler Brossel is a quantum optics laboratory in Univer-

sity Pierre and Marie Curie where single atom trapping experiments require the use of glass nanofibres. These nanofibres are made from commercial optical fibres. These optical fibres possess a cladding layer, as well as an additional protective layer. The cladding layer is a low refraction index medium, used to improve efficiency of the optical fibre waveguide. The initial fibre is 400 μm in diameter, but the raw core glass fibre is only 30 μm. The protective coating and cladding layer are removed with an optical fibre stripper, which resembles a typical electric cable stripper. The fibre is wiped with a Kimtech tissue soaked with isopropanol to remove any residue.

The usual method to draw very thin glass fibres from larger one is to stretch them while heating. The basis of textile-grade glass fibres is silica, SiO_2. In its pure form it exists as a polymer, $(SiO_2)_n$. It has no true melting point but softens up to 1200°C, where it begins to degrade. As viscosity of the glass must be as low as possible to ensure large strain without break, we aim to reach this limit temperature before stretching the fibre. We use an oxyhydrogen (2:1 O_2 and H_2 molecules) blowpipe to warm a central portion of the fibre up to 1200°C. In addition to the possibility of reaching such high tempera- ture, oxyhydrogen is clean and leaves no soot, water being the only product of combustion. The nozzle of the blowpipe is adjusted at the right distance from the fibre to reach the required temperature. The fibre is oscillated horizontally above the flame to avoid overheating and degradation. The oscillations are made over a 2 cm length at $1\,\mathrm{cm\,s^{-1}}$. Additionnally, the fibre is stretched at $25\,\mathrm{\mu m\,s^{-1}}$. The process takes roughly 5 minutes to reach the required fibre diametre of 350 nm. This method as well as the optimization of the drawing parameters were implemented by Baptiste Gouraud. This method produces extremely thin glass fibres as shown on figure 5.8.
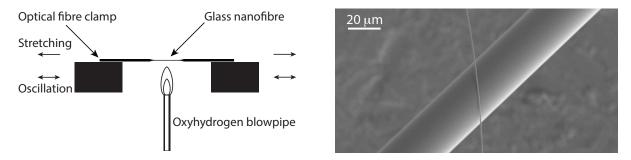

Figure 5.8 – Sketch of the drawing method to produce glass nanofibres down to 350 nm in diameter (left) and image of the resulting suspended nanofibres (right) along with an original optical fibre (30 μm in diameter) observed under electronic microscopy under 5 kV and a magnification of 630×.

One glass nanofibre was taken from the drawing setup by gently touching the large part of the fibre with caliper forks. We use a glue that cures under UV light to clamp the fibre further in a controlled manner. Silicone oil is a liquid of choice to coil glass fibres as it wets them well with a measured contact angle of 8±5°. Brushing the fibres with high viscosity silicone oil unfortunately breaks them. Low vis- cosity silicone oil (20 times that of water) is thus sprayed over the glass fibre using the method described in section 3.3.1. The fibre is then slightly collapsed, and local coiling of the glass nanofibre is observed, as depicted in figure 5.9.

This shows the universal potential of the windlass mechanism to coil fibres, although some material such as glass might be constraining to manufacture at such small size. A method to upscale the range of the windlass mechanism has been explained in section 5.2 and uses multiple fibres, but that does not address the manufacturing problem. In order to do so, the next section presents a method based on buoyancy to increase the critical radius of a coilable single fibre.
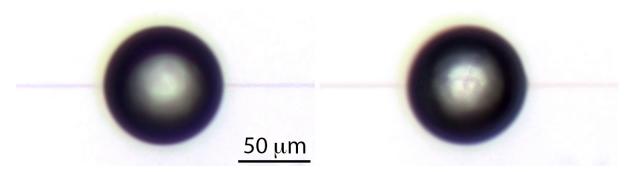
Figure 5.9 – Left: A silicone oil droplet sits on glass nano-fibre (below 350 nm diameter). Right: When the fibre is collapsed, the curvature of the glass fibre localizes inside the drop through the elastocapillary windlass mechanism. The green halo is due to diffraction.

5.5 Macro-windlass

In section 1.5, we explained that the critical coilable fibre radius is influenced by the gravitational field, as there is a maximum drop weight that the fibre can sustain through capillary forces. An interesting and quite straightforward way to upscale drop-on-coilable-fibre systems is to counteract gravity by use of Archimede's forces. Placing the system in a dense fluid provide such a possibility. Of course, the external liquid and the liquid droplet must be immiscible. The gravito-capillary length $\ell_c = \sqrt{\frac{\gamma}{\rho g}}$ may be increased dramatically as the density of the droplet ρ is replaced by the density contrast $\Delta \rho = \rho - \rho_{\text{ext}}$, with ρ_{ext} the density of the environment. It means that centimetric droplets may be stabilized in a dense fluid, which is impossible in air. A proper matching of the external fluid density is possible through mixture. For instance, an ethanol/water mixture (both immiscible with the silicone oil of the droplet) may match the density of the droplet. A 26 % in weight of ethanol in water matches the 960 kg m^{-3} density of silicone oil. However, due to solution instability against convection and evaporation, keeping a perfect match is a complex task.

Another effect of a liquid environmenent is that it changes the wetting properties of the drop. The use of a non-wetting liquid (with respect to the fibre) as an external liquid decreases the contact angle of the drop and actually increases the effective surface tension of the liquid. For instance, using a silicone oil droplet in a water environement (which does not wet our plastic fibres) decreases the contact angle down to practically zero and increases the surface tension from 21 to 43 mN m^{-1} (Good and Elbing, 1970; Kanellopoulos and Owen, 1971). All in all, the addition of all those effects allows a dramatic upscaling of the critical fibre radius. As a proof of concept, figure 5.10 shows a thick fibre being coiled in a macroscopic droplet.

Experiments shown on figure 5.10 have been performed by Paul Grandgeorge, the PhD student who will take the windlass mechanism project further for the next three years. In figure 5.10 we used a silicon-based polymer (reference RTV3535 from Esprit Composite, with a Young's modulus of 1.3 MPa) with a silicone oil droplet. Due to the proximity in chemical structure of the fibre and droplet, the contact angle is almost zero. However, this might be a sign of imbibition. This has been checked as an attempt to measure increase of fibre volume as well as drop volume decrease. But no effect has been observed whatsoever, which means that we can neglect the imbibition issue here confidently.

Applying curvature to macroscopic fibres in a dense liquid has previously been achieved by Roman and Bico (2010). Albeit looking similar, they used a fibre free at one end. This slight difference changes profoundly the problem, as the buckling state is different. The retightening effect, the unique

Figure 5.10 – A 2.7 mm silicone oil droplet coils a 140 µm polymeric fibre. A dense environment (water) is an effective way of upscaling the coilable fibre systems by use of Archimede's forces. Source: Paul Grandgeorge.

force profile and the liquid-solid force hybridation are specific to the windlass mechanism.

This technique is very useful as it allows upscaling of our system with a simple method: simply put the drop-on-fibre system in an immiscible liquid. And in addition, the closest the densities of the liquids, the more powerful the upscaling possibility. Some rigid materials have a critical radius of coilable fibre of only a few hundreds of nanometers, which is difficult to manufacture, as seen in section 5.4. This technique can prove valuable to facilitate the fabrication process of windlassing devices using these rigid materials.

5.6 Microfabrication

5.6.1 Microtangles

Pugno (2014) put forward that the simple introduction of a frictional element can increase the toughness of a material, and experimentally demonstrated such an idea, measuring an almost hundredfold increase. This could explain the mysterious abundance of tangle formations in spite of their incremental energy cost and topological difficulty, in biological evolved structures, such as DNA strands and proteins (Pugno, 2014).

When constrained to high level of packing (typically one hundred coils inside our silicone oil droplet-on-TPU-fibre system), the proper rearrangement of the fibre might be problematic because of steric barriers as well as build up of self-contact stresses. This may leave us with a coiling that is stuck by solid friction. The fibre is still able to uncoil, but requires a higher amount of energy, even in the quasi-static regime. This coulomb frictional component thus adds up to the toughness of the fibre. Interestingly, such a structure does not need the presence of the droplet any longer to be sustained. It is thus possible to "dry" the sample by gently touching the droplet with tissue and recover a simple fibre system, but with the additional presence of an entangled structure, as shown on figure 5.11. A contour length of 22 mm of a 4.5 µm diameter fibre was collapsed into a droplet of initial diameter of 163 µm to make this sample.

The exhaustive characterisation of these tangled structures are currently under work, and show premises to increase the measured thoughness of our samples. The force-displacement curve should resemble the one observed for drop-on-coilable-fibre systems qualitatively at first order (shown in section 3.3.2). Indeed, the sliding of the frictional tangle should occur at constant force, which depends on the self-friction coefficient. This should lead to a force plateau much like the one observed during capillary uncoiling of the coiled fibre, but at much higher forces. When the tangle is completely undone,
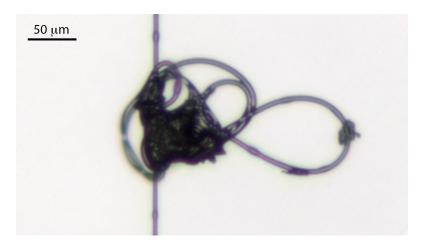
Figure 5.11 – Microtangle made by extreme coiling and extraction of the droplet.

the system enters the elastic regime. The main difference between the drop-on-coilable-fibre systems and tangled-fibre structures is the irreversibility of the latter. One cannot collapse the fibre back into a tangle without going through the process of drop deposition, high level of capillary coiling, and drop removal.

5.6.2 Micro-coils

As explained in section 4.3, if a coiling drop evaporates down to the deactivation radius, the fibre is expected to completely uncoil and recover the classical drop-on-fibre shape. Instead, we observe a structural instability, leading to complex tridimensionnal regular patterns that could be very useful in microfabrication. Here we use an ethanol droplet (stabilized in a saturated atmosphere) to coil a TPU fibre. The sample is then let free to evaporate by slowly decreasing the ethanol vapor pressure through adjustment of the mist flow (see section 2.2.2). As the drop evaporates, the inner fibre coiling is compressed inwards and rearranges in a very ordered manner. When the deactivation radius of the fibre is reached, the drop keeps on evaporating, but without squeezing the droplet. Instead, it evaporates preferantially in the direction of the axis of the coil with a pinned contact line on the external fibre, resulting in a pancake-shaped drop. Upon further evaporation, the fibre coiling constitutes a frame on which a thin film of ethanol exists, until pinching eventually occurs. Some non-volatile residues still attach to the fibre, creating an actual toroidal coiling sustained by capillarity, as depicted in figure 5.12.
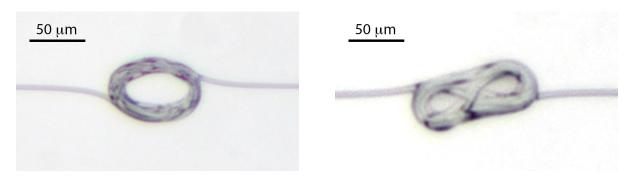

Figure 5.12 – Toroidal and lemniscate-shaped coilings obtained by evaporation of a windlassed droplet. The inner radius of the tore is equal to the deactivation radius defined in equation (3.3). This may be used for unconventional microfabrication techniques.

It is worth mentioning that the equilibrium inner radius of the coil is 71 µm, which is very close to the deactivation radius, which in this specific case is $R_{\text{deac}} = 66$ µm (see equation (3.3)). Figure 5.12 also shows a 8-shaped equilibrium coiling. Higher-symmetry coilings have also been observed. The regulation of the final shape might be due to some residual torsion within the fibre. However, prediction of the shape might require an exhaustive detailed study of this complex non-linear case.

5.7   Conclusion

In this PhD work, we have shown that the combination of the right fibre and the right droplet leads to an impressive diversity and richness of interactions, such as configurations where a droplet is able to coil the fibre on which it sits, phenomenon called elasto-capillary windlass. Through work on natural samples, we have shown that the windlass mechanism is indeed possible, and is furthermore present in spider capture silk, which consists of a silk core fibre coated with glue droplets. The presence of capillary forces provides tension to the whole sample during coiling, and allows preservation of web structural integrity. The mechanical behaviour of spider capture silk can be described as a liquid-solid mechanical hybrid, where the behavior below core fibre rest length is that of a liquid, whereas above this rest length it is that of a solid. This unique behaviour also has implications in spider web damping properties, which are crucial to the ultimate efficiency of the web as a food trap.

We have further shown that the elasto-capillary windlass mechanism can be explained by a phase transition formalism, where a given drop-on-coilable-fibre sample is described as a mixture of a coiled wet phase and a dry straight phase. The fact that surface energy can be transferred into bending energy leads to the possibility of existence of such phases, although only under certain conditions. The fibre must be thin enough and soft enough to be coiled within a sufficiently large and wetting droplet. This restricts realisation of the windlass mechanism to the micro- and nano-world. Nevertheless, we have shown that it is indeed possible to create a completely artificial version of drop-on-coilable-fibre systems with virtually any material, inspired by the observation of spider capture silk. The inherent mechanical nature of this phenomenon reveals its universality. The mechanical properties of spider silk thus come from two different sources: the complex specific biochemical proteins for the properties in tension, and the universal elastocapillary windlass for the properties in compression.

The design of artificial drop-on-coilable-fibre systems further gave us the opportunity to study in fine details these systems. We have shown that a simple balance between the capillary compressive force and the local critical buckling force explains the transtition to coiling activation. The subtle mechanics of this structure problem implies a subcritical transition, indicated by an initial negative stiffness regime as well as a dependency on previous sample history. Further into the post-buckling regime, in-drop fibre coiling organizes into complex forms, which may be disordered and occupy all the available drop space, or alternatively be ordered and well organized. The actual shape of the drop envelope is of importance in the determination of the coiling arrangement, as showed by the strong link between morphology and drop deformation. We have also observed the influence of gravity: whenever a drop is too heavy, the capillary forces are not sufficient to keep the entire sample straight. The system then adopts a triangular shape where the drop is pulled downward by gravity. Analysis of the angle between the two straight parts of the outer-drop fibre showed good agreement with the picture of rotating meniscii that accomodate the drop weight. This angle is related to the force profile of the drop-on-coilable-fibre system, and may thus serve as an optical fine metrology tool.

We further showed that the drop-on-coilable-fibre systems can be enriched by the addition of new degrees of freedom, such as using several fibres, temperature changes or evaporation. This led to the design of actuators and sensors, as well as a new technique for 3D microfabrication, showing the potential of increasingly complex cases of drop-on-coilable-fibre systems, both technologically and academically.

DIFFERENT KINDS OF CAPTURE THREADS

A.1 Cribellate versus ecribellate

In the previous chapters, we described the importance of capture silk as an effective trap for the spider's preys. We focused on the ecribellate capture silk, that consists of gluey droplets on a silk thread. But there is actually a second type of capture silk, evolutionnarily older: the cribellate silk. From the macroscopic point of view, both webs have a similar architecture, see figure A.1 insets A and B. However, the capture silk threads are very different: the ecribellate silk uses wet adhesion through its gluey liquid droplets, while cribellate silk uses the dry adhesion of highly puffed nanofibres, see insets C and D. Ecribellate capture threads are spun by a double spinneret, see inset E. The one connected to the flagelliform silk gland (FL) that spins the core silk thread and the one connected to the aggregate gland (AG) that produces the gluey liquid coating. Cribellate silk is very different. Its puffy morphology comes from the specific spinning process (Opell, 1993, 1994). During spinning, the large amount of produced silk nanofibres is combed by the spider with the use of its backlegs, see figure A.1 G. The combing induces electrostatic charging of the fibres (Kronenberger and Vollrath, 2015; Vollrath, 2006), and subsequent self-repulsion leads
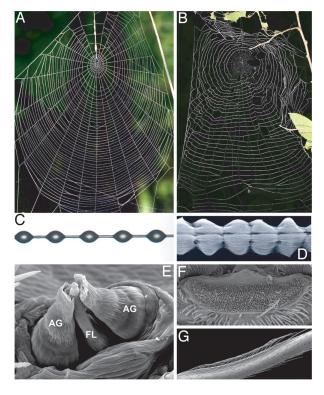

Figure A.1 – Comparison of ecribellate (A, C, E) and cribellate (B, D, F) spider webs (A and B), capture silks (C and D) and spinnerets (E and F,G). Source : Blackledge et al. (2009).

to the observed periodic puffing. Additionnally, van der Waals interactions produce a strong adhesion force, that is analogous to the glue function of ecribellate silk.

A.2   Wet versus dry adhesion

Here we mention the existence of a confusion in the literature (Helmer, 2010). Zheng et al. (2010) wrote a paper in 2010 claiming that the bioinspired design of artificial fibres that mimic the structural features of the capture silk of the cribellate spider *Uloborus* and exhibit its directional water-collecting ability. At the origin of their study was the observation that wetted cribellate spider silk have a periodic structure with thin and aligned nanofibres zones combined with thick and randomly oriented nanofibres. Deposition of a water droplet on this structure allows control of the fluid and preferable settlement on the thick zones. As mentioned above, cribellate capture silk uses dry adhesion, in contrast to the wet ecribellate spider silk.

Consequently, wetting the (dry) cribellate capture silk annihilates the electrostatic interactions on which the adhesion relies. Furthermore, the hundreds of nanofibres – once forming a large puff through electrostatic repulsion – collapse into a much smaller area, which lowers dramatically the contact area. The main task of ecribellate capture silk, adhering strongly to incoming potential preys, is thus ruined by the combination of these two phenomena. The dramatic decrease in adhesion is measured in two ways: the frontal poking of a thread or the side poke followed by retraction. These two methods qualitatively yield similar results. For the frontal poke, the dry work of adhesion is 5 ± 3 nJ while the wet work of adhesion is 0.02 ± 0.03 nJ. For the side poke, the dry work of adhesion is 40 ± 30 nJ and while the wet work of adhesion is 0.07 ± 0.03 nJ. Wetting the cribellate thread is thus highly destructive in respect to its biological function, see figure A.2. We submitted a paper describing this results to the journal *The Science of Nature*.
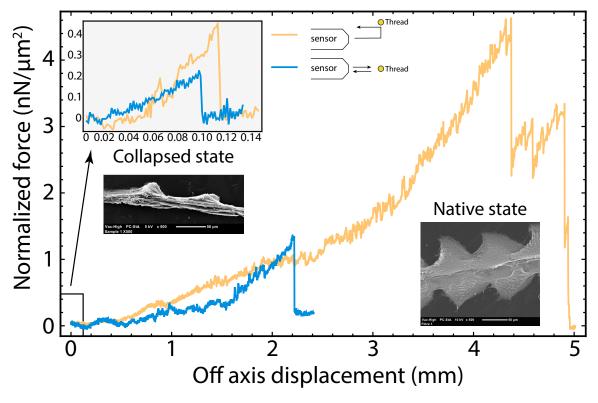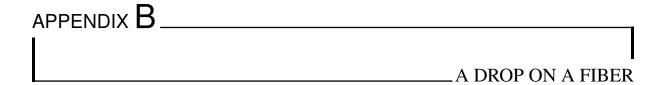

Figure A.2 – Comparison of the adhesion of the cribellate capture silk in its natural and collapsed states (see electron microscope micrographs insets). The adhesion work of collapsed cribellate silk is approximately 500 times lower on average than with cribellate silk in its natural state.

Here we numerically solve the shape of a drop on a fibre, and discuss the spherical drop approximation used in the previous sections. We also define a method for fine measurements of contact angles.

B.1 Shape of a drop on a fiber

A drop finds its equilibrium shape through the wetting interactions with its supporting fibre. In the case of a fibre with vanishing size, the drop tends to be spherical. On the other end, for very large fibres compared to the drop size, the shape of the supported drop will adapt and become cylindrical. The important parameters in the system are the fibre radius r, the drop maximum radius R and the Young-Dupré contact angle θ_Y, shown on figure B.1.

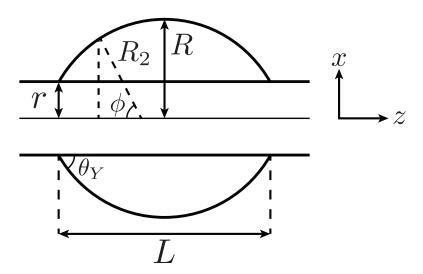**Figure B.1** – Sketch of a drop-on-fibre system with corresponding notations. The point of origin is set in the middle of the drop on the fibre axis. Adapted from Carroll (1976).

In the absence of siginificant gravitational effects, the condition for equilibrium of the drop is that the Laplace pressure ΔP is the same at every point of the drop surface. This yields a geometrical constraint

on the drop shape, and more precisely on the local 3D curvature of the interface. This curvature condition writes

$$1/R_1 + 1/R_2 = K_1 \tag{B.1}$$

where K_1 is a constant, R_2 is the radius of curvature of the drop surface in the plane that includes the fibre main axis, and R_1 is the radius of curvature in a perpendicular plane, see figure B.1. This yields a differential equation on the local radius x and the angle ϕ

$$\cos\phi \frac{d\phi}{dx} + \frac{\sin\phi}{x} = K_1 \tag{B.2}$$

K_1 as well as the subsequent integration constant can be evaluated from the boundary condition at the drop maximum width and at the contact line. This yields a final differential equation on the drop shape as

$$-\frac{dz}{dx} = \frac{x^2 + arR}{\sqrt{(R^2 - x^2)(x^2 - a^2 r^2)}} \text{ with } a = \frac{R\cos\theta_Y - r}{R - r\cos\theta_Y} \tag{B.3}$$

This differential equation can be integrated and leads to a linear combination of elliptic integrals:

$$z = \pm(arF(\varphi, k) + R\,E(\varphi, k)) \text{ with } \sin\varphi = \frac{1}{k}\sqrt{1 - \left(\frac{x}{R}\right)^2} \text{ and } k^2 = \frac{R^2 - a^2 r^2}{R^2} \tag{B.4}$$

where F and E are the elliptic integrals of first and second kind respectively. This equation has been used by Carroll (1976) to calculate analytical expressions of the drop length, volume, surface area and inner pressure. We solved this equation numerically using Mathematica, and plotted the 3D shape of the drop, see an example on figure B.2. The drop resembles a rugby ball, and adopts a unduloidal shape, that is in between a sphere and a cylinder.
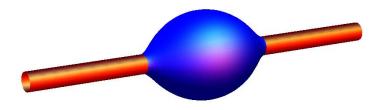

Figure B.2 – Numerical computation of the shape of a droplet on a fibre using equation (B.4).

Meniscus length and the spherical approximation   In the work presented in this manuscript, we considered the drop as quasi spherical for ease of modelling. We can use equation (B.4) to properly calculate the relative divergence of the drop shape from the ideal sphere. We compute the exact shape of a given drop-on-fibre system, along with the wetted fibre length L_w and the drop volume V. The effective radius of the drop R_{eff} is then calculated as $R_{\text{eff}} = \left(\frac{3V}{4\pi}\right)^{1/3}$. The difference between the wetted fibre length

and the effective radius yields the meniscus length $L_m = L_w - R_{eff}$. Physical arguments show that the relative meniscus length $\ell_m = \dfrac{L_m}{R_{eff}}$ only depends on the drop to fibre size ratio, $\dfrac{R_{eff}}{r}$ (Takahashi, 1990; Quéré and Di Meglio, 1994). We further use these dimensionless parameters to quantify the equilibrium of the system.
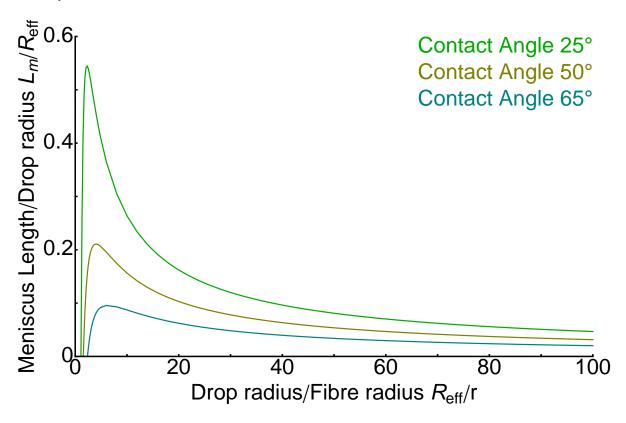

Figure B.3 – Resuls of numerical solutions for the relative meniscus length as a function of relative drop radius for varied contact angles.

Figure B.3 shows the results of calculations for the relative meniscus length as a function of the relative drop radius. The relative meniscus length has a maximum for $\dfrac{R_{eff}}{r} \approx 1.2$, which magnitude depends on the contact angle, and can be quite large and the drop quite oblong. However, for our typical drop-on-coilable-fibre systems, the drop is always much bigger than the fibre, usually by two orders of magnitude. According to figure B.3, this means a meniscus length of 5 to 10 % of the drop radius for a contact angle of 23°, which corresponds to silicone oil on TPU. The assumption of quasi-spherical drop is thus quite well respected.

In order to experimentally verify equation (B.4), we use two test cases: the aspect ratio $\frac{L_w}{2R}$ of a drop on a given fibre as a function of the drop length, and the loss of wetted fibre length for heavy drops. The drop aspect ratio is measured as the drop length over the drop maximum radius. This is done in practice with a 4 µm radius fibre on which many droplets of varying sizes were deposited. The aspect ratio is then measured optically and compared to theoretical values in figure B.4.

The loss of wetted fibre length for heavy drops has been described in section 4.6 and is due to the rotation of the capillary meniscii to accomodate the drop weight. The actual wetted fibre length is measured as the part of the fibre that lies within the drop. In the case of spherical drops without gravity, the wetted fibre length corresponds to the drop radius. However, for non-spherical drops, it corresponds to

the main length of the unduloidal drop. Influence of gravity leads to breaking of the vertical symmetry and the subsequent downward translation of the drop's center of mass, see figure 4.16. Considering a force balance for an ideal spherical drop yields a relation between the actual wetted fibre length and the drop effective radius, see the dashed blue curve in figure B.4 (right). When compared with the experimental data, the trend is well reproduced, showing a linear increase for small drops and a maximum. However, there is an offset between the theoretical values and the actual data. The addition of the meniscus length calculated from equation (B.4) compensates this offset, see the red solid curve in figure B.4 (right).
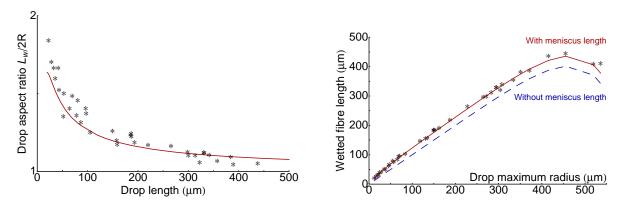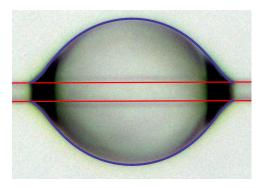

Figure B.4 – Comparison of experimental data and theoretical values for drop aspect ratio versus drop length (left) and wetted fibre length versus drop maximum radius (right) for a 4 μm radius fibre. The actual wetted fibre length is derived from a force balance under gravity (equation (4.12)) (blue dashed curve) and the additional length of the meniscus is calculated from the drop-on-fibre shape equation (B.4) (red solid curve).

B.1.1 Measuring the contact angle

Here we further use equation (B.4) to obtain a reliable measurement of the contact angle. This is a difficult measurement to perform, as the contact angle is the slope of the drop shape at the very location of the contact line. For micronic fibres, this slope connects quickly to the ideal spherical drop shape, leading to a sharp slope gradient. The analysis of the whole drop shape yields much finer measurements. From an snapshot of the system, the fibre boundaries are first fitted by the user as two straight lines. We implemented a dynamic module that overlay a calculated drop shape over the image of the real drop. Maximum drop radius and contact angles are then adjusted to fit the shape, see figure B.5. There are also possibilities of pinning at the contact line, due to physical roughness or chemical inhomogeneities. However, this was not observed in our case. This shows that the prepared fibres are of good quality.

B.1.2 Roll-up instability

For a certain parameters range, the axisymmetric drop shape is not stable and leads to side pearling, known as the roll-up instability. The roll-up instability was first described by Adam (1937) as an efficient way to activate the process of detergency. This is especially true for droplets that weakly wet the material of the fibre, and for small droplets (Carroll, 1986). It is described as a transition in the shape of a drop on a fibre. In the previously presented chapters, we took care to obtain axisymmetric droplets and avoid the roll-up instability, by using sufficiently large amount of liquid, or by increasing the wetting properties of the liquid. However, the non-axisymmetric drop case could perhaps reveal some unintended potential. Indeed, the drop shape is an indication of the wetting properties of the liquid on the considered fibre. Figure B.6 shows what happens when glycerol droplets, that do not wet the PLA fibre
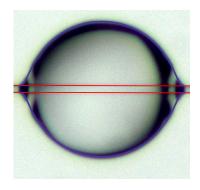
Figure B.5 – Drops of ethanol (left) and silicone oil (right) on a PolyUrethan fibre and shape fit using Carroll equation (B.4). Left: The ethanol drop has a length of $L_w = 134$ μm and the fibre has a diameter of 14 μm. Right: The silicone oil drop has a length of $L_w = 186$ μm and the fibre has a diameter of 7.8μm. This yields values of the contact angle of $\theta_Y = 19 \pm 3°$ for ethanol and $\theta_Y = 23 \pm 3°$ for silicone oil.

on which they sit, are exposed to an ethanol mist. The slight addition of ethanol to glycerol changes the wetting properties and induce the recovery of the axisymmetric shape.
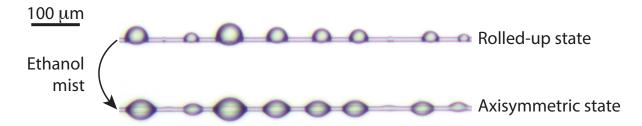

Figure B.6 – Left : Glycerol droplets on Poly Lactic Acid (PLA) fibre. Glycerol does not wet PLA, so the drops are rolled up. Right : Same sample, but under an ethanol-saturated atmosphere. Glycerol sucks up ethanol, and the resulting droplet wets PLA with a restored axisymmetric shape.

B.2 Force of a drop on a fiber

To quantify the action of the drop on the fiber, one can measure the actual capillary force exerted by the meniscii. To do so, we use two different techniques. Both of them have the merit of discarding the inherent drift and offset of the sensor, explained in appendix D.5. The idea is to put a TPU thread of known diameter under slight tension, record the background force during 25 seconds (500 points), then apply silicone oil brushing. The peak of force has a magnitude of roughly 20μN and lasts around one second, and the system relaxes within merely 3 seconds. After the relaxation, we record the new force during another 25 seconds, and measure the mean value. The difference between the forces before and after silicone brushing is expected to be the capillary force. The reverse process can be exploited too: record the force with a droplet, then remove the droplet and measure the difference with the new force. The two techniques give similar results, within the measurement noise of magnitude 10nN for the FT-FS100 sensors, and 100nN for the FT-FS1000 sensors (see appendix D.5). Force measurements using the two techniques are shown on figure B.7. The number of droplets does not matter: in effect, only the last meniscus pulls on the part of the fiber attached to the sensor. We verified this assumption by changing the number of droplets from 1 to dozens, and it has indeed no effect. Furthermore, the capillary force has an expected value of $2\pi r\gamma \cos\theta$, and thus does not change with drop size. This has

been experimentally verified as well, within measurement errors margins.

We measured 440 ± 100nN for a 8.3µm diametre fibre (expected value $2\pi r\gamma \cos\theta = 506$ nN) and 103 ± 10nN for a 1.9µm diametre fibre, with an expected value of $2\pi r\gamma \cos\theta = 116$ nN.

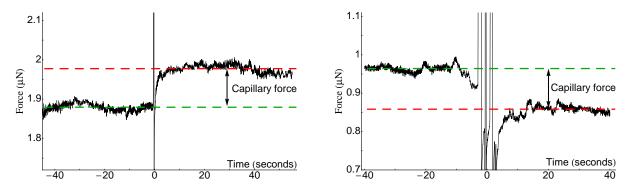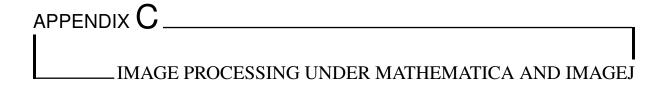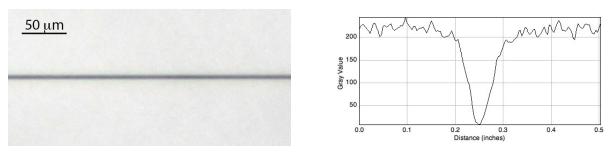**Figure B.7** – Measurement of the capillary force of a silicone droplet on a fibre. The measurement method is to record the background force, then apply silicone oil and measure the difference in force (left) or alternatively to record the background force with the drop, and remove it (right). The TPU fibre diameter here is 1.9 µm and the silicone oil drop has an effective radius of 85 µm (left) and 62 µm (right).

APPENDIX C

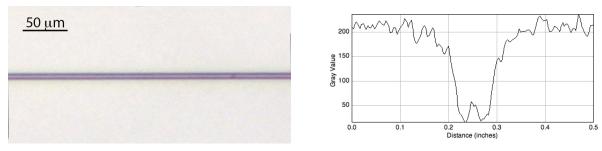## IMAGE PROCESSING UNDER MATHEMATICA AND IMAGEJ
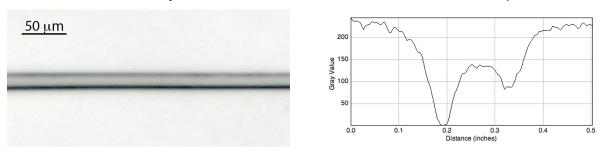
C.1   Fibre diameter measurement

In this PhD work, we have made extensive use of centimetre-long micronic fibres. The proper measurement of the fibre diameter is a crucial parameter to complete a quantitative study. Furthermore, the coiling criteria (equations (1.4) and (1.6)) require high experimental precision. The TPU fibre diameter measurement was performed using Fiji (update of ImageJ) software. The TPU fibre is glued onto the jaws of a caliper, for proper clamping conditions, as well as for ease of backlighting. As the fibre is transparent, this leads to better measurement. A high-resolution picture of the fibre is taken using the experimental setup described in section 2.2.2, mainly a camera and a microscope lens. It is then analysed using the following steps : the contrast is enhanced up to the point where 0.4% of the pixels are saturated, then the grey value of the pixels on a line perpendicular to the fibre axis is plotted. The typical obtained curve resembles a downward pointing gaussian, thus the diameter of the fibre is extracted as the width at half minimum of the peak. This allows for sub-diffraction resolution measurements of fibre diameter. An accuracy of 350nm has been achived on fibre radii using this technique, cancelling out the influence of diffraction. We can hence use small numerical aperture microscope to enjoy the benefit of a large working distance (up to 54mm here) while keeping a resolution close to the limit of visible light.

(a) Profilometry of a small fibre. The measured diameter is 3.0±0.7 µm.

(b) Profilometry of an medium-sized fibre. The measured diameter is 6.8±0.7 µm.

(c) Profilometry of a large fibre. The measured diameter is 17.7±0.7 µm.

Figure C.1 – Profilometry of fibres of different sizes. The diffraction profile leads to a high accuracy measurement.

C.2   Fibre quality

In the previous chapters, we consider that the fibre has a constant radius for ease of comparison with the theroretical and numerical works. Using the technique described above, we extract a typical profile of local fibre diameter to verify its homogeneity, see figure C.2. The fibre local diameter might look inhomogeneous, but considering a measurement error of 0.7 µm and the difference of scales (fluctuations of micrometres over centimetres), the fibres can be considered as smooth and of good quality. We then perform 5 to 10 local diameter measurements and use the average value in further calculations.
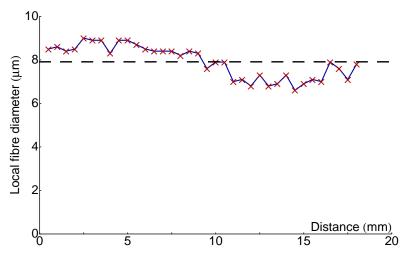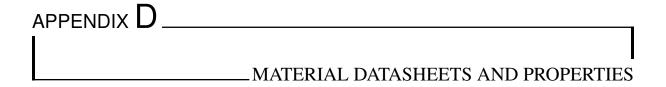

Figure C.2 – Typical profilometry of a fibre.

APPENDIX D

MATERIAL DATASHEETS AND PROPERTIES

D.1 ThermoPlastic PolyUrethane (TPU)

Our soft Thermoplastic PolyUrethan comes from BASF, where it has a product name of Elastollan 1185A. The datasheet value of the Young's modulus of the TPU is 20.5 MPa, the softest we could find, so that the critical fibre radius is as high as possible (see equation (1.6)). This value has been verified in situ after fibre production, to be sure that there are no effect of size or processing speed on the fibre rigidity.

BASF specifically designed Elastollan for extruded profile, sheet and film applications. It exhibits excellent abrasion resistance, toughness, transparency, very good low temperature flexibility, hydrolytic stability and fungus resistance. It has excellent damping characteristics and outstanding resistance to tear propagation. TPU is supplied uncolored in pelletized form.

D.2 PolyLactic Acid (PLA)

Here we used PolyLactic Acid (PLA), as it is a thermoplastic (hence easy to mold into thin fibres) that has a glass transition temperature of 60°C. Its Young's modulus is 2 GPa at room temperature, while it decreases down to 4 MPa at 80°C. The thousandfold decrease in rigidity means that the windlass activation threshold can easily be gone through by use of temperature, which makes it activable at will, see section 5.3.1.

It was initially used in our 3D printer from Makerbot, where it comes in the standard form of a 900g spool of 1.75 mm filament. PLA is a biodegradable thermoplastic aliphatic polyester derived from renewable resources, such as corn starch or sugarcane.

D.3 Silicone oil from Rhodorsil

We used silicone oils from Rhodorsil. They are polydimethylsiloxane oils, which are constituted of linear molecular chains of varying lengths whose groups comprise alternating silicon and oxygen atoms (the Si-O-Si siloxane bond). The silicon atoms are saturated by methyl groups - CH_3. Whilst the carbon chains of organic substances generally have low resistance to external influences, the stability of the Si-O bonds is basically comparable to that of inert mineral silicates, which makes it a good candidate for experiment where the stability of physical properties is required.

We mainly used a silicone oil called V1000, 1000 times more viscous than water. We used some V20 and V5 as well when low viscosity was required, for instance to coil brittle materials such as glass, see section 5.4.

D.4   Leica microscope and optical setup

The optical setup consisted of a Leica macroscope (VZ85RC) mounted on a micro-step motor and a 3 megapixels Leica DFC-295 camera (C-mount lens 400× angular zoom, working distance 54 mm, numerical aperture 0.12) for high resolution snapshots. The theoretical picture resolution is 334 nm/pixel, without taking diffraction into account. This is discussed in details in appendix C.1. For video recording, we used a D800E Nikon camera with three 10 mm C-mount extension rings (937 nm/pixel video resolution and 374 nm/pixel photo resolution). The very high resolution is particularly useful as it is used as an accurate measurement method. The depths of field with the Leica DFC-295 camera is 2.7 mm and 80 μm at 50× and 400× angular zoom respectively. The fields of view are 6.1 mm and 780 μm at both extremes. We used a long life highly uniform $50{\times}50$ mm^2 Phlox backlight at 60 klux or alternatively an optical fibre with LED lamp (50 W Moritex MHF-M1002 at 100 klux) with circular polarizers to avoid reflections. Side views were acquired with a second D800E Nikon camera, with a 70 mm extension tube and a 100 mm macro Zeiss lense (7,27 microns/pixel video resolution). All of it mounted on an optical table for stability.

D.5   FemtoTools force sensors and SmarAct linear micro-step motor

The force sensors we used are capacitive deflection force sensors, from the Zurich-based FemtoTools$^{®}$ company, see figure D.1. They use a unique method for measuring tiny forces (down to tens of nN) both in compression and traction. It works thanks to a calibrated series of capacitors, coupled with a tip made of a mono-crystal of silicon. When the tip is stretched, so is the series of capacitors. The capacitance of the full electronic system is a function of the spacing between the plates that make up each capacitor, and varies as the inverse of this distance. Thus, a signal can easily be recorded when stretching or compression occurs. A high number of capacitance with small spacing leads to a high sensitivity, at the scale of a few tens of nN. A data acquisition system is set for direct writing in a text file. The usual sampling frequency is 20 Hz, far below the 100 kHz capability of the sensors.

Each sensor comes with its individual calibration, on the order of 50 μN V^{-1} for the most sensitive sensors (FT-FS100). The sensors offer low transversal sensitivity, roughly 1000 times smaller than the in-axis sensitivity, which makes them very accurate. Each sensor has 4.5 decades of measurement range. The FT-FS100 ranges from 5 nN to 100 μN. The FT-FS1000 ranges from 50 nN to 1 mN and FT-FS10000 ranges from 500 nN to 10 mN. Each sensor costs approximately 500€ and are very fragile, so great care was taken for their manipulation.
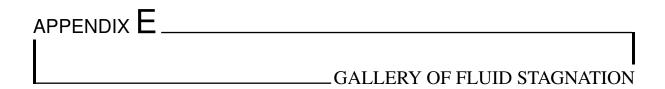
They have a magnetic shield to avoid electrical noise from magnetic background (cell phones, other measurement devices,...). They have a good long-term time stability, although a noisy drift of average slope 1nN s^{-1} (for the FT-FS100) was observed. The drift was erratic, so no offset compensation was possible, but for short experiments, the actual accuracy is within 10 nN. After a quick load, the sensors exhibit a good elasticity and very fast relaxation, around 10 μs. It actually relaxes much faster than our TPU fibres, thus the sensor response time can be neglected for our force measurements.

The sensors are mounted on a linear micro-step positioner SmarAct SLC-1730, with a 21 mm range, controlled by an external station with direction and speed control. Either continual or step displacement are available, with a velocity range from 5 μm s^{-1} to 15 mm s^{-1}. Speed levels were calibrated, and

Figure D.1 – A FemtoTools force sensor measures down to tens of nN with a capacitive deflection technology.

recorded as non constant along the course of the positioner, and varied by up to 10%. All the tests were performed in traction at an average speed of 12 μm s^{-1}. Considering the centimeter size in length of the sample, they can be considered quasi-static. Speed has been varied well below and slightly above this value, and no significant difference has been observed. The actual length of the sample and position of the drop are measured optically with a large side view camera (see figure 2.4). To decrease noise measurements levels, electronic contacts were insulated from the (metallic) optical table using electrical tape or styrofoam bottom. Gluing samples onto the sensor tip does not actually work, because the liquid glue creeps into the electronic and short-circuits the whole sensor. The samples are then attached to the sensor tip by wrapping a significant length of thread (at least 5 turns are done around the tip). The attachment is then tested during a couple of cycles of medium amplitude to verify its stability. It is verified that the rest length remains the same over cycles, both with force measurements and optically.

APPENDIX E

GALLERY OF FLUID STAGNATION
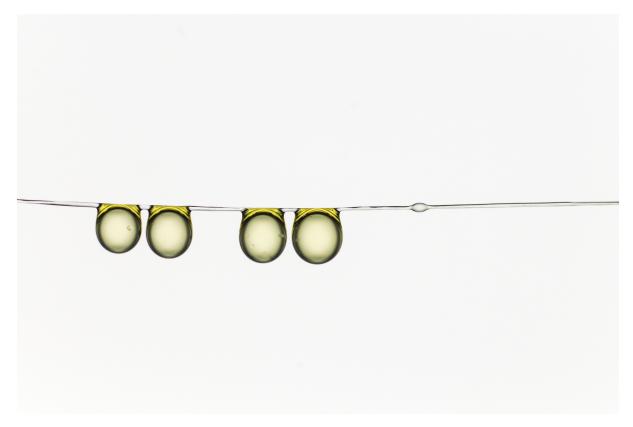
Figure E.1 – Olive oil on elastan.
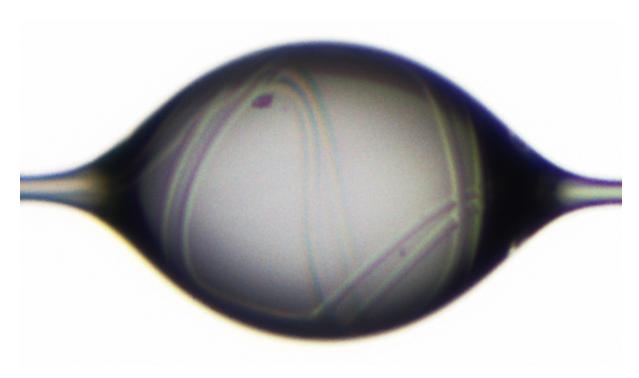
Figure E.2 – Windlass mechanism in natural spider silk sample.
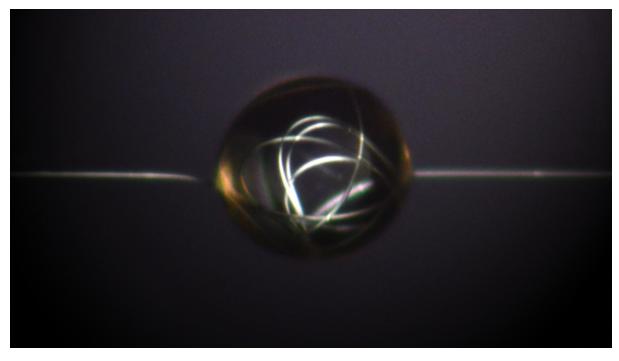
Figure E.3 – Soft ThermoplasticPolyUrethan and silicone oil droplet under polarized light offers a clear view of the universal windlass mechanism.
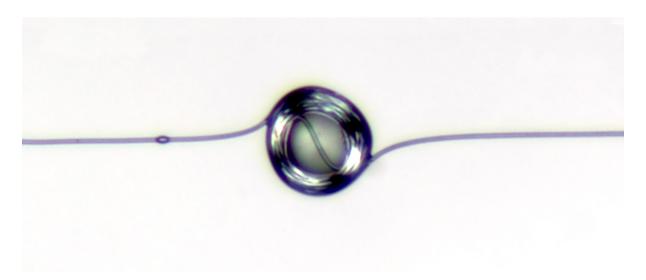
Figure E.4 – Localized coiling of TPU in silicone oil.
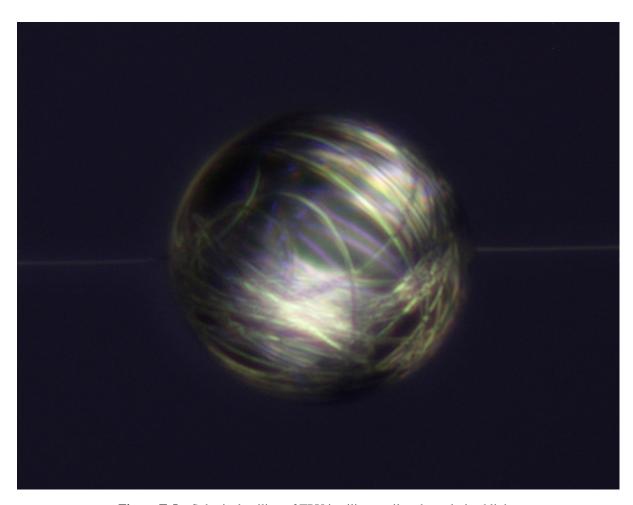
Figure E.5 – Spherical coiling of TPU in silicone oil under polarized light.
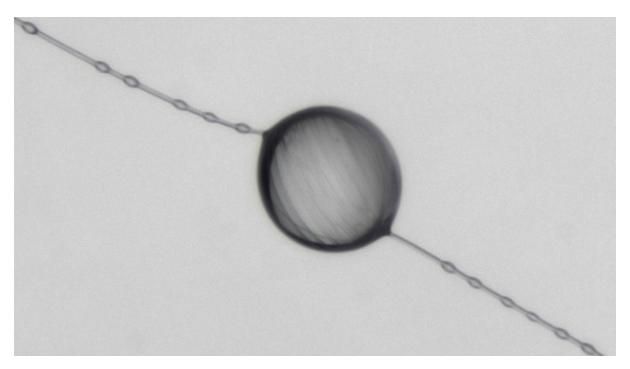
Figure E.6 – Artistic coiling.
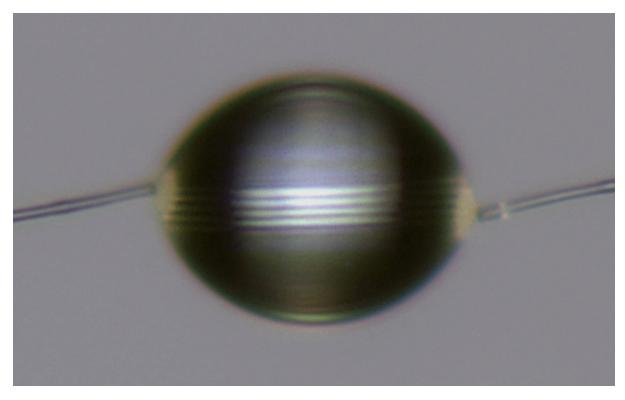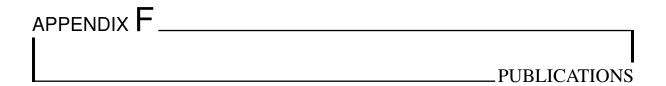
Figure E.7 – Organized coiling.

APPENDIX F

We wrote three papers on the results of this PhD work, with two currently in review at *PNAS* and *The Science Of Nature, Springer*.

- "In-drop capillary spooling of spider capture thread inspires highly extensible fibres." *In review at PNAS* (2015).

- "Coiling of an elastic beam inside a disk: A model for spider-capture silk." *International Journal of Non-Linear Mechanics, Elsevier*, 75:59–66 (2015).

- "Adhesion of dry and wet cribellate silk", *The Science Of Nature, Springer*, 102(7):1–4 (2015).

A fourth paper is currently being written, and will regroup the results presented in chapter 4.

In-drop capillary spooling of spider capture thread inspires highly extensible fibres

Hervé Elettro [*] , **Sébastien Neukirch** [*] , **Fritz Vollrath** [†] **and Arnaud Antkowiak** [*]

[*]Sorbonne Universités, UPMC Univ Paris 06, CNRS, UMR 7190 Institut Jean Le Rond d'Alembert, F-75005 Paris, France., and [†]Oxford Silk Group, Zoology Department, University of Oxford, UK

Spiders' webs and gossamer threads are often paraded as paradigms for lightweight structures and outstanding polymers. Probably the most intriguing of all spider silks is the araneid capture thread, covered with tiny glycoprotein glue droplets. Even if compressed, this thread remains surprisingly taut – a property shared with pure liquid films – allowing both thread and web to be in a constant state of tension. Vollrath and Edmonds proposed that the glue droplets would act as small windlasses and be responsible for the tension, but other explanations have also been suggested, involving for example the macromolecular properties of the flagelliform silk core filaments. Here we show that the nanolitre glue droplets of the capture thread indeed induce buckling and coiling of the core filaments: microscopic in-vivo observations reveal that the slack fibre is spooled into and within the droplets. We model windlass activation as a structural phase transition, and show that fibre spooling essentially results from the interplay between elasticity and capillarity. This is demonstrated by reproducing artificially the mechanism on a synthetic polyurethane thread/silicone oil droplet system. Fibre size is the key in natural and artificial setups which both require micrometer-sized fibres to function. The spools and coils inside the drops are further shown to directly affect the mechanical response of the thread, evidencing the central role played by geometry in spider silk mechanics. Beside shedding light on araneid capture thread functionality, we argue that the properties of this biological system provide novel insights for bioinspired synthetic actuators.

The orb-webs of araneid spiders are highly effective and efficient traps that are able to fully cushion the impact of an insect within a second and then manage to keep the prey well ensnared in a wet-sticky capture spiral until the spider can reach it (1). The exceptional extensional properties of the spiral threads rely on the macromolecular architecture of the silk fibroins (2; 3) while the ability to contract, self-tense and adapt slack length with virtually no hysteresis has been attributed to a surprisingly complex mechanical micro-mechanism (4). Here we are setting out to test this micro-windlass hypothesis. To date it is based mostly on indirect snap-shot observations of various amounts of coiled threads inside capture spiral droplets laid down on a microscope slide (4) combined with the interpretation of mechanical behaviour. The lack of direct, dynamic observation of the phenomenon has given rise to criticism refuting the conclusions of an active mechanism driving the system (see (5) with reply (6) and summary (7)). Much of the criticism was dismissed by empirical studies (6) but a fundamental question must be taken seriously: after all, the physics of such a mechanism would require the watery coating of the thread to be able to *(i)* exert forces sufficiently powerful to rapidly tension substantial lengths of the filament which bears hundreds of nanolitre droplets, and *(ii)* hold the composite system in place without sagging against gravity. Actually, the vast literature on liquid coating on fibres, whether in textile (8) or glass filaments (9) products or indeed in biological applications such as the wetting of mammalian hairs (10), does not contain any reports of such drop-induced 'windlass' events.

Our results fully support the windlass theory and identify the fundamental mechanism to be dependent on the interplay between elasticity and capillarity. Moreover, we demonstrate empirically as well as theoretically that this mechanism is generic, *i.e.* not requiring silk proteins in either the filaments nor the droplets as fundamental material components. This not only elucidates the physics of the system but also opens the way for the design of novel bio-inspired synthetic actuators using the windlass array concept.

Significance

The spiralling capture threads of spider orb webs are covered with hundreds of tiny glue droplets whose primary function is to entrap insects. In this paper we demonstrate that the function of the drops goes beyond glueing preys, for they play a role in the extreme extensibility of these fibres, usually ascribed to the complex molecular architecture of the silk. Indeed each of the droplet can spool and pack core filaments while tensing the thread and the whole web. We demonstrate that this effect is the result of the interplay between elasticity and capillarity by designing an entirely artificial drops-on-fibre compound as extensible as a capture thread is. These results lay the foundations for a new generation of bioinspired actuators.

Reserved for Publication Footnotes

I $T > T_P$

II $T \simeq T_P$

X

1 mm

III $T < T_P$

Figure 1. **A liquid-like fibre**. Whether stretched or relaxed, the typical capture silk thread of an araneid orb spider (here *Nephila edulis*) remains taut. Force monitoring reveals a threshold tension T_P above which the fibre behaves like a spring (**I**). As the force is decreased a force plateau $T \simeq T_P$ is reached, along which the fibre adopts a wide range of lengths, just as soap films do (**II**). At lower forces, $T < T_P$, the fibre is totally contracted (**III**). See also Supplementary Videos for full cycle.
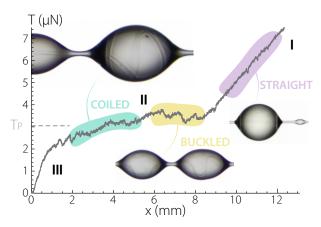

Figure 2. **Shape-induced functionalization.** Quasi-static force measurements on spider capture threads combined with microscopic observations demonstrate that the slack core filament is spooled into the droplets (typically 250-300 μm wide) along the force plateau $T = T_P$. For larger forces $T > T_P$, the fibre straightens and a spring-like behaviour is shown. The characteristic J-shape for this force-extension curve can be attributed to a shape-induced functionalization of the fibre by the glue droplets (see also Supplementary Video).

Figure 1 outlines the macroscopic observation of the system. The natural set-up is fully self-assembling, with the spider coating the core fibres of the capture spiral with a thin layer of hygroscopic compounds (11). This layer then swells by taking up water from the atmosphere and go through a Plateau-Rayleigh instability to form a string of interconnected silk droplets sitting astride the core silk fibres (12). This natural micron-sized windlass array system ensures that the capture thread is always under tension – independent of any extension or relaxation. As the capture thread is stretched, lengths of core filament are simply strained or, depending on past action, pulled out of a droplet. It appears that the sur-

face tension of the droplet is strong enough to pull-in the silk filament, which buckles and then coils up inside the liquid.

Figure 2 shows force-elongation measurements performed on a single capture thread, accompanied by microscopic observations of core fibre coiling within the glue droplets. This data reveals the self-organisation of the core filaments into coils within the droplet, and determines the link between the shape of the filament and the mechanical response of the thread. Indeed the observed mechanical response encompasses three different stages, each characterized by a typical force-displacement relation and a specific filament shape within the drop. At very low tension T exerted on the fibre, the central glue droplet, resulting from the successive merging of tiny drops, has 'ingested' a large amount of spare fibre and presents a roughly linear relation between force and extension, see region **III**. As a plateau force $T \simeq T_P$ is reached, the filament starts uncoiling and exiting the drop, allowing this composite system to effortlessly reach very large extensions, see region **II**. Interestingly this mechanical response, associated with unspooling, bears little resemblance with the typical response of a fibre, and is much more reminiscent of the mechanics of soap films (13). Past the threshold where all the coils have been straightened, the capture thread recovers a classic drop-on-(straight) fibre appearance along with a linear stretched spring regime response, see region **I**. This trimodal response of the capture thread is not unlike the typical response of a Shape Memory Alloy (SMA) fibre, see Figure 3. And indeed in both systems the plateau regime corresponds to a phase transition: from austenite to martensite in SMA, and from coils-in-drop to straight fibre in capture silk.

To elucidate the conditions for the windlass action, we examine this phase transition further. We start by considering a model capture thread composed of a soft fibre capable of being bent or stretched and subjected to an external tension T, supporting a wetting liquid drop standing astride (14). Though thin, silk filaments are not expected to be significantly excited with thermal fluctuations: the persistence length of such filaments is indeed estimated to be kilometer-sized (15), to be compared with a few tens of nanometers for DNA. Disregarding entropic elasticity effects, we describe windlass activation as a phase transition between a coiled phase – where the fibre is entirely
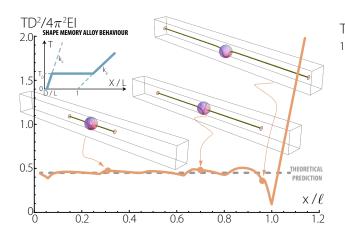
Figure 3. **Windlass as a structural phase transition.** Numerical simulations of a slender fibre supporting a drop sitting astride unravel a subcritical buckling transition where the slack fibre is suddenly localised within the droplet. Continuation of equilibria, with $F_\gamma D^2/(4\pi^2 EI) = 0.5$ and $L = 20\,D$, reveal the fine details in the micro-mechanical response, resulting in inhomogeneities in the Maxwell plateau. The approximate plateau value $T_P D^2/(4\pi^2\,EI) \simeq 0.45$, given by equation (2), is drawn for comparison. Several equilibrium configurations illustrate the coiling of the fiber and its strong packing within the droplet. The mechanical response is typical of systems exhibiting first-order phase transitions (such as shape-memory alloys - SMA), and the numerical results are confirmed by an analytical model involving a wet/coiled (analog to the austenite phase in SMA) and a dry/stretched (analog to the martensite phase in SMA) phase (see inset).

Figure 4. **A synthetic windlass mechanism.** Combined quasi-static mechanical measurements and polarizer-analyzer observations of silicone oil droplet sitting astride thin TPU fibre ($h = 2.3 \pm 0.15\mu m$, $E = 17 \pm 3$MPa, and wetting angle $\theta = 36 \pm 7°$ for the left inset) demonstrate that the key features of the spider capture thread can be obtained with an artificial system. The natural mechanical response of TPU, shown in dashed line, is significantly altered by the addition of an oil droplet (wet length $380\mu m$ for the left inset), resulting in a highly extensible system (here $+9000\%$ breaking strain). The resulting J-shape curve appears to be associated with elastocapillary spooling within the oil droplet, in agreement with our theoretical description (see also Supplementary Video).

packed within the liquid drop – and an extended phase – where the thread runs straight outside the drop. The extended phase is modelled as a spring with stiffness $k_e = \pi E h^2/\ell$, where ℓ stands for the rest length, E the Young's modulus of the fibre and h its radius. The strain energy of the extended phase is then $\frac{1}{2}k_e(x_e - \ell)^2$, where x_e is the phase's extension. The coiled phase typically describes the system at low applied tension T. In the limit $T = 0$ the coiled phase extension is $x_c = D$ where D is the diameter of the, then spherical, liquid drop. As tension starts rising, the liquid drop deforms into an elongated shape. Modelling the deformation as ellipsoidal yields the following spring-like relation: $T = \frac{4}{5}\pi\gamma(x_c - D)$, where γ is the liquid surface tension. The strain energy of the coiled phase is then $\mathcal{E}_c = \frac{1}{2}k_c(x_c - D)^2$ where the spring stiffness of the liquid drop directly arises from surface tension $k_c = \frac{4}{5}\pi\gamma$. As typical for phase transition problems, there is an energetical cost per unit length associated with the transformation from the coiled phase to the extended phase, which we note ϵ_0. This energy originates from both the uncoiling of the fibre and the energy difference between wet and dry states. The uncoiling process results in an elastic energy gain $-\frac{1}{2}EI\kappa^2$ per unit length, where the curvature $\kappa = 2/D$ and $I = \frac{\pi}{4}h^4$. The latent energy per unit length also embodies the difference in surface energies: in the coiled phase the fibre is surrounded by liquid, hence bears a surface energy $2\pi h\gamma_{sl}$ per unit length whereas in the extended phase the air surrounding the fibre yields an energy $2\pi h\gamma_{sv}$ per unit length. Here γ_{sl} and γ_{sv} denote solid-liquid and solid-air interface energies respectively. It is to be noted that a surface energy constrast between the coiled and extended phase persists even if a thin liquid film sheathes the core filament, for the energy of a filament coated with a thin liquid layer differs from that of a filament immersed in liquid (13). Upon using Young-Dupré wetting relation $\gamma_{sv} - \gamma_{sl} = \gamma\cos\theta$, the energetical cost for phase trans-

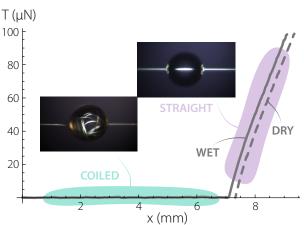formation is obtained: $\epsilon_0 = 2\pi h\gamma\cos\theta - \frac{1}{2}\pi E h^4/D^2$, where θ is the liquid contact angle on the fibre. From this expression we readily obtain conditions for windlass activation. Indeed, for the coiled phase to be stable at small extensions x, ϵ_0 has to be positive. This condition can be recast into a condition for the radius, where it becomes apparent that only extremely thin fibres can deploy a windlass:

$$h < \left(\frac{4\gamma\cos\theta}{E}\right)^{1/3} D^{2/3} \qquad [\mathbf{1}]$$

Noting the total energy $\mathcal{E}_e$ of the extended phase as $\mathcal{E}_e = \frac{1}{2}k_e\,(x_e - \ell)^2 + \epsilon_0\ell$, we write the global energy when part of the fibre is in the coiled phase, and part in the extended phase. Denoting the extended phase fraction ρ, the global energy $\mathcal{E}(x_e, x_c, \rho)$ reads: $\mathcal{E} = (1 - \rho)\mathcal{E}_c(x_c) + \rho\mathcal{E}_e(x_e)$. Minimizing this energy we find that the fibre can be entirely in the coiled phase ($\rho = 0$; filament fully packed in the drop) with tension $T = k_c(x - D)$, or entirely in the extended phase ($\rho = 1$) with tension $T = k_e(x - \ell)$. A third interesting possibility consists in a mixture of phases $0 < \rho < 1$. In this latter case, part of the filament is packed in the drop but the outer part is taut, consistent with our observations. In the limit where $D \ll \ell$ and $\epsilon_0 \ll k_e, k_c$, we have $x_c \simeq D + \epsilon_0/k_c$, $x_e \simeq \ell + \epsilon_0/k_e$ and $T \simeq T_P \simeq \epsilon_0$, so that the plateau tension is

$$T_P \simeq 2\pi h\gamma\cos\theta - \frac{1}{2}\pi E\frac{h^4}{D^2} \qquad [\mathbf{2}]$$

We performed detailed numerical computations of equilibrium of an extensible and flexible elastic fibre (16; 17). The filament, held at both extremities with imposed distance x, was subjected to attracting meniscus forces F_γ at entrance and exit of a confining sphere. The loading (x, T) diagram, shown in Fig. 3, reveals inhomogeneities in the Maxwell line. These inhomogeneities are due to fine details in the micro-mechanical response (spooling and unspooling events) of the

a) **BARE FIBRE**

b)

PUSH   PUSH

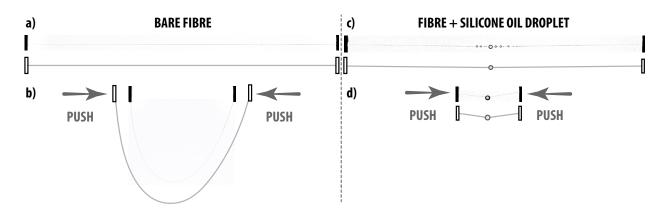c) **FIBRE + SILICONE OIL DROPLET**

d)

PUSH   PUSH

Figure 5. **Artificial spider capture thread.** Left: a thin micrometer-sized TPU filament is held on a caliper. Bringing the ends together leads the filament to exhibit a characteristic catenary-like sagging shape (note: the outlines serve as guides for the eye). Right: This behaviour changes after deposition of a small silicone oil droplet on the filament: bringing the extremities closer leaves the filament taut while the excess filament enters the central droplet.

system. Setting $F_\gamma = 2\pi h\gamma\cos\theta$, we plot in Fig. 3 the horizontal line corresponding to equation (2), and see that it compares well with numerical computations.

Our theoretical results show that, provided capillarity prevails over filament elasticity, elastocapillary spooling can be initiated on any flexible fibre, and that there is no need for any rearrangement in the molecular architecture. We experimentally demonstrated this material independence by triggering windlass on a soft Thermoplastic PolyUrethane (TPU) micron-sized filament. As soon as a single silicone oil droplet was deposited on the sagging TPU filament, the fibre straightened and a tension force on the fibre of typically 1 μN immediately developed. We performed tensile tests and observed that the force curve, see Fig. 4, exhibited the plateau regime with $T_P \sim 1\mu$N until the filament was totally straight and the spring regime started. Snapshots of the filament within the oil droplet in the plateau and spring regimes are shown in Fig. 4 and confirm the link between filament shape and the mechanical response of the system. In addition we show in Fig. 5 that a synthetic TPU fibre displayed the same overall properties of hypercontraction than capture silk: the liquid drop put the system in tension and there was virtually no sagging, even up to fivefold length reduction.

Interestingly the addition of the oil droplet allows to turn (and tune) the mechanical response into the J-shaped curve so typical of many collagenous tissues (18). Mimicking the mechanical response of biological tissues with synthetic materials certainly offers appealing perspectives for e.g. the design of artificial muscles. Actually, more than the material properties, this is the shape of the strongly curled spools of core filament, reminiscent of packed DNA in bacteriophages (19), that drives the mechanical response of both the natural and the artificial systems. These typical examples of shape-induced functionalization (20) illustrate the fact that geometry plays a key role in spider silk and TPU/oil droplet 'extreme' mechanics (21; 22).

In conclusion we have shown that the mechanical response of capture silk relies on it being a thin fibre decorated with drops powering the micro-windlass action. Thus the extraordinary mechanical behaviour of araneid spider capture silk relies more on the macroscopic composite structure than on the microscopic material properties, underlining that natural se-

lection sometimes cleverly tinkers by coopting simple laws of physics (23).

Materials and Methods

Capture silk samples. Our **Nephila edulis** spider was kept in a $80 \times 80 \times 30$ cm vivarium, consisting of wood panels, PMMA windows and artificial plants. The spider was kept at high humidity (above 70%) and comfortable temperature (above $22°$C) with a 12/12 hr day/night schedule. The spider was fed crickets and flies three times a week. Sections of web were carefully excised using a soldering iron for transfer within a rigid frame. To visualise the fibre running through each droplet, the humidity was set to 100% rH for 15 minutes before observation. The humidity was then stepped down to 50% (observation) rH.

Artificial samples. PolyUrethane (TPU, Elastollan 1185A from BASF$^{®}$) granules were deposited on a hot plate at $230°$C. After melting, we used a tweezer to pick up a small droplet which was then stretched quickly while at the same time being released into ambient room temperature. This resulted in the creation of micron-sized, metre-long, soft filaments. The filament was then deposited on the measuring setup as outlined below. A droplet of silicone oil (Rhodorsil$^{®}$ 47V1000) was then deposited by gently touching and brushing the filament with a drop hanging from a pipette.

Measurement methods. Filament samples were transferred to the measuring setup by coiling one end around the tip of a FemtoTools FT-FS1000 capacitive deflection force sensor (50 nN-1mN range) and gluing the other end to a glass slide as base. The force sensor was mounted on a linear micro positioner SmarAct SLC-1730 (repeatability 0.5 μm) and measurements are performed through a work station by USB connection. All the tests were performed in stretching at a speed of 25μm/s, and considering the centimeter size in length of the sample, they can be considered to be quasi-static. The optical setup consisted of a Leica macroscope (VZ85RC) mounted on a micro-step motor and a 3 megapixels Leica DFC-295 camera ($400\times$ zoom, 334 nm/pixel picture resolution) or a D800E Nikon camera with 3 10mm C-mount extension rings (937 nm/pixel video resolution and 374 nm/pixel photo resolution) alternatively. We used a Phlox 50x50 mm backlight, at 60000 lux or alternatively an optical fibre with LED lamp (Moritex MHF-M1002) with circular polarizer. Side views were acquired with a second D800E camera, with a 70mm extension tube and a 100mm macro Zeiss lense (7,27 microns/pixel video resolution). The force sensor was tared to zero with the fibre compressed slightly more than its slack length, so that it sags, but only minutely, be it for fibres with or without droplet. The measurement of the slack length was performed by pulling on the filament at one end by a few micrometers to straighten the fibre.

The TPU fibre diameter measurement was performed using Fiji software. A high-resolution picture of the fibre is analysed using the following steps : the contrast is enhanced up to the point that 0.4% of the pixels are saturated, then the grey value of the pixels on a line perpendicular to the fibre axis is plotted. The typical curve obtained this way resembles a downward pointing gaussian, thus the diameter of the fibre is extracted as the full width at half minimum of the peak.

Numerical computations. The windlass system is modeled as an elastic filament, obeying Kirchhoff equilibrium equations, in interaction with a sphere. Except at the two 'meniscus' points, the filament is prevented from touching or crossing the sphere through a soft-wall barrier potential. The equilibrium of the system is solved using

two-points boundary-value problem techniques (shooting method in Mathematica, and collocation method using the Fortran - AUTO code).

Appendix: Supplementary information

The coiled phase has extension x_c. It is modeled as a linear spring with stiffness $k_c = 4/5 \, \pi \gamma$, where γ is the liquid surface tension. The tension-extension relation is then

$$T = 4/5 \, \pi \, \gamma (x_c - D) \qquad [\mathbf{3}]$$

where D is the diameter of the drop at $T = 0$. The strain energy of the coiled phase is then

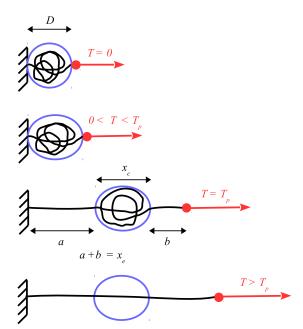$$\mathcal{E}_c = 1/2 \, k_c \, (x_c - D)^2 \qquad [\mathbf{4}]$$

Figure 6. Two phase model. The windlass system comprises two phases. The extended phase consists of the fiber that lies outside the drop(s). The coiled phase consists of the the fiber that is coiled inside the drop(s). Each phase has its own extension, and there is a fraction ρ (resp. $1 - \rho$) of the complete fiber is the extended (resp. coiled) phase.

The extended phase has extension x_e. It is modelled as a spring with stiffness $k_e = \pi \, h^2 \, E/\ell$ and rest length ℓ, where E is the Young's modulus of the fiber and h the radius of its circular cross-section. The tension-extension relation of the extended phase is then

$$T = \pi \, h^2 \, E(x_e/\ell - 1) \qquad [\mathbf{5}]$$

As explained in the main text, ϵ_0 is the energy associated with the transformation of a unit length of the coiled phase into a unit length of the extended phase:

$$\epsilon_0 = 2\pi \, h \, \gamma \cos\theta - 1/2 \, \pi E \, h^4/D^2 \qquad [\mathbf{6}]$$

where θ is the wetting angle of the liquid on the fiber. The total energy of the extended phase is then

$$\mathcal{E}_e = 1/2 \, k_e (x_e - \ell)^2 + \epsilon_0 \, \ell \qquad [\mathbf{7}]$$

When a fraction ρ (respectively $1 - \rho$) of the system is in the extended (resp. coiled) phase, the global energy $\mathcal{E}(x_e, x_c, \rho)$ is given by:

$$\mathcal{E} = (1 - \rho) \, \mathcal{E}_c(x_c) + \rho \, \mathcal{E}_e(x_e) \qquad [\mathbf{8}]$$

where ℓ is the natural length of the fiber.

We minimize this energy under the fixed-end constraint of given global extension x:

$$x = (1 - \rho) \, x_c + \rho \, x_e \qquad [\mathbf{9}]$$

Consequently we work with the function $\mathcal{L} = \mathcal{E} - \lambda \, [(1 - \rho)x_c + \rho x_e]$ and solve for

$$(\partial \mathcal{L}/\partial x_c, \partial \mathcal{L}/\partial x_e, \partial \mathcal{L}/\partial \rho) = 0 \qquad [\mathbf{10}]$$

The Lagrange multiplier λ is easily identified with the external force T needed to enforce the constraint (9).

A first solution is $\rho = 0$, $T = \lambda = k_c \, (x - D)$, and $x_c = x$; the system is entirely in the coiled phase.

A second solution is $\rho = 1$, $T = \lambda = k_e \, (x - \ell)$, and $x_e = x$; the system is entirely in the extended phase.

A third solution is $0 < \rho < 1$, that is the system is in a mixture of phases. The tension is given by $T = \mathcal{E}'_c(x_c) = \mathcal{E}'_e(x_e) = (\mathcal{E}_e - \mathcal{E}_c)/(x_e - x_c)$ yielding

$$T = \lambda = \epsilon_0 \left(1 + \frac{\lambda^2}{2 \, \epsilon_0 \, k_c} - \frac{\lambda^2}{2 \, \epsilon_0 \, k_e} \right) \Big/ \left(1 - \frac{D}{\ell} \right) \qquad [\mathbf{11}]$$

which, as $D \ll L$ and $\epsilon_0 \ll k_e \, , k_c$, simplifies to $T \simeq \epsilon_0$.

References

1. Rainer Foelix. *Biology of spiders*. Oxford University Press, 2010.
2. Nathan Becker, Emin Oroudjev, Stephanie Mutz, Jason P. Cleveland, Paul K. Hansma, Cheryl Y. Hayashi, Dmitrii E. Makarov, and Helen G. Hansma. Molecular nanosprings in spider capture-silk threads. *Nat Mater*, 2(4):278–283, 2003.
3. Todd A. Blackledge, Adam P. Summers, and Cheryl Y. Hayashi. Gumfooted lines in black widow cobwebs and the mechanical properties of spider capture silk. *Zoology*, 108(1):41–46, 3 2005.
4. Fritz Vollrath and Donald T. Edmonds. Modulation of the mechanical properties of spider silk by coating with water. *Nature*, 340:305–307, 1989.
5. P. Schneider. Elastic properties of the viscid silk of orb weaving spiders (araneidae). *Naturwissenschaften*, 82(3):144–145, 1995.
6. F. Vollrath and D. Edmonds. Elastic properties of spider's capture silk. *Naturwissenschaften*, 82(8):379–380, 1995.
7. H.M. Peters. Ultrastructure of orb spiders' gluey capture threads. *Naturwissenschaften*, 82(8):380–382, 1995.
8. N. K. Adam. Detergent action and its relation to wetting and emulsification. *Journal of the Society of Dyers and Colourists*, 53(4):121–129, 1937.
9. David Quéré. Fluid coating on a fiber. *Annual Review of Fluid Mechanics*, 31(1):347–384, 2011/01/31 1999.
10. Brendan Joseph Carroll. Droplet formation and contact angles of liquids on mammalian hair fibres. *Journal of the Chemical Society, Faraday Transactions 1: Physical Chemistry in Condensed Phases*, 85(11):3853–3860, 1989.

11. F. Vollrath and E.K. Tillinghast. Glycoprotein glue beneath a spider web's aqueous coat. *Naturwissenschaften*, 78(12):557–559, 1991.

12. Donald T. Edmonds and Fritz Vollrath. The contribution of atmospheric water vapour to the formation and efficiency of a spider's capture web. *Proceedings of the Royal Society of London. Series B: Biological Sciences*, 248(1322):145–148, 1992.

13. P.G. de Gennes, F. Brochard-Wyart, and D. Quéré. *Capillarity and Wetting Phenomena: Drops, Bubbles, Pearls, Waves*. Springer, 2003.

14. Elise Lorenceau, Tim Senden, and David Quéré. Wetting of fibers. In R.G. Weiss and P. Terech, editors, *Molecular Gels. Materials with Self-Assembled Fibrillar Networks*, pages 223–237. Springer, 2006.

15. John F. Marko and Simona Cocco. The micromechanics of DNA. *Physics World*, pages 37–41, 2003.

16. Basile Audoly and Yves Pomeau. *Elasticity and Geometry: From hair curls to the non-linear response of shells*. Oxford University Press, 2010.

17. A. Antkowiak, B. Audoly, C. Josserand, S. Neukirch, and M. Rivetti. Instant fabrication and selection of folded structures using drop impact. *Proc. Natl Acad. Sci. U.S.A.*, 108(26):10400–10404, 2011.

18. J. E. Gordon. *Structures or why things don't fall down*. Penguin Books, 1978.

19. Amélie Leforestier and Françoise Livolant. Structure of toroidal dna collapsed inside the phage capsid. *Proceedings of the National Academy of Sciences*, 2009.

20. Philip Ball. *Shapes - Nature's Patterns: A Tapestry in Three Parts*. Oxford University Press, 2009.

21. A. Lazarus, H. C. B. Florijn, and P. M. Reis. Geometry-induced rigidity in nonspherical pressurized elastic shells. *Phys. Rev. Lett.*, 109:144301, Oct 2012.

22. K Krieger. Buckling down. *Nature*, 488(7410):146–147, 2012.

23. F Jacob. Evolution and tinkering. *Science*, 196(4295):1161–1166, 1977.

Coiling of an elastic beam inside a disk: A model for spider-capture silk

Hervé Elettro [a,b], Fritz Vollrath [c], Arnaud Antkowiak [a,b], Sébastien Neukirch [a,b,*]

[a] Centre National de la Recherche Scientifique, UMR 7190, Institut Jean Le Rond d'Alembert, F-75005 Paris, France
[b] Sorbonne Universités, UPMC Univ Paris 06, UMR 7190, Institut Jean Le Rond d'Alembert, F-75005 Paris, France
[c] Oxford Silk Group, Zoology Department, University of Oxford, UK

ABSTRACT

Motivated by recent experimental observations of capillary-induced spooling of fibers inside droplets both in spider capture silk and in synthetic systems, we investigate the behavior of a fiber packed in a drop. Using a simplified 2D model, we provide analytical predictions for the buckling threshold and the deep post-buckling asymptotic behavior. The threshold for spooling is found to be in particularly good agreement with experimental results. We further solve the Elastica equations for a fiber confined in a soft potential, and track the equilibrium paths using numerical continuation techniques. A wealth of different paths corresponding to different symmetries is uncovered, and their stability is finally discussed.

© 2015 Elsevier Ltd. All rights reserved.

1. Introduction

The mechanical properties of spider silk are often presented as outstanding [1,2]. An indeed, most silk threads outperform the best man-made fibers, such a Kevlar, at least in terms of toughness [3]. To a large extent, these properties rely on the molecular architecture of the silk. For example, it has been shown that the building blocks of flagelliform silk involve molecular nanosprings [4]. In 1989 however, a team comprising a zoologist and a physicist reported on coiling and packing of the core filament inside a glue droplet [5]. This *windlass mechanism*, as it was called, provided indirect evidence that the glue droplets may as well play a role in the mechanical response of the silk thread. These results have been a subject of debate in the community, and it is only very recently that the mechanism has been observed to be active in a real spider web, see Fig. 1 (left) [6]. A natural question that arises in this context is the role played by the molecular structure of the silk and the glue in the observed coiling. An experimental answer to this question is provided in Fig. 1 (right), where a micron-sized artificial thread bearing a silicon oil droplet also exhibits the coiling mechanism and packing behavior, therefore demonstrating that capillarity and elasticity are sufficient ingredients to explain the mechanism.

Interestingly, the shape adopted by the filament inside the drop can be as different as a perfectly ordered closely packed annular bundle or a completely disordered tangle. This behavior is

reminiscent of the organization of packed wires in rigid [7] and elastic [8] spherical shells, patterns of folded structures such as plant leaves or crumpled paper [9,10], and DNA packing inside capsids [11–13]. The purpose of the present paper is to explore theoretically in a simplified setting the shape and stability of strongly post-buckled states in order to lay down the basis for a deeper understanding of the windlass mechanism.

The paper is organized as follows. In Section 2 we present the problem and the equilibrium equations. In Section 3 we perform a linear stability analysis of the straight beam and predict the buckling threshold. Experimental results are confronted to theoretical in Section 4. Finally, we describe the non-linear response of the system in terms of equilibrium solutions and their stability in Section 5.

2. Model

We consider an elastic beam in interaction with a liquid disk and under the action of a tensile end-load. As indicated in Fig. 2, we restrict to planar deformations of the beam, X and Y denoting the horizontal and vertical directions respectively. The beam has length L and a circular cross-section of radius h. We work under the slender ($L \gg h$) Euler–Bernoulli hypotheses where the beam is considered inextensible and unshearable. Configurations are thus fully described by the position and orientation of the centerline. We use the arc-length $S \in [0, L]$ and note $\theta(S)$ the angle between the tangent of the beam and the horizontal. The presence of the liquid disk generates capillary forces due to the contrast of surface energy, the interaction

Fig. 1. Experiments on fibers bent inside liquid drops. *Left*: microscopic photograph of spider capture silk. Flagelliform core filaments are seen to be coiled and packed inside a (typically 300μ wide) glue droplet. *Right*: same mechanism reproduced artificially with a 200 μm synthetic droplet and fiber (see experimental verification section in Section 4). Reproduced from [6].
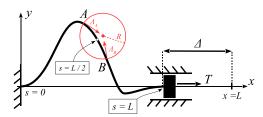

Fig. 2. An elastic beam held in tension at its extremities, and buckling under the action of compressive forces at a disk. The beam is clamped at both ends. The deformation of the beam is described by the angle $\theta(S)$ between the tangent to the beam and the x-axis, where $S \in [0, L]$ is the arc-length along the beam.

energy of the beam with the liquid being smaller than the interaction energy of the beam with the air. Capillary forces are two-fold: (i) meniscus forces applied on the beam at the entrance and exit of the disk, and (ii) barrier forces that prevent the beam from exiting the disk elsewhere than at the meniscus points. We consider that the drop is undeformable and thus remains a disk throughout the experiments. As shown in Appendix A, meniscus forces are pointing toward the center of the disk (see Eqs. (A.15) and (A.18)) and their intensity is related to the angle between their direction and the tangent to the beam at the meniscus points (see Eq. (A.25)). A soft-wall barrier potential [14]

$$V(X,Y) = \frac{V_0}{1 + \rho - (1/R)\sqrt{(X-X_C)^2 + (Y-Y_C)^2}} \tag{1}$$

is used to retain the beam inside the disk, centered on (X_C, Y_C) and of radius R. The small dimensionless parameter ρ is introduced to avoid the potential to diverge at the meniscus points A and B, where the rod enters and exits the disk. The intensity V_0 of the potential is chosen to be small, the hard-wall limit being $V_0 \to 0$. Kinematics, relating the position (X,Y) of the rod and the inclination θ of its tangent ($\cos\theta, \sin\theta$) with the horizontal, the bending constitutive relation, relating the curvature $\theta'(S)$ to the moment $M(S)$, and finally force (N_x, N_y) and moment balance are detailed in Appendix A and read

$$X'(S) = \cos\theta, \quad Y'(S) = \sin\theta \tag{2a}$$

$$EI\theta'(S) = M, \quad M'(S) = N_x \sin\theta - N_y \cos\theta \tag{2b}$$

$$N_x'(S) = \chi \frac{\partial V}{\partial X} + \delta(S-S_A)\Lambda_A \frac{X_A - X_C}{R} + \delta(S-S_B)\Lambda_B \frac{X_B - X_C}{R} \tag{2c}$$

$$N_y'(S) = \chi \frac{\partial V}{\partial Y} + \delta(S-S_A)\Lambda_A \frac{Y_A - Y_C}{R} + \delta(S-S_B)\Lambda_B \frac{Y_B - Y_C}{R} \tag{2d}$$

where S is the arc-length along the rod, and $(\ )' = d(\ )/dS$. We define the coordinates of point A as $(X_A, Y_A) = (X(S_A), Y(S_A))$, same for point B. Note that the potential V has the dimension of an energy per unit of arc-length of the beam. For $S \in [S_A; S_B]$ the rod lies inside the disk and we have $\chi = 1$, otherwise $\chi = 0$. The Dirac distribution $\delta(S)$ localizes meniscus forces at points A and B. The rod material has Young's modulus E and the second moment of area $I = \pi h^4/4$. The intensities Λ_A and Λ_B of the meniscus forces are unknown but related to surface tension γ_{LV} through Eq. (A.25), where $F_\gamma = 2\pi h\gamma_{LV} \cos\alpha_Y$ with α_Y

being the Young–Dupré wetting angle ($\gamma_{SV} - \gamma_{SL} = \gamma_{LV} \cos\alpha_Y$), and where $V_A = V_B = V_0/\rho$ are small compared to F_γ. We restrict ourself to cases where the disk is centered on the mid-point of the rod, that is we introduce Σ such that $S_A = L/2 - \Sigma$ and $S_B = L/2 + \Sigma$. The rod has then 2Σ of its arc-length spent inside the disk. Finally the external applied tension is noted $T = N_x(L)$.

2.1. Non-dimensionalization

We use the diameter $D = 2R$ of the disk as unit length, and the buckling load EI/D^2 as unit force. We thus introduce the following dimensionless quantities:

$$s = \frac{S}{D}; \quad \sigma = \frac{\Sigma}{D}; \quad \ell = \frac{L}{D}; \quad (x,y) = \frac{(X,Y)}{D}; \quad n = \frac{ND^2}{EI}; \quad t = \frac{TD^2}{EI} \tag{3a}$$

$$f_\gamma = \frac{F_\gamma D^2}{EI}; \quad m = \frac{MD}{EI}; \quad \lambda_{A,B} = \frac{\Lambda_{A,B}D^2}{EI}; \quad (v,v_0) = \frac{(V,V_0)D^2}{EI} \tag{3b}$$

and $\delta(s) = D\delta(S)$. We then have

$$v(x,y) = v_0\left(1 + \rho - 2\sqrt{(x-x_C)^2 + (y-y_C)^2}\right)^{-1} \text{ and}$$

$$x'(s) = \cos\theta, \quad y'(s) = \sin\theta \tag{4a}$$

$$\theta'(s) = m, \quad m'(s) = n_x \sin\theta - n_y \cos\theta \tag{4b}$$

$$n_x'(s) = \chi \frac{\partial v}{\partial x} + 2\delta(s-s_A)\lambda_A(x_A - x_C) + 2\delta(s-s_B)\lambda_B(x_B - x_C) \tag{4c}$$

$$n_y'(s) = \chi \frac{\partial v}{\partial y} + 2\delta(s-s_A)\lambda_A(y_A - y_C) + 2\delta(s-s_B)\lambda_B(y_B - y_C) \tag{4d}$$

where $(\ )' = d(\ )/ds$, and $s_A = \ell/2 - \sigma$, $s_B = \ell/2 + \sigma$.

2.2. Boundary-value problem

We consider v_0, ρ, f_γ, and ℓ as fixed parameters and we look for equilibrium solutions by integrating (4) with the initial conditions

$$x(0) = 0; \quad y(0) = 0; \quad \theta(0) = 0; \quad m(0) = m_0; \quad n_x(0) = n_{x0};$$

$$n_y(0) = n_{y0} \tag{5}$$

where m_0, n_{x0}, and n_{y0} are unknowns to be accompanied with σ, x_C, y_C, λ_A, and λ_B. We therefore have eight unknowns which are balanced by the following seven conditions. At the $s = \ell$ end of the rod, clamped boundary conditions read

$$y(\ell) = 0; \quad \theta(\ell) = 0 \tag{6}$$

The requirement that points A and B lie on the circle yields the conditions

$$[x_A - x_C]^2 + [y_A - y_C]^2 = 1/4; \quad [x_B - x_C]^2 + [y_B - y_C]^2 = 1/4 \tag{7}$$
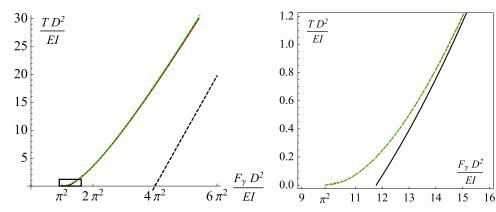
Fig. 3. Buckling curve for $\ell = 5$. (Left) Curves defined by Eqs. (11)–(13). At this scale the three curves are almost indistinguishable. The asymptote $t = f_\gamma - 4\pi^2$ is shown dashed. (Right) Zoom corresponding to the rectangle shown on the Left. The approximations (12) and (13) are still hard to distinguish, but are seen to deviate from the exact curve (11), shown continuous and black.

and the three force balances related to forces coming from the disk read

$$n_x(s_A^-) = n_x(s_B^+) \tag{8a}$$

$$n_y(s_A^-) = n_y(s_B^+) \tag{8b}$$

$$-2f_\gamma + v_A + v_B - 2\lambda_A[(x_A - x_C)\cos\theta(s_A) + (y_A - y_C)\sin\theta(s_A)] \\ + 2\lambda_B[(x_B - x_C)\cos\theta(s_B) + (y_B - y_C)\sin\theta(s_B)] = 0 \tag{8c}$$

The solution set is thus a $8 - 7 = 1$ dimensional manifold and we plot in Section 5 different solution paths for several values of the parameter f_γ.

3. Buckling threshold

The trivial solution $x(s) = s$, $y(s) = \theta(s) = m(s) = n_y(s) = 0$ to Eq. (4) with boundary conditions (5)–(8), exists for any value of the load t. Nevertheless, for given values of the parameters v_0, ρ, f_γ, and ℓ, there is a threshold value of t under which the trivial solution ceases to be stable and buckling occurs. We look for the first buckling mode which is symmetrical with respect to the axis joining the center of the disk (x_C, y_C) and the beam midpoint $(x(\ell/2), y(\ell/2))$. We linearize Eqs. (4) for small deflections, $|y(s)| \sim \epsilon$, and small slopes, $|\theta(s)| \sim \epsilon$, with $0 < \epsilon \ll 1$, see Appendix B for a comprehensive exposition of this perturbation expansion. As in the buckling configuration the rod has virtually no packing interaction with the disk, we set $v_0 = 0$. The first four equations of system (4) become $x'(s) = 1$, $y'(s) = \theta(s)$, $\theta'(s) = m(s)$, and $m'(s) = n_x(s)\theta(s) - n_y(s)$. We then have $x_C = \ell/2$, $x_A = \ell/2 - \sigma$, and $x_B = \ell/2 + \sigma$. At order ϵ^0, Eq. (7) yields $\sigma = 1/2$. As symmetry imposes $y_A = y_B$ and $\theta(s_A) = -\theta(s_B)$, Eq. (7) at order ϵ^2 imposes $y_C = y_A = y_B$. Then (8c) at order ϵ^0 yields $2f_\gamma = \lambda_A + \lambda_B$ and, as symmetry requires $\lambda_A = \lambda_B$, we finally obtain $f_\gamma = \lambda_A = \lambda_B$. Following symmetry we introduce $\hat{s} = s - \ell/2$. The three functions $y(\hat{s})$, $\theta(\hat{s})$, and $m(\hat{s})$ are then respectively even, odd, and even functions of the variable $\hat{s}$. We focus on the right half of the system, $\hat{s} \in [0; \ell/2]$. Eq. (4c) is integrated to yield $n_x(\hat{s}) = t - f_\gamma$ for $\hat{s} \in [0; 1/2]$ and $n_x(\hat{s}) = t$ for $\hat{s} \in [1/2; \ell/2]$. Eq. (4d) shows that $n_y(\hat{s}) = $ const. and from $m'(\hat{s}) = n_x(\hat{s})\theta(\hat{s}) - n_y(\hat{s})$ we see that $n_y(\hat{s})$ has to be odd, hence zero. We finally arrive at the reduced system

$$\theta'' = -(f_\gamma - t)\theta \quad \text{for } \hat{s} \in [0; 1/2] \tag{9}$$

$$\theta'' = t\theta \quad \text{for } \hat{s} \in [1/2; \ell/2] \tag{10}$$

and we restrict to the $f_\gamma > t \geq 0$ case. Integrating these equations and using the boundary conditions $\theta(\hat{s} = 0) = 0 = \theta(\hat{s} = \ell/2)$ and the matching conditions $\theta(\hat{s} = 1/2^-) = \theta(\hat{s} = 1/2^+)$ and $m(\hat{s} =$
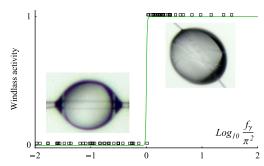

Fig. 4. Experimental verification of the windlass activation as function of the parameter f_γ. The windlass mechanism is active as soon as the meniscus force f_γ is greater than π^2.

$1/2^-) = m(\hat{s} = 1/2^+)$, we obtain the buckling condition

$$\sqrt{f_\gamma - t}\,\tanh\frac{(\ell-1)\sqrt{t}}{2} + \sqrt{t}\,\tan\frac{\sqrt{f_\gamma - t}}{2} = 0 \tag{11}$$

which is plotted in Fig. 3. The two interesting asymptotic limits of the curve defined by (11) are (i) if $t \to 0$ then $f_\gamma \to \pi^2 + 8/\ell$, and (ii) if $f_\gamma \to +\infty$ then $t \to f_\gamma - 4\pi^2$.

3.1. Approximations to the buckling load

In the case where $\ell \ll 1$, we simplify Eq. (11) and find

$$\sqrt{f_\gamma - t} + \sqrt{t}\,\tan\frac{\sqrt{f_\gamma - t}}{2} = 0 \tag{12}$$

This formula has the same large f_γ limit as (11) and in fact as $\ell \to +\infty$, the curve defined by (11) tends to the curve defined by (12) everywhere but in a boundary layer around $(f_\gamma, t) = (\pi^2, 0)$. Indeed even if ℓ is large, for small t the tanh term cannot be approximated by 1 if $t \sim 1/\ell^2$. It is convenient to have an explicit formula $t = t(f_\gamma)$ for buckling and we introduce the approximation

$$t_b(f_\gamma) = f_\gamma - 4\pi^2 - \frac{108\pi^4}{3\pi^4 - 40\pi^2 + (3\pi^2 - 28)f_\gamma + (32\pi - 6\pi^3)\sqrt{f_\gamma}} \tag{13}$$

This last formula has the same behavior as (12) at low t: we have $t_b(f_\gamma = \pi^2) = 0$, and $t'_b(f_\gamma = \pi^2) = 0$. Moreover (13) also shares the large f_γ limit of (11) and (12): $t_b = -4\pi^2 + f_\gamma + \cdots$. We see in Fig. 3 that the curves defined by (12) and (13) are in fact hard to distinguish.

4. Experimental verification

In order to verify experimentally and quantitatively the mechanics of the windlass, we place a drop on a fiber and test whether the fibre coils in the drop. The fibre is made of BASF Thermoplastic PolyUrethan (TPU) that is melt-spinned. This process involves melting down the TPU, then applying a large extension rate to the liquid filament while it cools down rapidly in the ambient air. It results in reproducible, meter-long micronic fibres (1–20 μm in radius) with portions away from the edges having small perturbations in radius (typically $< 5\%$ every 1000 radii). Calipers are used to further manipulate the samples. Clamping is achieved with cured Loctite[®] glue. The system size is measured optically with a Leica macroscope (VZ85RC) mounted on a micro-step motor and a 3 megapixels Leica

DFC-295 camera (400× magnification, 334 nm/pixel picture resolution) with a Phlox 50 × 50 mm backlight, at 60,000 lux or alternatively an optical fibre with LED lamp (Moritex MHF-M1002) with circular polarizer. The fibre radius is then extracted by image analysis, using imageJ (http://imagej.nih.gov/ij/). For the droplet, we select silicone oil Rhodorsil 47V1000, the figure 1000 referring to its viscosity compared to water. High viscosity was chosen in order to be able to deposit drops on the fibre by brushing, and for its slow evaporation properties. Using the condition that meniscus forces have to support the weight of the droplet and be strong enough to buckle the beam, we find that to be bendable, a TPU fibre must be below 7.2 μm in radius, with $E_{TPU} = 17 \pm 3$ MPa, $\gamma_{silicone–oil/air} = 21.1$ mN/m, $\alpha_{Y,silicone–oil/TPU} = 27 \pm 5°$ and $\rho_{silicone–oil} = 960$ kg/m^3 the silicone oil density.
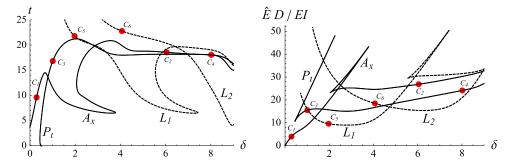
Fig. 5. Post-buckling paths: (*left*) force–displacement curves for $f_\gamma = 20$, where t is the applied tension and δ the end-shortening, and (*right*) energy $\hat{E}$ as function of δ. Solid lines represents both *Ax* configurations, where the beam shape is symmetric with respect to the axis joining the center of the disk (x_C, y_C) and the beam midpoint $(x(\ell/2), y(\ell/2))$, and *Pt* configurations, where the beam shape is symmetric with respect to the beam midpoint *Pt*. Dashed lines correspond to L_1 and L_2 configurations.
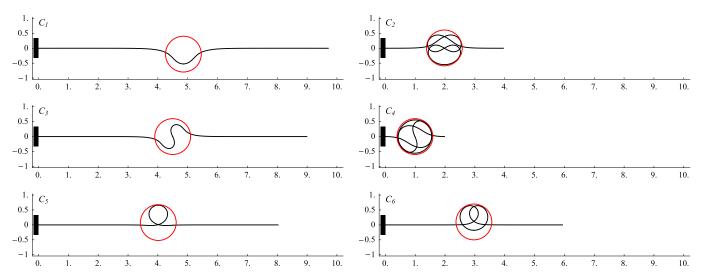
Fig. 6. Post-buckling configurations. Top row shows *Ax* configurations, symmetric with respect to the axis joining the center of the disk (x_C, y_C) and the beam midpoint $(x(\ell/2), y(\ell/2))$. Middle row shows *Pt* configurations, symmetric with respect to the beam midpoint *Pt*. Bottom row represents L_1 and L_2 configurations. The circles have center (x_C, y_C) and radius $(1+\rho)/2$.
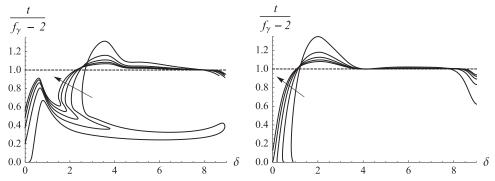
Fig. 7. Equilibrium paths for $f_\gamma = 10, 20, \dots, 50$ with the vertical axis rescaled according to Eq. (14). (Left) Axis-symmetric (*Ax*) configurations and (right) point-symmetric (*Pt*) configurations. Direction of increasing f_γ is indicated with the arrows.

We deposit a drop on a fibre with a known radius and we slowly bring the caliper forks closer to impose compression on the fibre. If the drop is able to coil the fibre, the macroscopic consequences are easily visible to the naked eye. If at first try the drop does not coil, the sample is tested again with a random compression and a slight shake to overcome any possible metastability. The couple drop/fiber is given an activity index of 1 if coiling is achieved and 0 otherwise (see Fig. 4). The experimental results show that coiling is present whenever $f_\gamma > \pi^2$, with a error of margin of 3%, consistent with Eq. (11).

5. Non-linear post-buckling computations

5.1. Equilibrium paths

We now analyze the post-buckling regime by numerically solving the non-linear system of equilibrium equations. We use a shooting method to solve the boundary-value problem (4)–(8) and a pseudo-arc-length continuation algorithm to follow the solution as parameters are varied, both these routines being implemented in Mathematica. For large f_γ values, typically $f_\gamma > 15$, numerical difficulties arise and we thankfully switch to the AUTO package [15]. We fix $\ell = 10$, $\nu_0 = 0.02$, $\rho = 0.2$, and we compute force-extension bifurcation diagrams for several values of f_γ. We show in Fig. 5 such a diagram for $f_\gamma = 20$ where the tension t is plotted as a function of the end-shortening $\delta = \ell - x(\ell)$. The diagram comprises four different equilibrium paths: (i) path *Ax* where configurations are symmetric with respect to the axis joining the center of the disk (x_C, y_C) and the beam midpoint $(x(\ell/2), y(\ell/2))$, (ii) path *Pt* where configurations are symmetric with respect to the beam midpoint, (iii) path L_1 where configurations are looping once inside the disk, and (iv) path L_2 where configurations are looping twice inside the disk. Few of these configurations are shown in Fig. 6. In a typical experiment the system is first completely straight, held by a large tension t. This situation corresponds to a point on the vertical axis of Fig. 5, above the buckling threshold. As t is decreased the systems reach the start of the *Ax* path, and the beam buckles. For $f_\gamma = 20$, the numerically found value of the buckling tension $t \simeq 3.66$ is to be compared to $t_b(20) \simeq 3.76$ given by (13), and $t \simeq 3.73$ given by (11). As the system branches on the *Ax* path, tension goes up again – we have a subcritical bifurcation. The slope of the *Ax* path is calculated analytically in Appendix B and is plotted in Fig. B1 for comparison. As the beam enters deeper in the post-buckling regime, bending localizes inside the disk and the tails remain approximatively straight. The path eventually reaches a plateau, see formula (14), where the beam coils in a circular way inside the disk and the bending energy in the beam can then be approximated by $(1/2)EI/R^2[L - X(L)]$. We also plot the $t > 0$ part of the path *Pt*. This path also reaches the same plateau as the beam coils in the same circular way inside the disk. In addition we plot paths along which the beam adopts configurations with one (path L_1) or two (path L_2) loops. The relevance of these paths could be questioned for two reasons: (i) configuration on path L_1 do not have the same topology as far as twist is considered: a full turn of twist would be necessary to connect configurations on path *Ax* or *Pt* with configurations on path L_1, see [16,17], and (ii) these paths are not connected to the vertical axis $\delta = 0$. We plot in Fig. 5 (right) the energy $\hat{E} = E_\kappa + E_w + E_\gamma - P\gamma_{SV}L + F_\gamma(\Delta + D)$ as a function of the end-shortening δ and we see that, for some range of the end-shortening δ, configurations on paths L_1 or L_2 have a lower energy than configurations on paths *Ax* or *Pt*. These remarks call for a stability analysis of the equilibrium configurations, as well as a study of configurations deformed in 3D, where twist, link, and writhe would be computed [18].

5.2. Approximate analytical model for the plateau regime

As explained in [6], in the regime where the end-shortening $\delta = \ell - x(\ell)$ is large, that is when several coils of the beam are present in the disk, the external tension t reaches a plateau and no longer varies as more coils are added. The plateau value of the tension is calculated by a balance of energy as a beam length ΔS enters the disk. The work done by the tension T is $-T\Delta S$, the work done by the meniscus force F_γ is $+F_\gamma\Delta S$, and the energy spent to bend the beam in coils is $-(1/2)(EI/R^2)\Delta S$. The sum of these energies is zero on the plateau, which yields

$$t = f_\gamma - 2 \qquad (14)$$

in dimensionless quantities. In Fig. 7 we plot *Ax* and *Pt* equilibrium paths for $f_\gamma = 10, 20, \ldots, 50$ with the vertical axis rescaled according to (14). The collapse of the curves for $\delta \gtrsim 4$ confirms relation (14).

6. Conclusion

This paper presents a first venture into the complex equilibria adopted by a fiber buckled, coiled, and packed by a droplet. Using a simple 2D model and numerical continuation techniques, we have uncovered several equilibrium paths characterized by different symmetries (point-symmetric, axis-symmetric, single or double-looped) and provided clues for the bifurcations between these different states. Analytical predictions for the buckling threshold, as well as the asymptotic behavior (plateau regime) for the deep post-buckling regime have been derived. The agreement between experiments and theory for the windlass activation threshold is certainly promising, and calls for an extension of the present model to 3D (including twist and writhe), and a deeper comparison between the experimentally observed ordered and disordered packing modes and the theoretical prediction. Finally the deformation of the drop on its own, considered rigid throughout this study, and its interplay with the shape adopted by the fiber also deserves a dedicated investigation.

Appendix A. Variational derivation of the equilibrium equations

To prevent the beam from exiting the disk elsewhere than at the meniscus points, we use a (soft wall) barrier potential [14]

$$V(X, Y) = \frac{V_0}{1 + \rho - (1/R)\sqrt{(X - X_C)^2 + (Y - Y_C)^2}} \qquad (A.1)$$

where the disk has center (X_C, Y_C) and radius R. The small dimensionless parameter ρ is introduced to avoid the potential to diverge at the meniscus points A and B, where the rod enters and exits the disk. The internal energy of the system comprises the bending energy E_b of the rod, the barrier energy E_w of the circle,

and surface energy E_γ

$$E_\kappa = \frac{1}{2}EI\int_0^{S_A}\kappa_1^2\,dS + \frac{1}{2}EI\int_{S_A}^{S_B}\kappa_2^2\,dS + \frac{1}{2}EI\int_{S_B}^L\kappa_3^2\,dS \tag{A.2a}$$

$$E_w = \int_{S_A}^{S_B}V(X(S),Y(S),X_C,Y_C)\,dS \tag{A.2b}$$

$$E_\gamma = P\gamma_{SV}S_A + P\gamma_{SL}(S_B - S_A) + P\gamma_{SV}(L - S_B) \tag{A.2c}$$

where $P = 2\pi h$ is the perimeter of the cross-section of the rod, and V_0 has the dimension of an energy per unit length. The curvatures $\kappa_i(S)$ are defined in each region of the rod. We add the work done by the external load Te_x and obtain the potential energy of the system

$$E_\kappa + E_w + E_\gamma - TX(L) \tag{A.3}$$

We minimize this energy under the following constraints:

$$\frac{S_A + S_B}{2} = \frac{L}{2} \tag{A.4a}$$

$$[X(S_A) - X_C]^2 + [Y(S_A) - Y_C]^2 = R^2 \tag{A.4b}$$

$$[X(S_B) - X_C]^2 + [Y(S_B) - Y_C]^2 = R^2 \tag{A.4c}$$

Eq. (A.4a) imposes that the capturing disk is centered on the midpoint of the rod. We introduce Σ such that $S_A = L/2 - \Sigma$ and $S_B = L/2 + \Sigma$. The rod has then 2Σ of its arc-length spent in the disk. As the variables $X(S)$, $Y(S)$, $\kappa(S)$ and $\theta(S)$ all appear in the formulation, we have to consider the continuous constraints relating them:

$$X'(S) = \cos\theta(S), \quad Y'(S) = \sin\theta(S), \quad \theta'(S) = \kappa(S) \tag{A.5}$$

We consequently write the Lagrangian

$$\begin{aligned}
\mathcal{L}&(X,Y,\theta,\kappa_1,\kappa_2,\kappa_3,X_C,Y_C,\Sigma)\\
&= -TX(L) + \int_0^{L/2-\Sigma}\left(\frac{EI}{2}\kappa_1^2 + P\gamma_{SV} + \nu_1(S)[X' - \cos\theta] + \mu_1(S)\right.\\
&\quad \left.\times[Y' - \sin\theta] + \eta_1(S)[\theta' - \kappa_1]\right)dS\\
&\quad + \int_{L/2-\Sigma}^{L/2+\Sigma}\left(\frac{EI}{2}\kappa_2^2 + P\gamma_{SL} + \nu_2(S)[X' - \cos\theta]\right.\\
&\quad \left. + \mu_2(S)[Y' - \sin\theta] + \eta_2(S)[\theta' - \kappa_2] + V(X,Y,X_C,Y_C)\right)dS\\
&\quad + \int_{L/2+\Sigma}^L\left(\frac{EI}{2}\kappa_3^2 + P\gamma_{SV} + \nu_3(S)[X' - \cos\theta]\right.\\
&\quad \left. + \mu_3(S)[Y' - \sin\theta] + \eta_3(S)[\theta' - \kappa_3]\right)dS\\
&\quad + \frac{\Lambda_A}{2R}([X(L/2-\Sigma) - X_C]^2 + [Y(L/2-\Sigma) - Y_C]^2 - R^2)\\
&\quad + \frac{\Lambda_B}{2R}([X(L/2+\Sigma) - X_C]^2 + [Y(L/2+\Sigma) - Y_C]^2 - R^2)
\end{aligned} \tag{A.6}$$

The rod is clamped as both extremities, boundary conditions read

$$X(0) = 0, \quad Y(0) = 0, \quad \theta(0) = 0, \quad Y(L) = 0, \quad \theta(L) = 0 \tag{A.7}$$

A.1. First variation

We note $\boldsymbol{U} = (X,Y,\theta,\kappa_1,\kappa_2,\kappa_3,X_C,Y_C,\Sigma)$ and we consider the conditions for the state $\boldsymbol{U}_e$ to minimize the energy E. Calculus of variations shows that a necessary condition is

$$\mathcal{L}'(\boldsymbol{U}_e)\overline{\boldsymbol{U}} = \frac{d}{d\epsilon}\mathcal{L}(\boldsymbol{U}_e + \epsilon\overline{\boldsymbol{U}})\Big|_{\epsilon=0} = 0 \tag{A.8}$$

where $\overline{\boldsymbol{U}} = (\overline{X},\overline{Y},\overline{\theta},\overline{\kappa}_1,\overline{\kappa}_2,\overline{\kappa}_3,\overline{X}_C,\overline{Y}_C,\overline{\Sigma})$. The bar ‾ sign represents a small perturbation of the variable. Moreover boundary conditions (A.7) imply that

$$\overline{X}(0) = 0, \quad \overline{Y}(0) = 0, \quad \overline{\theta}(0) = 0, \quad \overline{Y}(L) = 0, \quad \overline{\theta}(L) = 0 \tag{A.9}$$

Noting that $\int_0^{A+\epsilon\overline{A}}f(x)\,dx = \int_0^A f(x)\,dx + \epsilon\overline{A}f(A) + O(\epsilon^2)$ we evaluate the first variation (A.8)

$$\begin{aligned}
\mathcal{L}'&(U_e)(\overline{U}) = -T\overline{X}(L) - 2F_\gamma\overline{\Sigma} + V_A\overline{\Sigma} + V_B\overline{\Sigma}\\
&+ \int_0^{L/2-\Sigma}(EI\overline{\kappa}_1\kappa_1 + \nu_1(S)[\overline{X}' + \overline{\theta}\sin\theta] + \mu_1(S)[\overline{Y}' - \overline{\theta}\cos\theta]\\
&+ \eta_1(S)[\overline{\theta}' - \overline{\kappa}_1])\,dS\\
&+ \int_{L/2-\Sigma}^{L/2+\Sigma}(EI\overline{\kappa}_2\kappa_2 + \nu_2(S)[\overline{X}' + \overline{\theta}\sin\theta]\\
&+ \mu_2(S)[\overline{Y}' - \overline{\theta}\cos\theta] + \eta_2(S)[\overline{\theta}' - \overline{\kappa}_2] + \overline{V})\,dS\\
&\int_{L/2+\Sigma}^L(EI\overline{\kappa}_3\kappa_3 + \nu_3(S)[\overline{X}' + \overline{\theta}\sin\theta]\\
&+ \mu_3(S)[\overline{Y}' - \overline{\theta}\cos\theta] + \eta_3(S)[\overline{\theta}' - \overline{\kappa}_3])\,dS\\
&+ \frac{\Lambda_A}{R}[X(L/2-\Sigma) - X_C][\overline{X}(L/2-\Sigma) - \overline{\Sigma}X'(L/2-\Sigma) - \overline{X}_C]\\
&+ \frac{\Lambda_A}{R}[Y(L/2-\Sigma) - Y_C][\overline{Y}(L/2-\Sigma) - \overline{\Sigma}Y'(L/2-\Sigma) - \overline{Y}_C]\\
&+ \frac{\Lambda_B}{R}[X(L/2+\Sigma) - X_C][\overline{X}(L/2+\Sigma) + \overline{\Sigma}X'(L/2+\Sigma) - \overline{X}_C]\\
&+ \frac{\Lambda_B}{R}[Y(L/2+\Sigma) - Y_C][\overline{Y}(L/2+\Sigma) + \overline{\Sigma}Y'(L/2+\Sigma) - \overline{Y}_C]
\end{aligned} \tag{A.10}$$

where $F_\gamma = P(\gamma_{SV} - \gamma_{SL})$, $V_A = V(X(S_A),Y(S_A))$, $V_B = V(X(S_B),Y(S_B))$, and $\overline{V} = (\partial V/\partial X)\overline{X} + (\partial V/\partial Y)\overline{Y} + (\partial V/\partial X_C)\overline{X}_C + (\partial V/\partial Y_C)\overline{Y}_C$. Note also that we have used (A.5) at $S = L/2 \pm \Sigma$ to eliminate several terms. Requiring (A.10) to vanish for all $\overline{\kappa}_i$, $i = 1,2,3$, we obtain

$$EI\kappa_i(S) = \eta_i(S), \quad i = 1,2,3 \tag{A.11}$$

and hence identify the Lagrange multipliers $\eta_i(S)$ with the bending moment $M(S)$ in the beam. Requiring (A.10) to vanish for all $\overline{\theta}$ yields, after integration by parts

$$\begin{aligned}
&[\eta_1(S)\overline{\theta}]_0^{L/2-\Sigma} + \int_0^{L/2-\Sigma}(\nu_1(S)\sin\theta - \mu_1(S)\cos\theta - \eta_1'(S))\overline{\theta}\,dS\\
&+ [\eta_2(S)\overline{\theta}]_{L/2-\Sigma}^{L/2+\Sigma} + \int_{L/2-\Sigma}^{L/2+\Sigma}(\nu_2(S)\sin\theta - \mu_2(S)\cos\theta - \eta_2'(S))\overline{\theta}\,dS\\
&+ [\eta_3(S)\overline{\theta}]_{L/2+\Sigma}^L + \int_{L/2+\Sigma}^L(\nu_3(S)\sin\theta - \mu_3(S)\cos\theta - \eta_3'(S))\overline{\theta}\,dS = 0
\end{aligned} \tag{A.12}$$

Due to the boundary conditions (A.9), part of the boundary terms vanish. Nevertheless, arbitrariness of $\overline{\theta}$ at $S = L/2 \pm \Sigma$ implies that $\eta_1(L/2-\Sigma) = \eta_2(L/2-\Sigma)$ and $\eta_2(L/2+\Sigma) = \eta_3(L/2+\Sigma)$: the bending moment is continuous at the entry and the exit of the disk. Moreover, from the requirement that (A.1) vanishes for all $\overline{\theta}(S)$, we obtain the equations for the equilibrium of the bending moment

$$\eta_i'(S) = M'(S) = \nu_i(S)\sin\theta - \mu_i(S)\cos\theta, \quad i = 1,2,3 \tag{A.13}$$

Requiring (A.10) to vanish for all $\overline{X}$ yields, after integration by parts

$$\begin{aligned}
&\frac{\Lambda_A}{R}[X(L/2-\Sigma) - X_C]\overline{X}(L/2-\Sigma) + [\nu_1(S)\overline{X}]_0^{L/2-\Sigma}\\
&- \int_0^{L/2-\Sigma}\nu_1'(S)\overline{X}\,dS - T\overline{X}(L)\\
&+ [\nu_2(S)\overline{X}]_{L/2-\Sigma}^{L/2+\Sigma} + \int_{L/2-\Sigma}^{L/2+\Sigma}\left[\frac{\partial V}{\partial X} - \nu_2'(S)\right]\overline{X}\,dS\\
&+ \frac{\Lambda_B}{R}[X(L/2+\Sigma) - X_C]\overline{X}(L/2+\Sigma)\\
&+ [\nu_3(S)\overline{X}]_{L/2+\Sigma}^L - \int_{L/2+\Sigma}^L\nu_3'(S)\overline{X}\,dS = 0
\end{aligned} \tag{A.14}$$

Boundary conditions (A.9) cancel part of the boundary terms, but arbitrariness of $\overline{X}$ at $S = L/2 \pm \Sigma$ implies

$$\nu_2(L/2-\Sigma) - \nu_1(L/2-\Sigma) = \frac{\Lambda_A}{R}[X(L/2-\Sigma) - X_C] \tag{A.15a}$$

$$\nu_3(L/2+\Sigma)-\nu_2(L/2+\Sigma)=\frac{\Lambda_B}{R}[X(L/2+\Sigma)-X_C] \tag{A.15b}$$

while arbitrariness of $\overline{X}$ at $S=L$ implies

$$\nu_3(L)=T \tag{A.16}$$

Eq. (A.16) enable us to identify ν_3 and therefore ν_1 and ν_2 with the x-component, N_x, of the resultant force in the beam. By extension the μ_i are identified to the y-component, N_y, of this force. Eqs. (A.15) are then seen as jumps in the x-component of the internal force due to the external force coming from the disk. Moreover, from the requirement that (A.14) vanishes for all $\overline{X}(S)$, we obtain the equilibrium equations for the x-component of the resultant force in the beam

$$\nu'_1(S)=0, \quad \nu'_2(S)=\frac{\partial V}{\partial X}, \quad \nu'_3(S)=0 \tag{A.17}$$

The same procedure for the variable Y yields

$$\mu_2(L/2-\Sigma)-\mu_1(L/2-\Sigma)=\frac{\Lambda_A}{R}[Y(L/2-\Sigma)-Y_C] \tag{A.18a}$$

$$\mu_3(L/2+\Sigma)-\mu_2(L/2+\Sigma)=\frac{\Lambda_B}{R}[Y(L/2+\Sigma)-Y_C] \tag{A.18b}$$

and

$$\mu'_1(S)=0, \quad \mu'_2(S)=\frac{\partial V}{\partial Y}, \quad \mu'_3(S)=0 \tag{A.19}$$

Eqs. (A.18) are then seen as jumps in the y-component of the internal force due to the external force coming from the disk, and Eqs. (A.19) are the equilibrium equations for the y-component of the resultant force in the beam. Requiring (A.10) to vanish for all $\overline{X}_C$ yields

$$-\frac{\Lambda_A}{R}[X(L/2-\Sigma)-X_C]-\frac{\Lambda_B}{R}[X(L/2+\Sigma)-X_C] \\ +\int_{L/2-\Sigma}^{L/2+\Sigma}\frac{\partial V}{\partial X_C}dS=0 \tag{A.20}$$

We use the identity $\frac{\partial V}{\partial X_C}=-\frac{\partial V}{\partial X}$ and (A.17) to obtain

$$\nu_2(L/2+\Sigma)-\nu_2(L/2-\Sigma)=-\frac{\Lambda_A}{R}[X(L/2-\Sigma)-X_C] \\ -\frac{\Lambda_B}{R}[X(L/2+\Sigma)-X_C] \tag{A.21}$$

The same procedure for the variable Y_C yields

$$\mu_2(L/2+\Sigma)-\mu_2(L/2-\Sigma)=-\frac{\Lambda_A}{R}[Y(L/2-\Sigma)-Y_C] \\ -\frac{\Lambda_B}{R}[Y(L/2+\Sigma)-Y_C] \tag{A.22}$$

Considering (A.21), (A.22), (A.15), and (A.18) together yields

$$\nu_1(L/2-\Sigma)=\nu_3(L/2+\Sigma) \tag{A.23}$$

$$\mu_1(L/2-\Sigma)=\mu_3(L/2+\Sigma) \tag{A.24}$$

which means that the internal force in the beam at the entrance of the disk is equal to the internal force at the exit of the disk. We therefore have that the total external force applied on the beam by the disk is zero. Finally requiring that (A.10) vanishes for all $\overline{\Sigma}$ yields

$$-2F_\gamma+V_A+V_B-\frac{\Lambda_A}{R}\{[X(L/2-\Sigma)-X_C]X'(L/2-\Sigma) \\ +[Y(L/2-\Sigma)-Y_C]Y'(L/2-\Sigma)\} \\ +\frac{\Lambda_B}{R}\{[X(L/2+\Sigma)-X_C]X'(L/2+\Sigma) \\ +[Y(L/2+\Sigma)-Y_C]Y'(L/2+\Sigma)\}=0 \tag{A.25}$$

In summary the equilibrium of the beam is governed by the system

$$X'(S)=\cos\theta \tag{A.26a}$$

$$Y'(S)=\sin\theta \tag{A.26b}$$

$$EI\theta'(S)=M \tag{A.26c}$$

$$M'(S)=N_x\sin\theta-N_y\cos\theta \tag{A.26d}$$

$$N'_x(S)=\chi\frac{\partial V}{\partial X}+\delta(S-S_A)\Lambda_A\frac{X_A-X_C}{R}+\delta(S-S_B)\Lambda_B\frac{X_B-X_C}{R} \tag{A.26e}$$

$$N'_y(S)=\chi\frac{\partial V}{\partial Y}+\delta(S-S_A)\Lambda_A\frac{Y_A-Y_C}{R}+\delta(S-S_B)\Lambda_B\frac{Y_B-Y_C}{R} \tag{A.26f}$$

with $\chi=1$ for $S\in[S_A;S_B]$ and $\chi=0$ otherwise, and where $\delta(S-S_\star)$ is the Dirac distribution centered on $S=S_\star$ and $X_{A,B}=X(\frac{L}{2}\pm\Sigma)$ and $Y_{A,B}=Y(\frac{L}{2}\pm\Sigma)$.

Appendix B. Incipient post-buckling regime

We here focus on configurations on path Ax. With regard to the shifted arc-length variable $\hat{s}=s-\ell/2$, introduced in Section 3, the variables have the following symmetries:

$$x(-\hat{s})=2x_C-x(\hat{s}), \quad y(-\hat{s})=y(\hat{s}), \quad \theta(-\hat{s})=-\theta(\hat{s}) \tag{B.1a}$$

$$m(-\hat{s})=m(\hat{s}), \quad n_x(-\hat{s})=n_x(\hat{s}), \quad n_y(-\hat{s})=-n_y(\hat{s}) \tag{B.1b}$$

The variable $n_y(\hat{s})$, an odd function of $\hat{s}$, has also to verify (A.24), which reads $n_y(\hat{s}=-\sigma)=n_y(\hat{s}=\sigma)$. Consequently $n_y(\pm\sigma)=0$ and, as $n_y(\hat{s})$ is constant for $|\hat{s}|>\sigma$, we have that $n_y(\hat{s})\equiv0$, $\forall|\hat{s}|>\sigma$. Moreover, in the limit where the barrier potential tends to zero, $v_0\to0$,[1]$n'_y(\hat{s})\equiv0$ inside the disk. Being an odd function, $n_y(\hat{s})$ is then such that

$$n_y(\hat{s})\equiv0 \quad \forall\hat{s} \tag{B.2}$$

The consequence is that the force jumps (A.18) for $n_y(\hat{s})$ at the entry $\hat{s}=-\sigma$ and exit $\hat{s}=+\sigma$ of the disk are zero: $\lambda_A[y_A-y_C]=0=\lambda_B[y_B-y_C]$. We discard the cases $\lambda_A=0$ and $\lambda_B=0$ for which there would not be any meniscus force at all, and conclude

$$y_A=y_C=y_B \tag{B.3}$$

Conditions (A.4b) and (A.4c) now read $(x_A-x_C)^2=1/4$ and $(x_B-x_C)^2=1/4$ which yields

$$x_A=x_C-1/2 \quad\text{and}\quad x_B=x_C+1/2 \tag{B.4}$$

As $n_x(-\hat{s})=n_x(\hat{s})$, the force jumps (A.15) imply that $\lambda_A[x_A-x_C]+\lambda_B[x_B-x_C]=0$. Using (B.4), we conclude that

$$\lambda_A=\lambda_B \tag{B.5}$$

Finally, using the global force balance (A.25), (B.3), (B.4), and (B.5), and still in the limit $v_0\to0$, we obtain

$$f_\gamma=\lambda_B\cos\theta_B \tag{B.6}$$

Taking advantage of the symmetries (B.1), we now rewrite the boundary-value problem (4)–(6) for the interval $\hat{s}\in[0,\ell/2]$. Using the external tension t, we write the x-component of the force as $n_x(\hat{s})\equiv t$, $\forall\hat{s}\in[\sigma,\ell/2]$ and using the jumps at $\hat{s}=\sigma$ we obtain $n_x(\hat{s})\equiv t-\lambda<0$, $\forall\hat{s}\in(0,\sigma)$ where we note $\lambda=\lambda_A=\lambda_B$. We therefore have to solve

$$dx^{in}/d\hat{s}=\cos\theta^{in}, \quad d\theta^{in}/d\hat{s}=m^{in}, \\ dm^{in}/d\hat{s}=-(\lambda-t)\sin\theta^{in} \quad\text{for } \hat{s}\in[0,\sigma] \tag{B.7a}$$

$$dx^{out}/d\hat{s}=\cos\theta^{out}, \quad d\theta^{out}/d\hat{s}=m^{out},$$

---

[1] The repulsion from the disk is only important for configurations in the deep post-buckling regime.

$$dm^{out}/d\hat{s} = -(\lambda - t)\sin\theta^{out} \quad \text{for } \hat{s} \in [\sigma, \ell/2] \tag{B.7b}$$

These are six differential equations with two unknowns parameters λ and σ. Boundary conditions are

$$x^{in}(0) = x_C, \quad \theta^{in}(0) = 0, \quad x^{in}(\sigma) = x_C + 1/2,$$
$$f_\gamma = \lambda\cos\theta^{in}(\sigma), \quad \theta^{out}(\ell/2) = 0 \tag{B.8}$$

and matching conditions are

$$x^{out}(\sigma) = x^{in}(\sigma), \quad \theta^{out}(\sigma) = \theta^{in}(\sigma), \quad m^{out}(\sigma) = m^{in}(\sigma) \tag{B.9}$$

Hence, for each given value of t, f_γ, ℓ, the eight boundary and matching conditions define a well-posed problem for Eqs. (B.7). For simplicity reasons, we replace the last condition in (B.8) by $\theta^{out}(+\infty) = 0$, that is we work in the large ℓ limit. We look for a small amplitude solution to this boundary-value problem, that is we develop each variable in power of ϵ, where ϵ is a small parameter. As buckling happens through a pitchfork bifurcation, two symmetric ($\epsilon > 0$, where the beam is buckled upward, and $\epsilon < 0$, where the beam is buckled downward) branches emerge from the $\epsilon = 0$ buckling point. Taking advantage of this symmetry we introduce the following series:

$$x^{in,out}(\hat{s}) = x_C + \hat{s} + \epsilon^2 x_2^{in,out}(\hat{s}) + O(\epsilon^4) \tag{B.10}$$

$$\theta^{in,out}(\hat{s}) = \epsilon\theta_1^{in,out}(\hat{s}) + \epsilon^3\theta_3^{in,out}(\hat{s}) + O(\epsilon^5) \tag{B.11}$$

$$m^{in,out}(\hat{s}) = \epsilon m_1^{in,out}(\hat{s}) + \epsilon^3 m_3^{in,out}(\hat{s}) + O(\epsilon^5) \tag{B.12}$$

$$t = t_0 + \epsilon^2 t_2 + O(\epsilon^4) \tag{B.13}$$

$$\lambda = f_\gamma + \epsilon^2\lambda_2 + O(\epsilon^4) \tag{B.14}$$

$$\sigma = 1/2 + \epsilon^2\sigma_2 + O(\epsilon^4) \tag{B.15}$$

Solving the problem (B.7)–(B.9), we find at order ϵ^1 that

$$\theta_1^{in}(\hat{s}) = \sin(\hat{s}\sqrt{f - t_0}) \tag{B.16}$$

$$\theta_1^{out}(\hat{s}) = e^{\sqrt{t_0}/2}\sin\left(\frac{\sqrt{f - t_0}}{2}\right)e^{-\hat{s}\sqrt{t_0}} \tag{B.17}$$

and that t_0 is solution to the equation

$$\sqrt{f - t_0}\cos\left(\frac{\sqrt{f - t_0}}{2}\right) + \sqrt{t_0}\sin\left(\frac{\sqrt{f - t_0}}{2}\right) = 0 \tag{B.18}$$

which is (12). At order ϵ^2, we find

$$\lambda_2 = \frac{1}{2}f_\gamma\sin^2\left(\frac{\sqrt{f - t_0}}{2}\right) \tag{B.19}$$

$$\sigma_2 = \frac{\sqrt{f - t_0} - \sin\left(\sqrt{f - t_0}\right)}{8\sqrt{f - t_0}} \tag{B.20}$$

$$x_2^{in}(\hat{s}) = \frac{\sin(2\hat{s}\sqrt{f - t_0}) - 2\hat{s}\sqrt{f - t_0}}{8\sqrt{f - t_0}} \tag{B.21}$$

$$x_2^{out}(\hat{s}) = \frac{\sin\left(\sqrt{f - t_0}\right)}{8\sqrt{f - t_0}} - \frac{1}{8} + \frac{\sin^2\left(\frac{\sqrt{f - t_0}}{2}\right)(e^{(1 - 2\hat{s})\sqrt{t_0}} - 1)}{4\sqrt{t_0}} \tag{B.22}$$

At order ϵ^3, we find $\theta_3^{in}(\hat{s})$, $m_3^{in}(\hat{s})$, $\theta^{out}(\hat{s})$, and $m^{out}(\hat{s})$ and from their matching conditions (B.9), we obtain

$$t_2 = \frac{f_\gamma^2(4 + 5\sqrt{t_0}) - f_\gamma t_0(2 + 3\sqrt{t_0}) + 2t_0^2 - 2f_\gamma[f_\gamma(\sqrt{t_0} - 2) + 4t_0]\cos(\sqrt{f - t_0})}{8f_\gamma(2 + \sqrt{t_0})} \tag{B.23}$$
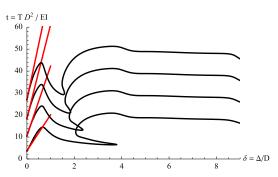

Fig. B1. Paths Ax for $f_\gamma = 20, 30, 40$ and 50 with their slope at the origin given by (B.25).

We now compute the end-shortening $\delta = \ell - x(s = \ell) = \ell - 2[x^{out}(\hat{s} = \ell/2) - x_C]$, still in the limit where $\ell \to +\infty$. Using (B.10) and (B.22) we find $\delta = \epsilon^2\delta_2$ with

$$\delta_2 = \frac{1}{4} + \frac{\sin^2\left(\frac{\sqrt{f - t_0}}{2}\right)}{2\sqrt{t_0}} - \frac{\sin\sqrt{f - t_0}}{4\sqrt{f - t_0}} \tag{B.24}$$

Finally we write

$$t = t_0 + \epsilon^2 t_2 = t_0 + \frac{t_2}{\delta_2}\delta \tag{B.25}$$

We plot in Fig. B1 paths Ax for $f_\gamma = 20, 30, 40$ and 50 and the straight lines given by (B.25).

References

[1] R. Foelix, Biology of Spiders, Oxford University Press, Oxford, 2010.
[2] F.G. Omenetto, D.L. Kaplan, New opportunities for an ancient material, Science 329 (5991) (2010) 528–531.
[3] F. Vollrath, D.P. Knight, Liquid crystalline spinning of spider silk, Nature 410 (6828) (2001) 541–548.
[4] N. Becker, E. Oroudjev, S. Mutz, J.P. Cleveland, P.K. Hansma, C.Y. Hayashi, D.E. Makarov, H.G. Hansma, Molecular nanosprings in spider capture-silk threads, Nat. Mater. 2 (4) (2003) 278–283.
[5] F. Vollrath, D.T. Edmonds, Modulation of the mechanical properties of spider silk by coating with water, Nature 340 (6231) (1989) 305–307.
[6] H. Elettro, S. Neukirch, F. Vollrath, A. Antkowiak, In-drop Capillary Spooling of Spider Capture Thread Inspires Highly Extensible Fibres, arXiv:1501.00962, 2015.
[7] N. Stoop, J. Najafi, F.K. Wittel, M. Habibi, H.J. Herrmann, Packing of elastic wires in spherical cavities, Phys. Rev. Lett. 106 (2011) 214102.
[8] R. Vetter, F.K. Wittel, H.J. Herrmann, Morphogenesis of filaments growing in flexible confinements, Nat. Commun. 5 (2014).
[9] L. Boué, M. Adda-Bedia, A. Boudaoud, D. Cassani, Y. Couder, A. Eddi, M. Trejo, Spiral patterns in the packing of flexible structures, Phys. Rev. Lett. 97 (16) (2006) 166104.
[10] E. Couturier, S. Courrech du Pont, S. Douady, The filling law: a general framework for leaf folding and its consequences on leaf shape diversity, J. Theoret. Biol. 289 (2011) 47–64.
[11] J.C. LaMarque, T.-v.L. Le, S.C. Harvey, Packaging double-helical DNA into viral capsids, Biopolymers 73 (3) (2004) 348–355.
[12] W.S. Klug, M.T. Feldmann, M. Ortiz, Three-dimensional director-field predictions of viral DNA packing arrangements, Comput. Mech. 35 (2) (2005) 146–152.
[13] A. Leforestier, F. Livolant, Structure of toroidal DNA collapsed inside the phage capsid, Proc. Natl. Acad. Sci. 106 (23) (2009) 9157–9162.
[14] R.S. Manning, G.B. Bulman, Stability of an elastic rod buckling into a soft wall, Proc. R. Soc. A: Math. Phys. Eng. Sci.: Math. 461 (2060) (2005) 2423–2450.
[15] E. Doedel, H.B. Keller, J.P. Kernevez, Numerical analysis and control of bifurcation problems: bifurcation in infinite dimensions, Int. J. Bifurc. Chaos 01 (04) (1991) 745–772.
[16] G.H.M. van der Heijden, S. Neukirch, V.G.A. Goss, J.M.T. Thompson, Instability and self-contact in the writhing of clamped rods, Int. J. Mech. Sci. 45 (1) (2003) 161–196.
[17] V.G.A. Goss, G.H.M. van der Heijden, J.M.T. Thompson, S. Neukirch, Experiments on snap buckling, hysteresis and loop formation in twisted rods, Exp. Mech. 45 (2) (2005) 101–111.
[18] H. Elettro, S. Neukirch, A. Antkowiak, Equilibrium and stability of a twisted rod confined in a liquid drop, 2015, in preparation.

SHORT COMMUNICATION

Adhesion of dry and wet electrostatic capture silk of uloborid spider

Hervé Elettro[1] · Sébastien Neukirch[1] · Arnaud Antkowiak[1] · Fritz Vollrath[2]

Abstract We demonstrate the impressive adhesive qualities of uloborid spider orb-web capture when dry, which are lost when the nano-filament threads are wetted. A force sensor with a 50 nN–1 mN detection sensitively allowed us to measure quantitatively the stress–strain characteristics of native silk threads in both the original dry state and after wetting by controlled application of water mist with droplet sizes ranging between 3 and 5 µm and densities ranging between 10^4 and 10^5 per mm^3. Stress forces of between 1 and 5 µN/µm^2 in the native, dry multifilament thread puffs were reduced to between 0.1 and 0.5 µN/µm^2 in the wetted collapsed state, with strain displacements reducing from between 2 and 5 mm in the dry to 0.10–0.12 mm in the wetted states. We conclude that wetting cribellate threads reduce their van der Waals adhesion with implications on the thread's adhesive strength under tension. This should be considered when discussing the evolutionary transitions of capture silks from the ancestral dry-state nano-filaments of the cribellate spider taxa to the wet-state glue-droplets of the ecribellate taxa.

Communicated by: Sven Thatje

✉ Fritz Vollrath
fritz.vollrath@zoo.ox.ac.uk

1 Sorbonne Universités, UPMC Paris 06, CNRS, UMR 7190, F-75005 Paris, France

2 Department of Zoology, University of Oxford, South Parks Rd, Oxford OX1 3PS, UK

Introduction

Orb-web spiders use two very different mechanisms to entrap insects in their capture threads. The evolutionary more ancestral cribellate technique requires the spider to slowly and laboriously hackle thousands of fine filaments, while the more advanced (i.e. derived) ecribellate technology deploys highly cost-efficient self-assembling glue droplets (Vollrath 2005). Molecular profiling suggests that the two mechanisms have dissimilar evolutionary histories with strong evidence for independent origins of the two types of orb webs (Fernández et al. 2014; Bond et al. 2014) despite many similarities in architecture and ecology (Shear 1986; Bond and Opell 1998; Foelix 2011; Opell and Bond 2001). The two opposing mechanisms of prey capture rely on fundamental differences between the two types of silk used by the two weaver types, cribellate and ecribellate, in their orb-web capture threads.

Indeed, these two different prey-capture systems are functionally opposed and comprise very different technologies (Peters 1987, 1995; Vollrath 2005; Opell and Schwend 2009; Opell et al. 2011; Sahni et al. 2011), i.e. the hackled-and-puffed nano-thread-adhesion capture system of the cribellate spiders (Peters 1984; Opell 1994) and the two-component-extrusion glue-adhesion system of the ecribellate spiders (Vollrath and Edmonds 1989; Opell and Hendricks 2007). The hackled threads relies on the spider to comb and electrostatically charge the threads, which are understood to attach and adhere to the insect by van-der-Waals forces (Hawthorn and Opell 2002, 2003). The aqueous glue threads carry droplets that self-assemble via a Rayleigh-Plateau transition upon water adsorption from the atmosphere (Edmonds and Vollrath

1992) and attach by surface wetting and glycoprotein adhesion (Vollrath et al. 1990; Vollrath and Tillinghast 1991; Opell and Hendricks 2007). Consequently, it has been deduced that the glue threads only work when wet while hackled threads work best when dry (Peters 1987; Opell 1994) or dryish (Hawthorn and Opell 2003).

It seems from the literature (cited so far as well as see also, e.g. Blackledge and Hayashi 2006) that the cribellate system would fundamentally depend on its original, non-wetted, highly puffed-out configuration state for the nano-fibrils to retain their function. Indeed, the very spinning mechanism of the cribellum fibre composite is specially adapted to an electrostatic spinning process that leads to the configuration of hackled puffs of dry silk nano-filaments astride core carrier threads (Kronenberger and Vollrath 2015). One must argue that the puffs, in turn, would rely on dryness for their continued function, if indeed, electrostatic forces and nano-adhesion sites are keys to their functionality. Confusingly, it has also been shown that high ambient humidity seems to increase the adhesive properties of some (nano-noded) cribellum threads, perhaps by adding capillary forces to electrostatic forces (Hawthorn and Opell 2003), strange as that might sound considering potentially conflicting physical dynamics.

Here, we test the hypothesis that cribellate capture threads are indeed much more sticky when dry as opposed to when wetted. *Uloborus* cribellum threads were exposed to high-density mist and their adhesion to a nano-force tensile tester measured before and after wetting. Imagery of both dry/puffed and wetted/collapsed threads complemented the force measurements.

Materials and methods

Uloborus plumipes spiders were collected at the Paris Jardin des Plantes greenhouse and taken into the laboratory where they spun webs in appropriate frames. The experimental apparatus consisted of a combination of microscope and stress–strain gage with the added ability of controlled application of water mist. *Uloborus* capture thread samples were carefully taken from a web using calipers to avoid deformation, straining and stressing. The samples were then tested at T 20 °C using a FemtoTools, FT-FS1000 detection capacitive force sensor with a 50 nN–1 mN measurement range in two different ways. Press-in is meant to approximate forward contact loading resulting from an insect hitting the web straight on. Press-on is meant to approximate a more a side-ways hit with shear loading generated by lateral body contact and flapping wings. Contact areas were calculated from the cross-section area of the sensor in contact with the sample. For the press-in setup, this is the full cross-section area of the sensor tip along its main axis, which is square with border size 50 μm, i.e. 2500 $μm^2$. For the press-on setup, the full width

of the sample (that is 100 μm for the dry case) is in contact with the edge of the sensor (that is 50 μm), i.e. 5000 $μm^2$. These contact areas are used for normalizing forces to allow comparison between press-in and press-on forces. Even though the contact area in not the same for the dry and wet threads, we use the same normalisation area for the wet case to account for the physical differences between the samples.

Wetting was achieved by controlled mega-sonic misting of distilled water at controlled droplet sizes ranging between 3 and 5 μm and at densities ranging between 10^4 and 10^5 per mm^3. We note (i) that threads dried out very quickly (see also video in Suppl. Material and/or www-link) and (ii) that it made no difference to dimensions and adhesive properties whether prior to the measurements pre-wetted threads were left at room humidity (50 % rH) or thoroughly desiccated by exposure to dry air surrounding a small dish of exposed phosphorus-pentoxide P_2O_5, which is an excellent way of drying silk threads (Vollrath and Edmonds 1989). SEM images were taken at a range of magnifications with 10 nm of Gold/Palladium coating.

Results and discussion

Our experiment demonstrated that wetting destroys the adhesive properties of the threads. We conclude that rain or even heavy mist would render the *Uloborus* capture threads unable to retain any prey that they may intercept (Fig. 1).

In its native state, the cribellate silk studied showed the typical uloborid puffs. These collapsed during even brief 5 min wetting (see Suppl Materials and www-link for video).
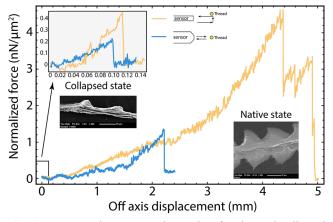
Fig. 1 Representative stress–stain graphs of native and collapsed cribellate capture silk adhering to a sensor. Measurements were taken subsequently on the same piece of capture thread of *Uloborus plumipes*, and images were taken from adjacent sections of the same thread. The sensor was either pushed into the thread or lowered onto the thread before being pulled away; in both cases, the force of contact was equivalent. Please note that these two curves are representative for 14 individual stress–strain tests, further explanations and significances in the text. Inserts: SEM images of a capture thread in the native puffed state and collapsed after wetting

The measured adhesion forces differed significantly between native-puffed and wetted-collapsed threads (Fig. 1), and this was irrespective whether the sensor was pushed (pressed) forward into the capture thread or pushed (pressed) down unto it (one tailed t tests, $p=1.0$ and 0.75 % respectively, $N=4$, $n=14$). For the dry threads, pushing onto a thread followed by pulling away showed stronger adhesion than pushing into a thread, again this was highly significant (Fig. 1, one tailed t test $p=1.4$ %). We assign this difference in force to the concurrent difference in contact between the sensor and the individual filaments. In the case of push-in/pull-out, the contact area of the sensor would have been about 2500 μm^2 and adherent threads were pulled away at more or less 90 degree. In the case of push-down/pull-away, the contact area of the sensor would have been about 5000 μm^2 and the threads are pulled in the area of contact and in a very oblique angle, which would allowed for much longer periods of contact over the same pulling distance. Of course, the differences of actual filament contact area between sensor and threads would change when the filaments are all collapsed into one-another, as happens when they are wetted (Fig. 1 left inset), which is in stark contrast to their native state when they are fully puffed out (Fig. 1 right inset).

The experimental wetting may or may not have affected electrostatic charges of the thread by temporary grounding of the otherwise insolating threads via the applied aqueous mist coating. However, it is much more likely that the wetting-induced collapse of the filament puffs significantly decreased the number of surface contact area/points and that this alone would account for the significant drop in adhesion after wetting. As our images show, and as Peters 1987 predicted which Zheng et al. 2010 confirmed, wetting the submicron capture filaments of *Uloborus* causes them to coalesce, which is an important phenomenon in fibre physics and hence reasonably well understood (Bico et al. 2004). As we have shown here, fine mist accumulates quickly and effectively destroys the adhesive effectiveness of hackled silk. For the spider, this means that fog (or perhaps even dew) may radically decrease the capture efficiency of an *Uloborus* web. As is well known, all orb weavers, cribellate and ecribellate alike, tend to take down their webs in rain. In the ecribellates, this is a response to droplet overloading, which leads to sagging threads that can snap and compromise the integrity of the whole structure. Overloading might also be a problem for cribellate capture silks but even a fine mist, as we have now demonstrated, leads to an irreversible loss of function which in turn would require web rebuilding.

We believe that our observations contribute to recent developments concerning our understanding of the evolution of spider capture threads. Two recent publications provide evidence for 'independent origins for the two types of orb webs' (p 1772, Fernández et al. 2014) and 'reject the prevailing paradigm of a monophyletic Orbiculariae' clade (p 1765,

Bond et al. 2014). Both studies used state-of-the-art gene sequencing coupled to other analyses of lineage relationships. Our discovery that wetting renders in-operable the evolutionary older cribellum capture threads suggests that a simple transition to the obligatory wet droplet threads of the ecribellate orb-weavers would have been far from straightforward, if at all possible, and thus strongly supports the notion of independent evolution of orb spider capture threads and, by extension, perhaps also of web spiral geometries and web-building behaviour patterns. Last but not least, our observations challenge the deductions of Zheng et al. (2010) who see wetting as such an integral part of cribellate capture thread function that it bio-inspired them to design supposedly derivative synthetic water collectors (Zheng 2014).

References

Bico J, Roman B, Moulin L, Boudaoud A (2004) Elastocapillary coalescence in wet hair. Nature 432:690

Blackledge TA, Hayashi CY (2006) Unraveling the mechanical properties of composite silk threads spun by cribellate orb-weaving spiders. J Exp Bio 209:3131–3140

Bond JA, Opell DB (1998) Testing adaptive radiation and key innovation hypotheses in spiders. Evolution 52:403–414

Bond JE, Garrison NL, Hamilton CA, Godwin RL, Hedin M, Agnarsson I (2014) Phylogenomics resolves a spider backbone phylogeny and rejects a prevailing paradigm for orb web evolution. Curr Biol 24:1765–1771

Edmonds D, Vollrath F (1992) The contribution of atmospheric water vapour to the formation and efficiency of a spider's capture web. Proc Roy Soc London 248:145–148

Fernández R, Hormiga G, Giribet G (2014) Phylogenomic analysis of spiders reveals nonmonophyly of orb weavers. Curr Biol 24:1772–1777

Foelix R (2011) Biology of spiders, 3rd edn. Oxford Univ. Press, Oxford

Hawthorn AC, Opell BD (2002) Evolution of adhesive mechanisms, in cribellar spider prey capture thread: Evidence for van der Waals and hygroscopic forces. Biol J Linn Soc Lond 77:1–8

Hawthorn AC, Opell BD (2003) Van der Waals and hygroscopic forces of adhesion generated by spider capture threads. J Exp Biol 206:3905–3911

Kronenberger K, Vollrath F (2015) Spiders spinning electrically charged nano-fibres. Biol Let 11(1):20140813. doi:10.1098/rsbl.2014.0813

Opell BD (1994) Factors governing the stickiness of cribellar prey capture threads in the spider family Uloboridae. J Morphol 221:111–119

Opell DB, Bond JE (2001) Changes in the mechanical properties of capture threads and the evolution of modern orb-weaving spiders. Evol Ecol Res 3:567–581

Opell DB, Hendricks ML (2007) Adhesive recruitment by the viscous capture threads of, araneoid orb-weaving spiders. J Exp Biol 210:553–560

Opell BD, Schwend HS (2009) Adhesive efficiency of spider prey capture threads. Zoology 112:16–26

Opell BD, Tran AM, Karinshak SE (2011) Adhesive compatibility of cribellar and viscous prey capture threads and its implication for the evolution of orb-weaving, spiders. J Exp Zool 315:376–384

Peters TM (1984) The spinning apparatus of Uloboridae in relation, to the structure and construction of capture threads, (Arachnida, Araneida). Zoomorph 104:96–104

Peters HM (1987) Fine Structure and Function of Capture Threads in Ecophysiology of Spiders. pp187-202 in (ed.) W. Nentwig Springer-Verlag Berlin Heidelberg

Peters HM (1995) Ultrastructure of orb spiders' gluey capture threads. Naturwissenschaften 82:380–382

Sahni V, Blackledge TA, Dhinojwala A (2011) A review on spider silk adhesion. J Adhes 87:595–614

Shear W (1986) Spiders, Webs, Behavior and Evolution. Stanford University Press

Vollrath F (2005) Spiders' Webs. Curr Biol 15:R364–R365

Vollrath F, Fairbrother WJ, Williams RJP, Tillinghast EK, Bernstein DT, Gallager KS, Townley MA (1990) Compounds in the droplets of the orb spider's viscid spiral. Nature 345:526–528

Vollrath F, Edmonds D (1989) Modulation of the mechanical properties of spider silk by coating with water. Nature 340:305–307

Vollrath F, Tillinghast E (1991) Glycoprotein glue beneath a spider web's aqueous coat. Naturwissenschaften 78:557–559

Zheng Y, Bai H, Huang Z, Tian X, Nie FQ, Zhao Y, Zhai J, Jiang L (2010) Directional water collection on wetted spider silk. Nature 462:640–443

Zheng Y 2014 <http://www.rsc.org/chemistryworld/2014/08/interview-yongmei-zheng-spider-silk-water-droplet>

Adam, N. K. Detergent action and its relation to wetting and emulsification. *Journal of the Society of Dyers and Colourists*, 53(4):121–129, 1937.

Agnarsson, I., Kuntner, M., and Blackledge, T. A. Bioprospecting finds the toughest biological material: Extraordinary silk from a giant riverine orb spider. *PLoS ONE*, 5(9), 2010.

Amarouchene, Y., Bonn, D., Meunier, J., and Kellay, H. Inhibition of the finite-time singularity during droplet fission of a polymeric fluid. *Physical Review Letters*, 86(16):3558, 2001.

Antkowiak, A., Audoly, B., Josserand, C., Neukirch, S., and Rivetti, M. Instant fabrication and selection of folded structures using drop impact. *Proceedings of the National Academy of Sciences of the United States of America*, 108(26):10400–10404, 2011.

Aoyanagi, Y. and Okumura, K. Simple model for the mechanics of spider webs. *Physical Review Letters*, 104(3):038102, 2010.

Audoly, B. and Pomeau, Y. *Elasticity and geometry: from hair curls to the nonlinear response of shells.* Oxford University Press, 2010.

Becker, N., Oroudjev, E., Mutz, S., Cleveland, J. P., Hansma, P. K., Hayashi, C. Y., Makarov, D. E., and Hansma, H. G. Molecular nanosprings in spider capture-silk threads. *Nat. Mater*, 2(4):278–283, 2003.

Bico, J., Roman, B., Moulin, L., and Boudaoud, A. Adhesion: Elastocapillary coalescence in wet hair. *Nature*, 432(7018):690–690, 2004.

Bikerman, J. Surface energy of solids. *physica status solidi (b)*, 10(1):3–26, 1965.

Blackledge, T. A., Swindeman, J. E., and Hayashi, C. Y. Quasistatic and continuous dynamic characterization of the mechanical properties of silk from the cobweb of the black widow spider Latrodectus hesperus. *Journal of Experimental Biology*, 208(10):1937–1949, 2005.

Blackledge, T. A., Scharff, N., Coddington, J. A., Szüts, T., Wenzel, J. W., Hayashi, C. Y., and Agnarsson, I. Reconstructing web evolution and spider diversification in the molecular era. *Proceedings of the National Academy of Sciences of the United States of America*, 106(13):5229–5234, 2009.

Blackledge, T. A., Sahni, V., and Dhinojwala, A. Viscoelastic solids explain spider web stickiness. *Nat Commun*, 1:19, May 2010.

Brunetta, L. and Craig, C. L. *Spider silk: Evolution and 400 million years of spinning, waiting, snagging, and mating*. Yale University Press, 2010.

Carroll, B. J. The accurate measurement of contact angle, phase contact areas, drop volume, and Laplace excess pressure in drop-on-fiber systems. *Journal of Colloid and Interface Science*, 57(3):488–495, 1976.

Carroll, B. J. Equilibrium conformations of liquid drops on thin cylinders under forces of capillarity. A theory for the roll-up process. *Langmuir*, 2(2):248–250, 1986.

Chakrapani, N., Wei, B., Carrillo, A., Ajayan, P. M., and Kane, R. S. Capillarity-driven assembly of two-dimensional cellular carbon nanotube foams. *Proc. Natl Acad. Sci. USA*, 101:4009–4012, 2004.

Collier, A. M. *A handbook of textiles*. Pergamon Press, 1970.

Cranford, S. W., Tarakanova, A., Pugno, N. M., and Buehler, M. J. Nonlinear material behaviour of spider silk yields robust webs. *Nature*, 482(7383):72–76, 2012.

De Gennes, P.-G. and Prost, J. The physics of liquid crystals. *Oxford University Press*, 2713:48, 1993.

De Gennes, P.-G., Brochard-Wyart, F., and Quéré, D. *Capillarity and wetting phenomena: drops, bubbles, pearls, waves*. Springer Science & Business Media, 2004.

De Langre, E. Effects of wind on plants. *Annual Review of Fluid Mechanics*, 40(1):141–168, 2008.

De Volder, M. and Hart, A. J. Engineering hierarchical nanostructures by elastocapillary self-assembly. *Angewandte Chemie International Edition*, 52(9):2412–2425, 2013.

Deboeuf, S., Adda-Bedia, M., and Boudaoud, A. Energy distributions and effective temperatures in the packing of elastic sheets. *EPL (Europhysics Letters)*, 85(2):24002, 2009.

Denny, M. The physical properties of spider's silk and their role in the design of orb-webs. *The Journal of Experimental Biology*, 65(2):483–506, 1976.

Dicko, C., Porter, D., Bond, J., Kenney, J. M., and Vollrath, F. Structural disorder in silk proteins reveals the emergence of elastomericity. *Biomacromolecules*, 9(1):216–221, 2008.

Dirac, P. A. M. *The principles of quantum mechanics*, volume 4. Clarendon Press Oxford, 1958.

Dumais, J. and Forterre, Y. "Vegetable Dynamicks": The Role of Water in Plant Movements. *Annual Review of Fluid Mechanics*, 44(1):453–478, 2012.

Edmonds, D. T. and Vollrath, F. The contribution of atmospheric water vapour to the formation and efficiency of a spider's capture web. *Proc. B.*, 248(1322):pp. 145–148, 1992.

Eisner, T. and Aneshansley, D. J. Defense by foot adhesion in a beetle (Hemisphaerota cyanea). *Proceedings of the National Academy of Sciences of the United States of America*, 97(12):6568–6573, 2000.

Elettro, H., Neukirch, S., Antkowiak, A., and Vollrath, F. Adhesion of dry and wet electrostatic capture silk of uloborid spider. *The Science of Nature*, 102(7-8):1–4, 2015.

Elettro, H., Vollrath, F., Antkowiak, A., and Neukirch, S. Coiling of an elastic beam inside a disk: A model for spider-capture silk. *International Journal of Non-Linear Mechanics*, 75:59–66, 2015.

Erbil, H. Y., McHale, G., and Newton, M. Drop evaporation on solid surfaces: constant contact angle mode. *Langmuir*, 18(7):2636–2641, 2002.

Euler, L. *Methodus inveniendi lineas curvas maximi minimive proprietate gaudens*. 1744.

Flügge-Lotz, I. and Flügge, W. Ludwig Prandtl in the nineteen-thirties: Reminiscences. *Annual Review of Fluid Mechanics*, 5:1–9, 1973.

Foelix, R. *Biology of spiders*. Oxford University Press, 2010.

Forterre, Y., Skotheim, J. M., Dumais, J., and Mahadevan, L. How the Venus flytrap snaps. *Nature*, 433 (7024):421–425, 2005.

Gao, L. and McCarthy, T. J. The "lotus effect" explained: two reasons why two length scales of topography are important. *Langmuir*, 22(7):2966–2967, 2006.

Gaume, L. and Forterre, Y. A viscoelastic deadly fluid in carnivorous pitcher plants. *PloS ONE*, 2(11): e1185, 2007.

Gauss, C. *Principia generalia theoriae figurae fluidorum in statu aequilibrii*. Nabu Press, Göttingae, Germany, 1830.

Gay, C. Stickiness—some fundamentals of adhesion. *Integrative and comparative biology*, 42(6):1123–1126, 2002.

Good, R. J. and Elbing, E. Generalization of theory for estimation of interfacial energies. *Industrial & Engineering Chemistry*, 62(3):54–78, 1970.

Gordon, J. *Structures: or why things don't fall down*. Da Capo Press, 2003.

Gosline, J. M., Denny, M. W., and DeMont, M. E. Spider slik as rubber. *Nature*, 309(7):551–552, 1984.

Gosline, J. M., DeMont, M., and Denny, M. W. The structure and properties of spider silk. *Endeavour*, 10(1):37 – 43, 1986.

Gracias, D., Kavthekar, V., Love, J., Paul, K., and Whitesides, G. Fabrication of micrometer-scale, patterned polyhedra by self-assembly. *Advanced Materials*, 14(3):235–238, 2002.

Greiner, A. and Wendorff, J. Electrospinning: A fascinating method for the preparation of ultrathin fibers. *Angew. Chem. Int. Ed. Engl.*, 46(30):5670–5703, 2007.

Heil, M. Minimal liquid bridges in non-axisymmetrically buckled elastic tubes. *Journal of Fluid Mechanics*, 380(-1):309–337, 1999.

Heimer, S. Wunderbare Welt der Spinnen. 1988.

Helmer, M. Biomaterials: Dew catchers. *Nature*, 463(7281):618–618, 2010.

Hillyard, P. *The book of the spider: from arachnophobia to the love of spiders*. Hutchinson, 1994.

Hochmuth, R. M., Mohandas, N., and Blackshear Jr, P. Measurement of the elastic modulus for red cell membrane using a fluid mechanical technique. *Biophysical Journal*, 13(8):747, 1973.

Hodgson, T. and Lee, J. The effect of surfactants on the coalescence of a drop at an interface I. *Journal of Colloid and Interface Science*, 30(1):94–108, 1969.

Holland, C., Vollrath, F., Ryan, A. J., and Mykhaylyk, O. O. Silk and synthetic polymers: Reconciling 100 degrees of separation. *Advanced Materials*, 24(1):105–109, 2012.

Humphrey, J. Fluid mechanics constraints on spider ballooning. *Oecologia*, 73(3):469–477, 1987.

Hure, J. and Audoly, B. Capillary buckling of a thin film adhering to a sphere. *Journal of the Mechanics and Physics of Solids*, 61(2):450–471, 2013.

Jackson, R. R. and Wilcox, R. S. Spider-eating spiders: Despite the small size of their brain, jumping spiders in the genus portia outwit other spiders with hunting techniques that include trial and error. *American Scientist*, pages 350–357, 1998.

Jacob, F. Evolution and tinkering. *Science*, 196(4295):1161–1166, 1977.

Jung, S., Clanet, C., and Bush, J. W. M. Capillary instability on an elastic helix. *Soft Matter*, 10: 3225–3228, 2014.

Kanellopoulos, A. and Owen, M. Adsorption of sodium dodecyl sulphate at the silicone fluid/water interface. *Transactions of the Faraday Society*, 67:3127–3138, 1971.

Katzav, E., Adda-Bedia, M., and Boudaoud, A. A statistical approach to close packing of elastic rods and to DNA packaging in viral capsids. *Proceedings of the National Academy of Sciences of the United States of America*, 103(50):18900–18904, 2006.

Kent, J. Quasi-steady diffusion-controlled droplet evaporation and condensation. *Applied Scientific Research*, 28(1):315–360, 1973.

Kim, D.-H., Viventi, J., Amsden, J. J., Xiao, J., Vigeland, L., Kim, Y.-S., Blanco, J. A., Panilaitis, B., Frechette, E. S., Contreras, D., Kaplan, D. L., Omenetto, F. G., Huang, Y., Hwang, K.-C., Zakin, M. R., Litt, B., and Rogers, J. A. Dissolvable films of silk fibroin for ultrathin conformal bio-integrated electronics. *Nat Mater*, 9(6):511–517, 2010.

Koch, G. W., Sillett, S. C., Jennings, G. M., and Davis, S. D. The limits to tree height. *Nature*, 428 (6985):851–854, 2004.

Kronenberger, K. and Vollrath, F. Spiders spinning electrically charged nano-fibres. *Biology letters*, 11 (1):20140813, 2015.

Kronenberger, K., Dicko, C., and Vollrath, F. A novel marine silk. *Naturwissenschaften*, 99(1):3–10, 2012.

Lafuma, A. and Quéré, D. Superhydrophobic states. *Nature Materials*, 2(7):457–460, 2003.

Landau, L. and Lifchitz, E. *Théorie de l'élasticité*. Éditions de Moscou, 1967.

Landau, L. D. and Levich, B. volume 17. 1942.

Laplace, P. Traité de mécanique céleste; suppléments au livre X, 1805 and 1806 resp. *Œuvres Complètes*, 4, 1805.

Lazarus, A., Florijn, H., and Reis, P. Geometry-induced rigidity in nonspherical pressurized elastic shells. *Physical Review Letters*, 109(14):144301, 2012.

Leforestier, A. and Livolant, F. Structure of toroidal dna collapsed inside the phage capsid. *Proceedings of the National Academy of Sciences*, 106(23):9157–9162, 2009.

Lewicka, M., Hermanson, O., and Rising, A. U. Recombinant spider silk matrices for neural stem cell cultures. *Biomaterials*, 33(31):7712 – 7717, 2012.

Li, L. K. B. *An experimental study on air-blast atomization of viscoelastic liquids*. PhD thesis, University of British Columbia, 2006.

Lidmar, J., Mirny, L., and Nelson, D. R. Virus shapes and buckling transitions in spherical shells. *Physical Review E*, 68(5):051910, 2003.

Lin, L. H., Edmonds, D. T., and Vollrath, F. Structural engineering of an orb-spider's web. *Nature*, 373 (6510):146–148, 1995.

Liu, Y., Sponner, A., Porter, D., and Vollrath, F. Proline and processing of spider silks. *Biomacromolecules*, 9(1):116–121, 2007.

Lorenceau, É., Clanet, C., and Quéré, D. Capturing drops with a thin fiber. *Journal of Colloid and Interface Science*, 279(1):192 – 197, 2004.

Lorenceau, E., Senden, T., and Quéré, D. Wetting of fibers. In Weiss, R. and Terech, P., editors, *Molecular Gels. Materials with Self-Assembled Fibrillar Networks*, pages 223–237. Springer, 2006.

Lucas, F. Spiders and their silks. *Discovery. Lond.*, 25:1–7, 1964.

Maleki, M., Reyssat, E., Quéré, D., and Golestanian, R. On the Landau-Levich transition. *Langmuir*, 23(20):10116–10122, 2007.

Manning, R. S. and Bulman, G. B. Stability of an elastic rod buckling into a soft wall. *Proceedings of the Royal Society A: Mathematical, Physical and Engineering Science*, 461(2060):2423–2450, 2005.

Marko, J. F. and Cocco, S. The micromechanics of DNA. *Phys. World*, 16:37–41, 2003.

Moisseiff, L. S. and Lienhard, F. Suspension bridges under the action of lateral forces. *Transactions of the American Society of Civil Engineers*, 2(98):1080–1141, 1933.

Noblin, X., Rojas, N. O., Westbrook, J., Llorens, C., Argentina, M., and Dumais, J. The Fern Sporangium: A Unique Catapult. *Science*, 335(6074):1322, 2012.

Nyffeler, M. and Benz, G. Spiders in natural pest control: A review. *Journal of Applied Entomology*, 103(1-5):321–339, 1987.

Omenetto, F. G. and Kaplan, D. L. New opportunities for an ancient material. *Science*, 329(5991): 528–531, 2010.

Opell, B. and Hendricks, M. The role of granules within viscous capture threads of orb-weaving spiders. *The Journal of experimental biology*, 213(2):339–346, 2010.

Opell, B. D. What forces are responsible for the stickiness of spider cribellar threads? *Journal of Experimental Zoology*, 265(5):469–476, 1993.

129

Opell, B. D. Factors governing the stickiness of cribellar prey capture threads in the spider family Uloboridae. *Journal of Morphology*, 221(1):111–119, 1994.

Opell, B. D. Redesigning spider webs: Stickiness, capture area and the evolution of modern orb-webs. *Evolutionary ecology research*, 1:503–516, 1999.

Opell, B. D., Karinshak, S. E., and Sigler, M. A. Humidity affects the extensibility of an orb-weaving spider's viscous thread droplets. *The Journal of Experimental Biology*, 214(17):2988–2993, 2011.

Ortega, V. and Dudley, R. Spiderweb deformation induced by electrostatically charged insects. *Sci. Rep.*, 3, 2013.

Ostwald, W. *Lehrbuch der Allgemeinen Chemie*, volume 2. Leipzig, Germany, 1896.

Petrov, A. S. and Harvey, S. C. Packaging Double-Helical DNA into Viral Capsids: Structures, Forces, and Energetics. *Biophysical Journal*, 95(2):497–502, 2008.

Pineirua, M., Bico, J., and Roman, B. Capillary origami controlled by an electric field. *Soft Matter*, 6: 4491–4496, 2010.

Plaza, G. R., Guinea, G. V., Pérez-Rigueiro, J., and Elices, M. Thermo-hygro-mechanical behavior of spider dragline silk: Glassy and rubbery states. *Journal of Polymer Science Part B: Polymer Physics*, 44(6):994–999, 2006.

Pocivavsek, L., Dellsy, R., Kern, A., Johnson, S., Lin, B., Lee, K. Y. C., and Cerda, E. Stress and fold localization in thin elastic membranes. *Science*, 320(5878):912–916, 2008.

Pomeau, Y. and Villermaux, E. Two hundred years of capillarity research. *Physics Today*, 59(3):39, 2006.

Porter, D., Guan, J., and Vollrath, F. Spider silk: Super material or thin fibre? *Advanced Materials*, 25 (9):1275–1279, 2012.

Pugno, N. M. The "Egg of Columbus" for Making the World's Toughest Fibres. *PLoS ONE*, 9(4): e93079, 2014.

Purohit, P. K., Kondev, J., and Phillips, R. Mechanics of DNA packaging in viruses. *Proceedings of the National Academy of Sciences of the United States of America*, 100(6):3173–3178, 2003.

Py, C., Reverdy, P., Doppler, L., Bico, J., Roman, B., and Baroud, C. N. Capillary origami: Spontaneous wrapping of a droplet with an elastic sheet. *Phys. Rev. Lett.*, 98(15):156103, 2007.

Quéré, D. and Di Meglio, J.-M. The meniscus on a fibre. *Advances in Colloid and Interface Science*, 48 (0):141 – 150, 1994.

Rogers, J. A., Someya, T., and Huang, Y. Materials and mechanics for stretchable electronics. *Science*, 327(5973):1603–1607, 2010.

Roman, B. and Bico, J. Elasto-capillarity: deforming an elastic structure with a liquid droplet. *Journal of Physics: Condensed Matter*, 22(49):493101, 2010.

Roman, B., Gay, C., and Clanet, C. Pendulum, drops and rods: a physical analogy. *Am. J. Phys.*, 2001.

Schneider, P. Elastic properties of the viscid silk of orb weaving spiders (Araneidae). *Naturwissenschaften*, 82(3):144–145, 1995.

Scott, R. *In the Wake of Tacoma: Suspension Bridges and the Quest for Aerodynamic Stability*. ASCE Press, 2001.

Sensenig, A. T., Lorentz, K. A., Kelly, S. P., and Blackledge, T. A. Spider orb webs rely on radial threads to absorb prey kinetic energy. *Journal of The Royal Society Interface*, 9(73):1880–1891, 2012.

Shenoy, V. B., Reddy, C. D., and Zhang, Y.-W. Spontaneous curling of graphene sheets with reconstructed edges. *ACS Nano*, 4(8):4840–4844, 2010.

Shim, J., Perdigou, C., Chen, E. R., Bertoldi, K., and Reis, P. M. Buckling-induced encapsulation of structured elastic shells under pressure. *Proceedings of the National Academy of Sciences of the United States of America*, 109(16):5978–5983, 2012.

Simmons, A. H., Michal, C. A., and Jelinski, L. W. Molecular orientation and two-component nature of the crystalline fraction of spider dragline silk. *Science*, 271(5245):84–87, 1996.

Skotheim, J. M. and Mahadevan, L. Physical limits and design principles for plant and fungal movements. *Science*, 308(5726):1308–1310, 2005.

Spatz, H.-C., Bruchert, F., and Pfisterer, J. Multiple resonance damping or how do trees escape dangerously large oscillations? *Am. J. Bot.*, 94(10):1603–1611, 2007.

Stefan, M. Experiments on apparent adhesion. 1874.

Stoop, N., Wittel, F. K., and Herrmann, H. J. Morphological phases of crumpled wire. *Phys. Rev. Lett.*, 101:094101, 2008.

Stoop, N., Najafi, J., Wittel, F. K., Habibi, M., and Herrmann, H. J. Packing of elastic wires in spherical cavities. *Phys. Rev. Lett.*, 106:214102, 2011.

Suter, R. B. and Stratton, G. E. Spitting performance parameters and their biomechanical implications in the spitting spider, Scytodes Thoracica. *J Insect Sci*, 9:1–15, 2009.

Sutherland, T. D., Young, J. H., Weisman, S., Hayashi, C. Y., and Merritt, D. J. Insect silk: one name, many materials. *Annual review of Entomology*, 55:171–188, 2010.

Syms, R., Yeatman, E., Bright, V., and Whitesides, G. Surface tension-powered self-assembly of microstructures - the state-of-the-art. *Journal Of Microelectromechanical Systems*, 12(4):387 – 417, 2003.

Takahashi, K. M. Meniscus shapes on small diameter fibers. *Journal of Colloid and Interface Science*, 134(1):181 – 187, 1990.

Taylor, G. Electrically driven jets. *Proceedings of the Royal Society of London. Series A, Mathematical and Physical Sciences*, 313(1515):453–475, 1969.

Thompson, J. M. T. Advances in shell buckling: Theory and experiments. Technical report, -, 2014.

Timoshenko, S. *A history of the strength of materials*. Dover Publications, 1983.

Treacy, M., Ebbesen, T., and Gibson, J. Exceptionally high young's modulus observed for individual carbon nanotubes. 1996.

Van Beek, J., Hess, S., Vollrath, F., and Meier, B. The molecular structure of spider dragline silk: folding and orientation of the protein backbone. *Proceedings of the National Academy of Sciences of the United States of America*, 99(16):10266–10271, 2002.

Van Krevelen, D. W. and Te Nijenhuis, K. *Properties of polymers: their correlation with chemical structure; their numerical estimation and prediction from additive group contributions*. Elsevier, 2009.

Vargo, T. G., Hook, D. J., Gardella, J. A., Eberhardt, M. A., Meyer, A. E., and Baier, R. E. A multitechnique surface analytical study of a segmented block copolymer poly (ether-urethane) modified through an H_2O radio frequency glow discharge. *Journal of Polymer Science Part A: Polymer Chemistry*, 29 (4):535–545, 1991.

Vella, D. and Mahadevan, L. The "cheerios effect". *American Journal of Physics*, 73(9):817–825, 2005.

Vepari, C. and Kaplan, D. L. Silk as a biomaterial. *Progress in Polymer Science*, 32(8–9):991 – 1007, 2007.

Verma, M. K. and Yadav, R. K. Supercriticality to subcriticality in dynamo transitions. *Physics of Plasmas*, 20(7):072307, 2013.

Vetter, R., Wittel, F., Stoop, N., and Herrmann, H. Finite elements simulation of dense wire packings. *European Journal of Mechanics - A/Solids*, 37:160–171, 2013.

Vetter, R., Wittel, F. K., and Herrmann, H. J. Packing of elastic wires in flexible shells. *arXiv*, 2015.

Vincent, O., Weißkopf, C., Poppinga, S., Masselter, T., Speck, T., Joyeux, M., Quilliet, C., and Marmottant, P. Ultra-fast underwater suction traps. *Proceedings of the Royal Society B: Biological Sciences*, 278(1720):2909–2914, 2011.

Vollrath, F. and Mohren, W. Spiral geometry in the garden spider's orb web. *Naturwissenschaften*, 72 (12):666–667, 1985.

Vollrath, F. Analysis and interpretation of orb spider exploration and web-building behavior. *Advances in the Study of Behavior*, 21(1):147–199, 1992.

Vollrath, F. Spider webs and silks. *Scientific American*, 266(3):70–76, 1992.

Vollrath, F. Spider silk: Thousands of nano-filaments and dollops of sticky glue. *Current Biology*, 16 (21):R925 – R927, 2006.

Vollrath, F. and Edmonds, D. Consequences of electrical conductivity in an orb spider's capture web. *Naturwissenschaften*, 100(12):1163–1169, 2013.

Vollrath, F. and Edmonds, D. T. Modulation of the mechanical properties of spider silk by coating with water. *Nature*, 340(6231):305–307, 1989.

Vollrath, F. and Knight, D. P. Liquid crystalline spinning of spider silk. *Nature*, 410(6828):541–548, 2001.

Vollrath, F. and Parker, G. A. Giant female or dwarf male spiders? *Nature*, 385(6618):688–688, 1997.

Vollrath, F., Fairbrother, W. J., Williams, R. J. P., Tillinghast, E. K., Bernstein, D. T., Gallagher, K. S., and Townley, M. A. Compounds in the droplets of the orb spider's viscid spiral. *Nature*, 345(6275): 526–528, 1990.

Wright, S. *The antimicrobial properties of spider silk*. PhD thesis, University of Nottingham, 2011.

Zarzycki, J. *Glasses and the vitreous state*. Number 9. Cambridge University Press, 1991.

Zheng, Y., Bai, H., Huang, Z., Tian, X., Nie, F.-Q., Zhao, Y., Zhai, J., and Jiang, L. Directional water collection on wetted spider silk. *Nature*, 463(7281):640–643, 2010.